Matrix - Mineral Interfaces in Biomineralization: Designing an in vitro Assay for Nacre Formation

by Ellen Keene

MATRIX – MINERAL INTERFACES IN BIOMINERALIZATION: DESIGNING AN *IN VITRO* ASSAY FOR NACRE FORMATION

A Dissertation

Presented to the Faculty of the Graduate School

of Cornell University

In Partial Fulfillment of the Requirements for the Degree of

Doctor of Philosophy

by

Ellen Keene

August 2010

MATRIX – MINERAL INTERFACES IN BIOMINERALIZATION: DESIGNING AN *IN VITRO* ASSAY FOR NACRE FORMATION

Ellen Keene, Ph. D.

Cornell University 2010

The formation of biogenic crystals *in vivo* (biomineralization) is controlled in part by the interface between organic and inorganic components. These interfaces can control the nucleation and growth of crystals, leading to the desired crystal polymorph, morphology, size, and orientation. By studying these interfaces, and developing increasingly complex synthetic systems, scientists can better understand biological systems and develop new materials with novel materials properties.

Mollusk nacre (mother-of-pearl) is a composite material composed of aragonite ($CaCO_3$) and various biopolymers. Synthetically, aragonite is difficult to nucleate. Mollusks utilize an organic matrix (β-chitin, silk fibroin-like hydrogel, and proteins) to control shell formation. Here, I present an *in vitro* assay for calcium carbonate mineralization where the assay complexity is systematically increased to understand the role of each matrix component in controlling crystallization. First, functionalized organic surfaces with soluble peptides were combined to probe the role of surface-peptide interactions in polymorph selectivity. Specifically, n16N (a 30 amino acid peptide from the Japanese pearl oyster *Pinctada fucata*) and its sequence variants, n16Ns (randomly scrambled) and n16NN (global Asp → Asn, Glu → Gln substitution), were combined with different forms of chitin (α and β) as well as synthetic Self-Assembled Monolayers (SAMs). Only the combination of n16N adsorbed onto β-chitin leads to the formation of aragonite *in vitro.* The n16N peptide and its variants have different binding affinities for β-chitin which correlate to their

ability to nucleate aragonite.

The complexity of the original *in vitro* assay was further increased to probe the role of another matrix component: silk fibroin hydrogels. With the addition of silk to synthetic, functionalized surfaces (SAMs), the ability of the SAM to affect crystal orientation and nucleation (as compared to controls) changed due to protein adsorption and denaturation on the functionalized surfaces. With the addition of silk fibroin to the chitin-n16N system, orientation and morphological control is gained (regardless of the n16N sequence). Flat vaterite crystals and amorphous calcium carbonate deposits are oriented with the β-chitin fibers. The work in this thesis provides evidence for the possible roles of the chitin-protein interface on mineralization in nacre.

BIOGRAPHICAL SKETCH

Ellen Christine Keene was born in 1982 to Richard and Elaine Keene in Fayetteville, North Carolina. As an army brat she traveled and moved around a lot, including living in a foreign country (Turkey). During her world travels as a child, she was fond of collecting rocks and seashells from various places that her parents would later have to pack up and move with each reassignment.

Upon her father's retirement from the military, she settled in the small town of Honeoye in New York's Finger Lakes region. She attended high school in Honeoye and graduated in 2001. She then attended Smith College in Northampton, Massachusetts where she majored in Physics. It is here that she became involved in scientific research. Working on several research projects (at Smith and in two REU programs), she discovered how much she enjoyed working in a lab. Her senior year at Smith, she completed a senior honors thesis under her adviser Professor Nalini Easwar studying dynamic force chains in flowing granular material. She graduated in the spring of 2005 with High Honors in Physics.

In the fall of 2005, Ellen started graduate school at Cornell University in the Materials Science and Engineering department working under Professor Lara Estroff. Here, she worked in the field of bio-inspired materials synthesis studying similar rocks and seashells that she collected as a child. After her defense in May 2010, Ellen will move to Michigan to begin work with The Dow Chemical Company. She will be doing research and development in their Analytical Sciences department.

ACKNOWLEDGMENTS

My success as a graduate student would not have been possible without the support of many. I am truly blessed, and for this I am forever grateful.

First, I would like to thank my adviser Professor Lara Estroff. Lara has an enthusiasm for research that is truly contagious, and she gave me encouragement and freedom to follow my interests in my research project. Also, as one of her first students I learned a lot about starting up and running a new lab. I am sure this experience will prove valuable as I start my career.

I am grateful for my labmates. We have been through a lot together and I will take away many fond memories. More specifically, Jason Dorvee, Miki Kunitake, and Hanying Li for many stimulating scientific conversations and helping to generate ideas for my research project. Amy Richter for collaborating on the GAFTIR work and writing a paper together. And Debra Lin, Ruiqi Song, and Dat Tran for our overlapped time together. And my undergrads, Vijay Ravichandran and Nikki Schwartzman, who both contributed to my work, but also helped me be a better student by learning how to teach them.

Many thanks to the facility managers at CCMR and NBTC who have spent countless hours teaching me about materials characterization. Especially, John Hunt and Dr. Maura Weathers at CCMR and Dr. Magnus Bergkvist previously of NBTC. They have taught me a lot, and these skills have proved invaluable for my dissertation and for my future career.

My research has also benefitted greatly from working in collaboration with Professor John Evans at New York University, who never said no to my requests for more peptide. Also, many thanks to Dr. Fabio Nudelman for many useful suggestions about proteins and biomineralization in general. And thanks to my committee members Professor Kit Umbach and Professor Lois Pollack.

And lastly, I would like to thank my family and friends. My friends have made life inside and outside of Cornell enjoyable and memorable. My parents have supported me throughout my 24 years as a student. And my husband and best friend, Mark, who has been a calming influence and a shoulder to lean on throughout graduate school.

TABLE OF CONTENTS

LIST OF FIGURES

LIST OF TABLES

LIST OF EQUATIONS

LIST OF ABBREVIATIONS

AA	Amino Acids
ACC	Amorphous Calcium Carbonate
AP24N	N-terminal peptide from *Haliotis refecens* protein AP24
Asn	Asparagine
Asp/p-Asp	Aspartic Acid/poly-L-Aspartic Acid
BSA	Bovine Serum Albumin
$CaCO_3$	Calcium Carbonate
CD	Circular Dichroism
$-CH_3$	methyl terminated SAM
-COOH	carboxylate terminated SAM
Cys	Cysteine
DI water	deionized water
DR80	Direct Red 80
EDX	Energy Dispersive X-ray
FTIR	Fourier transform infrared
G'	Storage modulus
G''	Loss modulus
GADDS	General Area Detector Diffraction System
GAFTIR	Grazing angle Fourier transform infrared
Gln	Glutamine
Glu/p-Glu	Glutamic Acid/poly-L-Glutamic Acid
IDPs	Intrinsically Disordered Proteins/Peptides
Method 1	Silk solutions purified with DI water
Method 2	Silk solutions purified with 5 w/v% Marseilles soap
Method 3	Silk solutions purified with 0.02 M sodium carbonate

MS-gel	Marseilles soap purified silk fibroin hydrogel
n16	16 kDa protein from the nacreous layer of *Pinctada fucata*
n16N	30 AA N-terminal domain of n16
n16NN	same as n16N with Asp → Asn and Glu → Gln
n16Ns	scrambled n16N sequence
pI	isoelectric point
SAM	Self Assembled Monolayer
SC-gel	Sodium carbonate purified silk fibroin hydrogel
SEM	Scanning Electron Microscopy
TGA	Thermogravimetric Analysis
Tyr	Tyrosine
W-gel	water purified silk fibroin hydrogel
WS	water soluble
XRD	x-ray diffraction

CHAPTER 1

INTRODUCTION:

CALCIUM CARBONATE MINERALIZATION IN NACRE: *IN VIVO* AND *IN VITRO* MODELS

1.1 Introduction

Biomineralization is the study of biological processes that result in the synthesis of composites of inorganic minerals within organic matrices as part of their skeletal systems. Organisms from all 5 kingdoms are known to produce many different minerals with a wide variety of functions.[1] A few common examples include mollusk shells (calcium carbonate), bone and teeth (calcium phosphate), diatoms and sponge spicules (silica), and magnetotatic bacteria (iron oxide). By studying these systems as materials scientists, we can learn strategies from biology to create new composite materials as well as design *in vitro* systems to answer questions from biology. The scope of my research was to study the mollusk shell and develop an *in vitro* organic matrix for the crystallization of calcium carbonate to further understand how the mollusk exerts control over polymorph selectivity.

1.2 Crystallochemical Aspects of Calcium Carbonate Mineralization

In classical crystallization theory, nucleation occurs via an accumulation of ions or small molecules to form clusters (i.e., nuclei). A crystal will not grow until nuclei reach a critical size (a balance between increasing the surface energy related to the growing surface area and the reduction of bulk energy related to the formation of a crystal lattice). Once the critical size is reached, continued growth leads to a reduction

in Gibbs free energy and the crystal will continue to grow unimpeded. Purely thermodynamic considerations often do not predict experimental results, because crystallization is often a kinetic process (Figure 1.1). Kinetic control can express itself in non-equilibrium crystal morphologies as well as in the formation of different polymorphs.

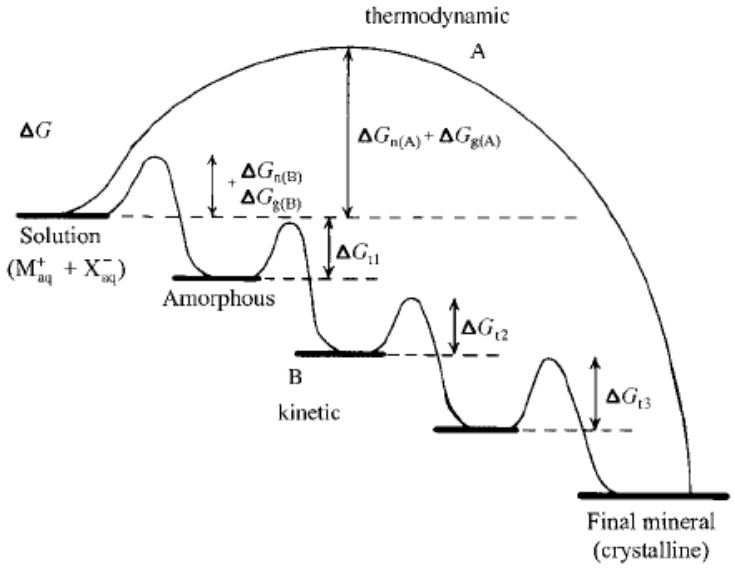

Figure 1.1 Crystallization pathways under thermodynamic and kinetic control. A system may follow a one step route (thermodynamic pathway A) or as a series of steps (kinetic pathway B). Each pathway depends on the Gibbs free energy (ΔG) associated with nucleation (n) and growth (g).[2]

Polymorphism is the existence of more than one crystal structure for a crystalline system. Polymorphism has great scientific and technological significance as polymorphs exhibit different materials properties such as hardness, optical properties, and solubility all of which are important to fields such as pharmaceuticals, agrochemistry, pigments and dyes, as well as the food industry. Therefore, the ability to predict and control crystal polymorphism is a continuing scientific challenge. In

biomineralization, polymorphism is utilized for different materials properties necessary for different locations within the organism. One such example is in mollusks, which can selectivity deposit different polymorphs of calcium carbonate (i.e., calcite and aragonite) under the control of biopolymers (Figure 1.2). Polymorph is determined during crystal nucleation. As such, it is necessary to study the microenvironment where the crystal forms to understand polymorph selectivity (see Chapters 2, 4 and 5).

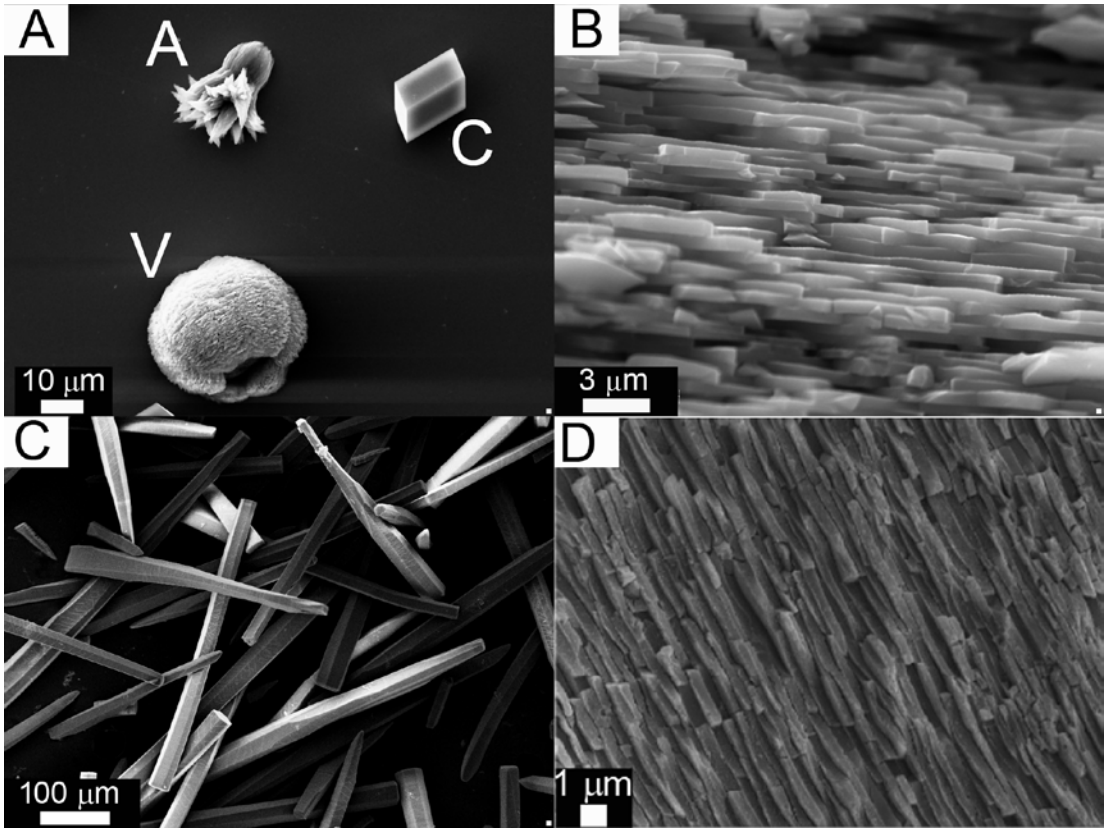

Figure 1.2 Synthetic and biogenic forms of calcium carbonate. (A) Synthetically grown $CaCO_3$. The labels on the micrograph indicate polymorph: *A* = aragonite, *C* = calcite, and *V* = vaterite. (B) Biogenic aragonite tablets from a pearl (C) Biogenic calcite prisms from *Atrina rigida* (D) Biogenic vaterite tablets in a lackluster pearl from *Hyriopsis cumingii* (modified from ref.[3]).

Calcium carbonate forms a variety of polymorphic forms. There are 3 anhydrous phases (calcite, aragonite, and vaterite), 2 hydrated crystalline forms (monohydrate and hexahydrate), and an amorphous phase. Within Nature, calcite and aragonite are the most commonly found polymorphs, having similar thermodynamic stabilities under standard conditions.

Calcite, the most thermodynamically stable polymorph, has trigonal symmetry (3bar 2/m). Calcite can be described by two different unit cells: the smallest being the acute rhombohedron containing two $CaCO_3$ units, or the hexagonal unit cell with six $CaCO_3$ units. The hexagonal unit cell is used for convenience to clearly demonstrate the alternating layers of Ca and CO_3 perpendicular to the *c*-axis (Figure 1.3A). Synthetically, calcite grows as large rhombohedra defined by six stable {10.4} faces (Figure 1.2A). Calcite is brittle, as the {10.4} planes have relatively low attachment energies (that holds parallel layers together) and are also cleavage planes. Aragonite has orthorhombic symmetry (2/m 2/m 2/m) and is described by an orthorhombic unit cell. Similar to calcite, aragonite has alternating layers of Ca and CO_3, except in aragonite the CO_3 layers are split into a double layer, separated by 0.96 Å, with different orientations between the two layers (Figure 1.3B). This double layer eliminates the cleavage planes found in calcite and allows for better ion packing (and as a consequence aragonite has a higher density than calcite). Aragonite grows synthetically as small needle-like crystals, due to a higher growth rate along the crystal *c*-axis, that generally do not grow into large crystals (Figure 1.2A). The last anhydrous crystalline phase is metastable vaterite. Vaterite has hexagonal symmetry (6/m 2/m 2/m) and is described by a hexagonal unit cell. Like calcite and aragonite, vaterite has alternating layers of Ca and CO_3, except now the CO_3 layers are parallel to the *c*-axis which is perpendicular to the CO_3 position in both calcite and aragonite (Figure 1.3C).

Synthetically, vaterite forms as poly-crystalline spherulites (Figure 1.2A). Vaterite is a metastable phase and as such is rare in Nature (Figure 1.2D).

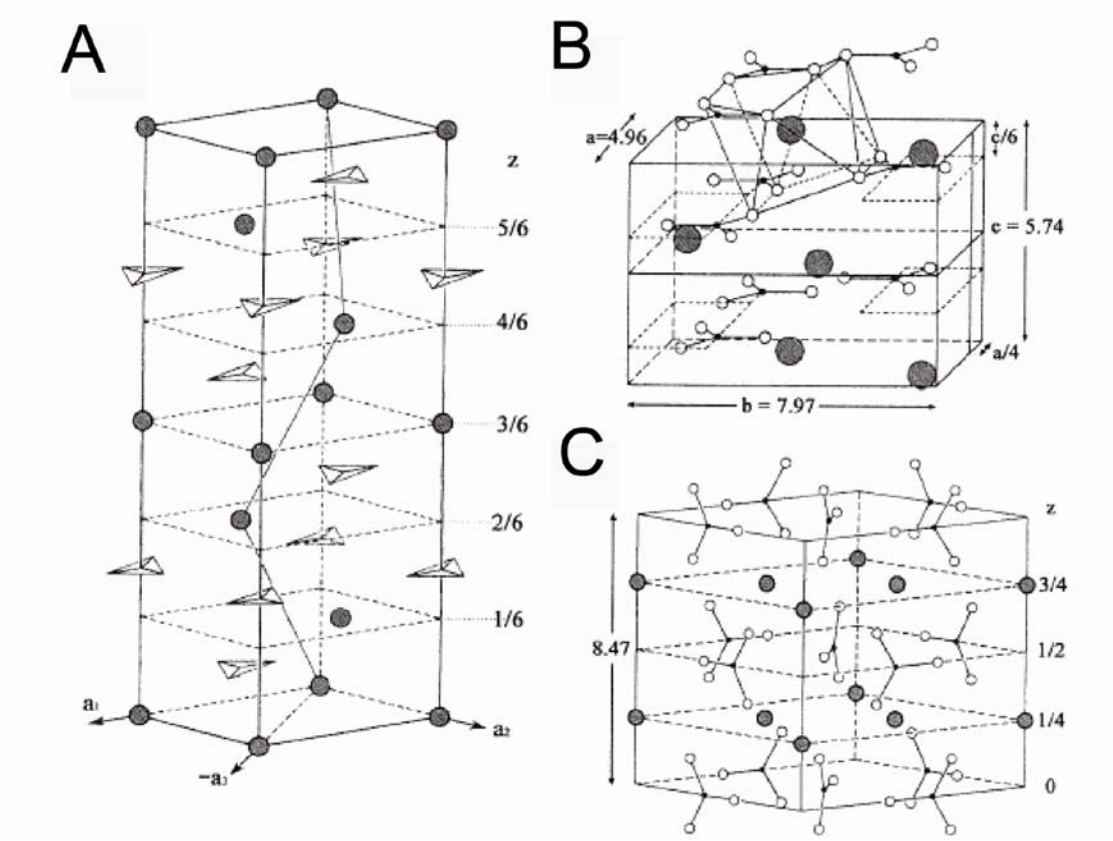

Figure 1.3 Crystal structures of (A) calcite, (B) aragonite, and (C) vaterite, with additional CO_3 groups shown outside unit cells for clarity and to demonstrate Ca coordination.[4, 5]

Traditional strategies for polymorph selection include changing solvents, temperature, reactant concentration, and other growth conditions in an attempt to control crystal formation by changing from a thermodynamic toward a kinetic regime (or vice versa).[6] While calcite and aragonite are widespread in biology, purposely

synthesized vaterite (under the control of the organism), exists in few organisms.[1, 7-9] The choice of polymorph, though, is almost always under strict control of specific biopolymer interactions. Specialized macromolecules (proteins, polysaccharides, etc.) are thought to control the physico-chemical processes of biomineral formation. For example, preferential adsorption of these macromolecules on distinct crystal faces can lead to growth of certain crystal faces (i.e., morphological control) as well as template a specific polymorph of the growing crystal. Vaterite is deposited abnormally (under the control of the environment) in lackluster pearls (Figure 1.2D), and has also been found in some mollusk shells trying to quickly repair their shell, and is suggested to be kinetically favorable under certain conditions and then transform into a more stable polymorph later.[10]

Within biology there is evidence that developing single crystals grow totally co-aligned with respect to an oriented domain of the organic matrix.[11] This growth process is termed heteroepitaxy. However, the occurrence of highly regular and oriented biogenic crystals does not automatically imply the validity of epitaxy. For example, recently it has been demonstrated that the formation of calcium carbonate crystals in biological systems may occur through the formation of amorphous calcium carbonate (ACC) which later converts to a more stable phase.[12-14] Furthermore, laboratory experiments have also demonstrated that calcite and aragonite can form via an amorphous precursor phase.[15-17] Regardless of the mineralization mechanism, biomineral synthesis is under strict control of the mineralizing organism.

1.3 Mollusk shell formation

The Mollusca phylum contains 7 taxonomic classes, 5 of which are shell bearing. The shells are typically layered structures composed of calcium carbonate, the

most commonly produced mineral by biological organisms.[1] Within the mollusk shell calcite, aragonite, and/or the amorphous phase have been identified. Within 3 of the mollusk classes, Gastropoda, Cepholopoda, and Bivalvia, there are several species that are capable of forming a bilayer structure. Typically, the bilayer structure contains both calcite and aragonite polymorphs separated into distinct layers of each called the prismatic and nacreous layers, respectively. Due to the mollusk's ability to abruptly switch from calcite to aragonite within its shell, the formation of mollusk shells is a model system for the general understanding of polymorphic control in biomineralization.

1.3.1 Mollusk shell physiology

Mollusk shell mineralization is classically described as a series of extracellular events occurring within compartments.[18] Over the years, the *in vivo* model for nacre formation has evolved due to continued research on the mollusk shell. Nacre contains an organic (proteins, polysaccharides, etc) and inorganic (mineral) component. Studies have focused primarily on how the organism utilizes these organic molecules to control mineralization, including polymorphism, crystal orientation, and morphology. Cells synthesize and release macromolecules (to the extracellular environment) which self-assemble into a three-dimensional matrix in which the mineral forms. The main steps in the mineralization process are: confining a space, forming an organic matrix framework, controlling ion input, constructing a nucleation site, controlling crystal orientation and growth, and terminating crystal growth.

The mantle, the organ responsible for shell formation, is a thin sheet of tissue that lies at the inner surface of the shell (Figure 1.4). The external surface of the shell is covered by a layer of highly cross-linked proteins called the periostracum (made by the mantle). The periostracum isolates the mantle from the surrounding environment

and creates an isolated compartment, called the extrapallial space, in which mineral is deposited. The organic biopolymers and inorganic ions (precursors to shell formation) are secreted by the epithelial cells of the mantle and make up the complex fluid filling the extrapallial space. It is well accepted that the organic matrix (both soluble and insoluble matrix components) are formed first, and this complex organic matrix induces heterogeneous nucleation of calcium carbonate crystals on its surface and regulates growth. The outer prismatic layer is deposited first, followed by the inner nacreous layer as the shell grows in thickness. Therefore, the mollusks that form bilayer shells are suitable models for investigating the polymorphic transition in the formation of the shell.

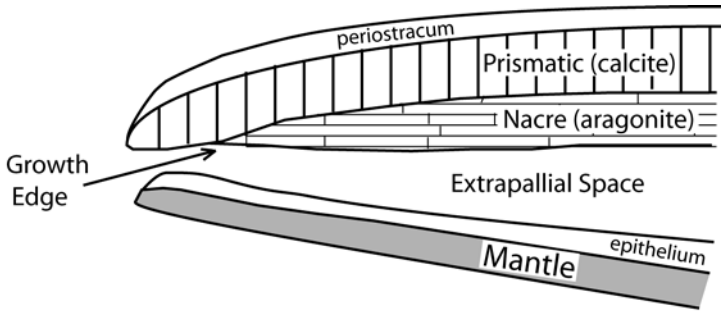

Figure 1.4 Schematic (not drawn to scale) of a mollusk shell cross section demonstrating the locations of the soft and hard tissues in relationship to the mineral growth edge. (Adapted from ref.[19])

There is much to be learned from mollusk shell formation and the role of the soluble and insoluble organic matrix in the formation and control of $CaCO_3$ mineralization. More specifically, Nature's control over crystal polymorph, size, and orientation, as well as, the thickness and configuration of the microstructural layers *in vivo*.

1.3.2 In vivo nacre models

Mollusca is a huge phylum with a wide variety of biomineral structures, but here I focus on mollusk nacre in mollusks that contain a bilayer structure containing a calcite prismatic layer and aragonite nacreous layer. Nacre, or mother of pearl, is only found in a few species across the entire Mollusca phylum, though it receives a lot of scientific attention due to its impressive mechanical properties, its bioactivity (i.e., as a material utilized for bone tissue engineering[20]), as well as for its polymorph selectivity (as it is difficult to synthesize aragonite under ambient conditions). X-ray photoelectron emission spectromicroscopy (X-PEEM) measurements on nacre indicate that the nacre tablets are co-aligned in the *c*-axis (with only ±11° misorientation over centimeter length scales), while there is no long-range order in the *ab* orientation.[21, 22] Although nacre has the same basic structure in different species of mollusks, there are a few differences when making comparisons across classes (i.e., gastropods, cephalopods, and bivalves). Bivalves follow a "brick wall" type structure, where there are overlapping terraces of nacre tablets (Figure 1.2B, 1.5A).[23] While in gastropods there is a "stack of coins" type structure where all the tablets are vertically aligned on top of each other (Figure 1.5B-D).[11, 24, 25] Some cephalopods (*Nautilus* is an example of this) have a mixture of both towered and terraced growth in adjacent locations. To focus my discussion of nacre, I will focus on what is known regarding nacre in bivalves only.

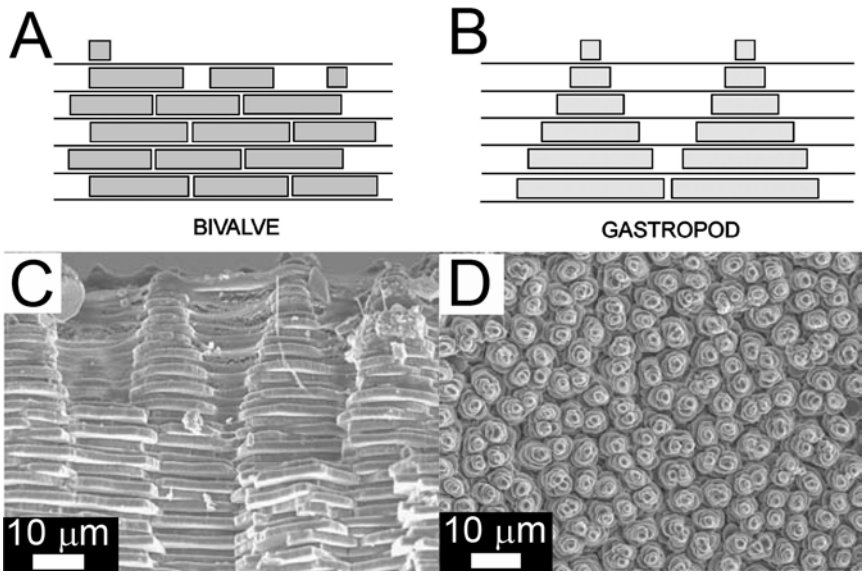

Figure 1.5 Simplified models of nacre formation of (A) "brick wall" bivalve nacre and (B) "stack of coins" gastropod nacre.[26] SEM micrographs of gastropod nacre from a (C) fractured transverse section of nacre from *Calliostoma zizyphynus* and (D) a top down view displaying towers of tablets from *Bolma rugosa*.[27]

The "modern" nacre models started in 1969 with the work of Bevelander and Nakahara who studied various mollusks through electron microscopy.[28] They proposed a "compartment model" where a preformed organic mold existed for aragonite tablets to form, but neglected to identify the organic components of the interlamellar matrix. As time progressed, individual researchers began to identify the organic components, such as an acidic template for nucleating crystal growth,[29] acidic macromolecules for inhibiting crystal growth,[30] and charged biomacromolecules such as specific amino acid sequences (i.e., Asp-rich)[31, 32] and sulfated polysaccharides[33] for concentrating calcium ions. These findings segregated the organic matrix into two groups, the soluble and the insoluble matrix fractions. The soluble component is made

up of “soluble” proteins (by water, acid, or EDTA), while the insoluble component is made up of the polysaccharide β-chitin and a hydrophobic silk fibroin-like protein (amino acid sequence is similar to spider and silkworm silk fibroin[34]).

All of these findings, as well as additional x-ray and electron diffraction data, were integrated into the next nacre model which was published in the 1980s by Weiner and coworkers.[32, 35, 36] This model was known as the “sandwich model” where the insoluble framework (composed of β-chitin) is sandwiched between two hydrophobic silk fibroin-like protein layers with a β-sheet structure, on top of which is a layer of Asp-rich soluble proteins (Figure 1.6A). The model suggested successive steps of nucleation and inhibition, with the addition of new organic matrix layers: poly-anionic template (chitin + proteins) to promote crystallization followed by the introduction of other proteins on top of the newly formed tablet to inhibit further crystal growth. This model was later referred to as “heteroepitaxy” because of indirect evidence that the organic matrix (β-chitin) acts as a template for aragonite nucleation and growth. Implications for epitaxial crystal nucleation was assumed because of the well-defined spatial relationship between the orientations of protein and chitin with aragonite.[36] A template mechanism requires stereochemical matching between the organic molecules and the mineral lattice, and is expected to determine crystal polymorph and orientation. However, this model does not explain the hierarchical structures of nacre tablets. A mineral bridge model was also proposed where the aragonite crystals grow through pores, or mineral bridges, to explain growth of co-aligned tablets.[11] Direct evidence for the mineral bridges model, however, was found in gastropods, but not in bivalves.[11, 37, 38]

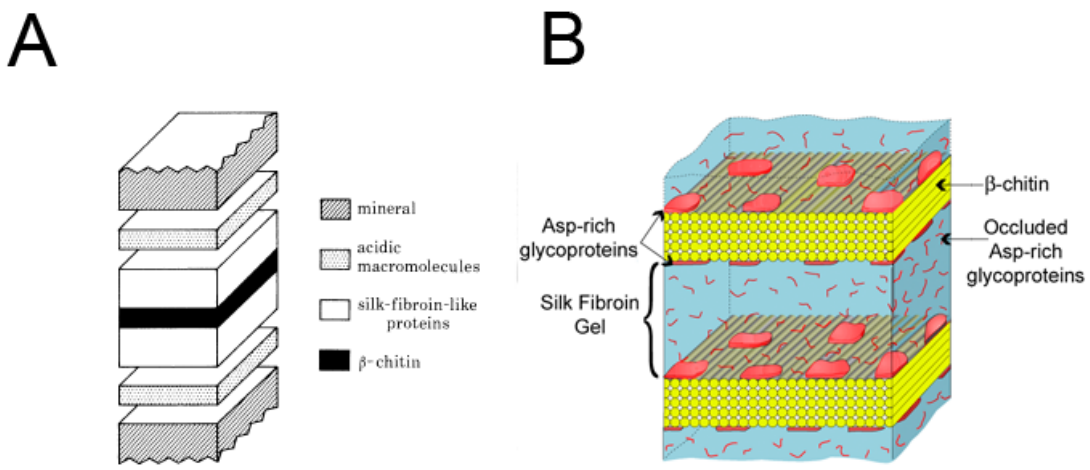

Figure 1.6 (A) The "sandwich" model where layers of chitin, silk, and acidic macromolecules separate aragonitic plates.[35] (B) The currently accepted model of the nacre growth within a silk gel-like phase.[39]

A drastic change in the view of *in vivo* nacre models came in 2001 with work by Levi-Kalisman et al., which remains the accepted model today (though it has been modified to fit a more dynamic perspective).[39, 40] This model (Figure 1.6B) retains the layered structure of the sandwich model, but changes the matrix structure based on cryo-TEM characterization of nacre. The insoluble β-chitin scaffold, which is the main component of the interlamellar matrix remains the same, but the silk fibroin-like proteins are proposed to be in a β-sheet gel-like state that acts as a space filler between chitin layers. Later environmental SEM studies of nacre verified that the silk-like protein is a hydrated gel.[40] The last matrix component, the assembly of soluble proteins, are both adsorbed onto the chitin surface as well as occluded within the silk-like gel. The proteins occluded within the silk-like hydrogel may control crystal polymorph and/or morphology. Nudelman et al. demonstrated, by histochemical studies of decalcified nacre, that there are carboxylate and sulfate groups on the organic matrix sheets acting as nucleation sites for nacre tablets.[41] These nucleation

sites (one per tablet) are randomly distributed and have no associated crystallographic orientation in the *ab* aragonite plane, though they may play a role in determining the crystal orientation in the *c* direction (i.e., templating mechanism). All the organic components are not thought to function in isolation, and their assembly and interaction may be essential for the correct regulation of crystal nucleation, growth, morphology, and polymorph.[42]

Although the soluble organic material is present in relatively low amounts (between 0.03 to 0.5 wt%),[43] great endeavors have been made to isolate these proteins from specific shell layers to sequence and characterize them. Some of these soluble proteins become occluded within the crystal while others may form films around the mineral.[44-47] A comprehensive review by Marin and coworkers discusses and groups a majority of the known molluscan proteins (from both the prismatic and nacreous layers) according to their pI values.[48] The majority of aragonitic proteins are termed "moderately acidic shell proteins" with pI's ranging between 4.5 and 7.5 and molecular weights below 85 kDa, and include n14,[49] n16,[50] nacrein,[51] pearlin,[52] MSI60,[34] mucoperlin,[53] Pif,[54] AP7,[55] and AP24,[55] to name a few examples. While many mollusk protein sequences are becoming known, we still lack a fundamental understanding of the participation of proteins in mollusk shell formation and no proteins that independently induce aragonite crystal formation, characteristic of nacre, have been identified.

Recently, it has been demonstrated that the formation of calcium carbonate crystals in biological systems may occur through the formation of ACC which later converts to a more stable phase.[12-14] Weiss et al. found that the larval shells of two marine bivalves contain an ACC precursor for aragonite.[13] Other researchers have begun to detect amorphous material in adult mollusks as well.[40, 56, 57] Amorphous materials are thought to be advantageous, because with the aid of organic

macromolecules, they can control the crystalline transition to a non-equilibrium crystal phase, as well as potentially be molded into intricate structures.[12, 58, 59] While the existence of ACC in nacre has become well accepted, its role, as well as the conversion mechanism to crystalline material (with the correct orientation and polymorph) is still debated.

1.4 Model systems

As discussed in the previous sections, mollusk biomineralization (and most other biomineralization systems) is regulated by soluble and insoluble organic components. The soluble components may control crystal phase and morphology, while the insoluble components may control nucleation and growth. The interplay between the organic and inorganic components *in vivo*, at both the molecular and the supramolecular levels, are dynamic, complicated, and not well understood. Therefore, scientists have tried to create model systems (such as for nacre) to better understand biomineralization systems, and to provide information about the mechanisms that may be relevant to biomineralization processes (section 1.4.1). Biomimetic experiments, or bio-inspired materials synthesis, try to exploit biological control *in vitro* to design new materials with novel materials properties (briefly discussed in section 1.4.2).

1.4.1 In vitro nacre models

Biological control over nacre mineralization is currently beyond what scientists have been able to achieve synthetically. By testing *in vitro* models we can better understand biological systems. Two *in vitro* studies have looked at the entire nacre organic matrix. Falini et al. and Belcher et al. have explored the organic matrix components of nacre *in vitro* to try and elucidate their roles in polymorph selectivity for nacre formation.[42, 60] Belcher et al. grew calcium carbonate on the nucleating

protein sheet isolated from the red abalone (*Haliotis rufescens*) and was able to switch between calcite and aragonite polymorphs in the presence of soluble proteins extracted from either the calcitic or aragonitic shell layers, respectively.[60] These results suggest that the soluble proteins control crystal polymorph and morphology. Falini et al. suggested that the insoluble organic matrix plays a role in polymorph control as well.[42] In Falini's assay, calcium carbonate was grown on a substrate of β-chitin and silk fibroin, with the addition of soluble macromolecules from either the calcitic or aragonitic layers. Falini's results demonstrated that polymorphic control was only possible with the complete substrate assembly (chitin + silk with soluble macromolecules). Both Belcher and Falini used a mixture of soluble macromolecules isolated from mollusk shells. As a result, nothing could be concluded about which protein(s) were important for determining polymorph selectivity.

Subsequent experiments have further investigated the function of the total organic matrix assembly extracted from the mollusk shell.[39, 54, 61, 62] These experiments have tried to distinguish between different protein functions in the assembly by isolating individual matrix components, and the results suggest that a subset of macromolecules are important for polymorph selectivity. More recently researchers have focused on extracting, purifying, and characterizing individual macromolecules, then using them in *in vitro* crystallization assays to try and gain information regarding the nucleating capabilities of the specific macromolecule isolated.[49, 54, 62-68] Information about these shell proteins' location (in the tissue and its spatial relationship to nacre) as well as structure (primary, secondary, and tertiary) are necessary to identify its function *in vivo*.

Shell proteins exert a control on the biomineralization process, and to start to understand these "control" proteins at the molecular level, shorter terminal peptide sequences have been made from the full known protein sequences.[55, 69-73] By utilizing

peptides, studies can try and understand the relationship between the structure of the peptide and its function in nacre formation (see Chapter 2). From these shorter sequences, important residue clusters can be identified. Many nacre proteins contain short, contiguous charged clusters of anionic (Asp, Glu), cationic (Lys, His, Arg), or hydrogen-bonding donor/acceptor (Ser, Thr, Tyr, Gln, Asn) residues.[74] With an appropriate balance of each residue type, each protein sequence is capable of binding Ca^{2+}, CO^{3-}, and water either in solution or at the mineral interface.[45, 70, 75] Other important residues include Gly, Pro, and Cys, which can affect protein conformation, motion, and stability.[74] To date, few nacre peptide structural studies have been conducted, though the ones that have been studied demonstrate that many nacre-associated polypeptides are structurally unstable and require external forces to stabilize their internal structures (i.e., intrinsically disordered).[70, 72, 76-78] One such study investigated the organic-mineral interface with x-ray adsorption near edge spectroscopy (XANES). This study found evidence of peptide ordering (of the amino acid side chains) when the nacre-specific peptide is associated with the mineral.[78]

The control macromolecules are typically minor macromolecular components of the biological material. Often, in *in vitro* crystallization studies, aragonitic proteins are insufficient to nucleate aragonite by itself. Rather the proteins need to be adsorbed to a substrate, mixed with other macromolecules, or combined with magnesium to achieve polymorph selectivity.[42, 49, 50, 60, 79] While nacre protein research looks at the individual macromolecules, these studies often neglect to take into account the other organic matrix components (i.e., the insoluble "framework" macromolecules: β-chitin and silk-like protein hydrogel, or that some of the control proteins may be part of a larger protein complex).

After cellulose, chitin (a linear polysaccharide whose monomer unit is N-acetylglucosamine, Figure 1.7) is the second most abundant biopolymer found in

Nature.[80] In nacre, the major component of the nacre interlamellar matrix is β-chitin (parallel repeat of the monomer unit).[39] Little *in vitro* research has been done on chitin,[79, 81-84] as its role in calcium carbonate based minerals appears relatively passive: neither chitin nor chitosan (deacetylated chitin) modify calcium carbonate growth *in vitro*.[79, 81, 82, 84] *In vivo*, β-chitin fibrils are preferentially aligned parallel to the *a*-axis of the aragonite tablets.[32] This polysaccharide-crystal alignment implies that aragonite orientation may be governed by the chitin, however, chitin lacks any chemical functional groups (i.e., carboxylates) capable of interacting strongly with calcium carbonate.[32, 36] However, a class of multi-domain proteins, often referred to as interactive matrix proteins,[85] are believed to interact with both the β-chitin substrate and the growing crystal.[34, 64, 65] It is likely that these proteins somehow translate the chitin fibril orientation to the crystals,[41] either directly or via "molecular proxies", i.e., other matrix proteins that interact directly with the interactive matrix proteins and the mineral phase as it grows. Over the years, multiple nacre-specific proteins, which may fulfill the role of "molecular proxies," have been identified and characterized.[48, 54, 74] In order to successfully model polymorph selection and phase stabilization in the laboratory, similar protein-polysaccharide interactions should be exploited to form a stable, functionalized surface for crystal nucleation (see Chapters 2, 4, and 5).

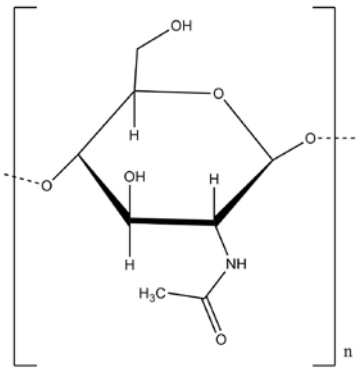

Figure 1.7 Chemical structure of chitin monomer (α-chitin = anti-parallel repeat, β-chitin = parallel repeat)

Another key component in the formation of mollusk shells is the hydrophobic Gly and Ala rich silk-like protein hydrogel (Figure 1.8). While the exact role of silk fibroin in nacre growth is unknown, possible roles have been speculated.[40] *In vivo* the silk-like hydrogel is a space filling agent and therefore can maintain the appropriate microenvironment for mineralization. *In vitro*, silk fibroin hydrogels are mild inhibitors of mineralization, and as such may limit the space for a critical nucleus to develop.[40] Therefore, the hydrogel can act as a site directing agent by suppressing crystallization, preventing uncontrolled crystallization until nutrients are in contact with the nucleating site or with the already formed mineral. Nature utilizes hydrogels *in vivo* because the crystallization environment in a hydrogel differs from solution growth in diffusion rates, ion activities, and water "structure" (especially in hydrophobic gels like silk) making a hydrogel an ideal environment to control crystal growth *in vivo*. Crystal growth in gels can also lead to morphological changes in the forming crystal, and sometimes result in porous crystals if the gel becomes occluded.[86-93]

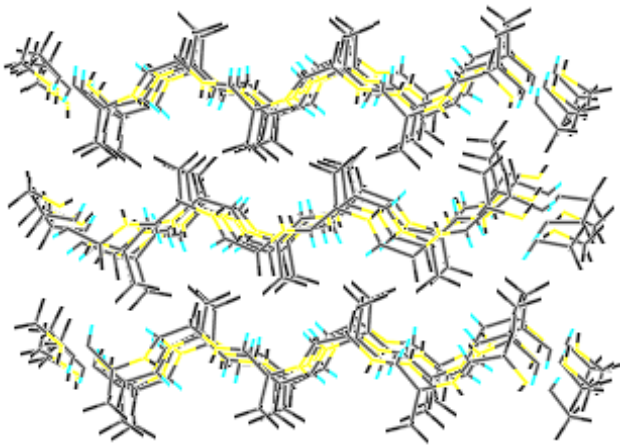

Figure 1.8 β-sheet structure of silk fibroin (rich in glycine and alanine)

In nacre, the silk-like proteins do not occur alone *in vivo,* but as a three-dimensional matrix (with chitin) for interaction with the soluble proteins, and together the matrix is able to control mineralization in a confined space. Therefore, both chitin and silk should be considered when designing an *in vitro* nacre model.[39, 42] Scanning electron microscopy (SEM) and cryo-TEM (transmission electron microscopy) studies of an artificial chitin-silk (from silkworm cocoons) substrate showed that the addition of silk does not alter the appearance of chitin, nor does it appear to form a recognizable separate layer, and therefore may be intercalated into the chitin matrix.[39, 61] However, these studies, and most *in vitro* crystallization studies with silk have utilized silk as a solution or a film,[42, 83, 94-96] and few studies have actually looked at silk fibroin hydrogels. Therefore, to create more accurate *in vitro* models for nacre formation, one must use silk fibroin hydrogels in their experiments (see Chapters 4 and 5).

In vitro mineralization experiments, with nacre specific components, are essential for clarifying the exact role of these biomolecules in the nacre biomineralization process. Previously, few *in vitro* studies have investigated multi-component systems, but instead looked at one or two components at a time.[45, 54, 76, 97, 98] This thesis systematically investigates more complex systems, which will help elucidate the roles and interactions among the different components in the biomineralization process, including biology's polymorphic control.

1.4.2 Bio-inspired Materials Synthesis

Studies that utilize ideas from biomineralization, but do not explore the specific matrix components, are considered bio-inspired materials syntheses and not *in vitro* models. While synthetic analogs do not help to gain understanding about the exact role of specific biomolecules *in vivo,* they do provide a synthetic platform for the

creation of new materials with materials properties similar to their biogenic counterparts.

Bio-inspired materials synthesis is a fast growing scientific field that has produced an almost unmanageable amount of literature. *In vitro* studies using natural and synthetic molecular systems have shown that matrix control of crystal morphology is possible.[1, 33, 42, 60, 99-103] Biologically inspired calcium carbonate synthesis has been carried out with a range of additives and on a range of organic substrates. Additives can change crystal morphologies by modifying surface energies via preferential adsorption on crystal surfaces. Fewer studies have been able to show control over polymorph.[42, 60, 104] Researchers have utilized the addition of many additives in solution (both synthetic and biological) including polymers,[102, 105-107] amino acids,[108-111] and other low molecular weight additives[112, 113] to favor the nucleation of the less stable polymorphs, vaterite and aragonite.

Highly ordered surfaces, such as Langmuir-Blodgett and self-assembled monolayers (SAMs), have been employed as synthetic models for crystallization.[89, 104, 114-124] These studies exploit the interfacial molecular recognition between the SAM terminal functionality and the forming crystal nuclei at the organic-inorganic interface. Many of these systems are able to orient calcite crystals, but fewer are able to control polymorph without the addition of other soluble additives. Vaterite formation seems to be the most common metastable phase on disordered, rough, and/or high charge density monolayers,[104, 125-127] though ACC,[99, 128] and aragonite[15, 129] may also form.

By combining a nucleating surface, with soluble additives, crystal orientation as well as morphology and polymorph can be better controlled. The synthetic matrix can act as an organic template by orienting crystals (functionalized surfaces) and by affecting morphology/growth rates (additives). When SAMs are combined with soluble additives, such as magnesium, it is also possible to control the morphology of

the crystals as a function of the nucleating surface.[130] Another synthetic system, which coupled an agarose hydrogel on top of a carboxylate-terminated SAM, was able to simultaneously control calcite shape and orientation.[89] Yet another system, exploits the cooperative templating affect between the organic components and aragonite by using either poly(acrylic acid) or poly(aspartate) additives with a poly(vinyl alcohol) or SAM functionalized substrate.[131-134] Together, the components are successfully able to control polymorph by forming poly-crystalline aragonite thin films.

Besides using biological systems as inspiration for synthetic mineralization, mineralization in synthetic systems can also provide insight into possible mechanisms in biomineralization processes. For example, the previously mentioned application of SAMs to orient $CaCO_3$ nucleation can act as a synthetic model for understanding the process of organic-matrix mediated nucleation in mollusk shells (see Chapter 4). Also, the use of various additives to affect both crystal morphology and polymorph *in vitro* is similar to the role of the soluble additives in the nacre organic matrix. Therefore, the mechanisms learned through additive controlled crystallization can be applied to the understanding of nacre formation *in vivo*. The use of synthetic systems to understand *in vivo* processes is an important realization, as it is generally easier to identify mechanisms for controlled synthetic systems than it is for *in vivo* experiments.

1.5 Summary and Outlook

Gaining understanding of the molecular interactions occurring at the interface between inorganic mineral and a macromolecular organic matrix is still a scientific challenge in biomineralization. Biogenic crystal formation, such as the aragonite tablets of nacre, serve as an example of the importance of such interfaces. While the components of the nacre organic matrix are well characterized, the exact function of

individual components in controlling crystal growth are still being explored. Continued research is needed to elucidate key biological questions such as: what makes a "good" organic matrix, what gives the proteins structure in the organic matrix, which amino acid motifs determine polymorph selectivity, and what happens at biological interfaces (i.e., organic-organic or organic-inorganic interfaces) and how are they important to mineralization? To be able to fully utilize nature's control over mineral formation *in vitro* (i.e., polymorph, orientation, morphology), continued efforts in fundamental biomineralization research is required.

1.6 Outline of the dissertation

In this dissertation, I developed an *in vitro* model of nacre biomineralization. To study the control of polymorph selectivity I systematically built up the complexity of an experimental assay to understand the structure and function of the *in vivo* organic matrix responsible for nacre formation. My synthetic organic matrix is formed from biologically relevant components to probe biological control over mineralization *in vitro*. I utilized silk fibroin hydrogels to replace the silk-like proteins *in vivo*, and nucleating surfaces, such as the biologically relevant β-chitin, or SAMs with similar functionalities as the insoluble framework matrix. I also substituted short, nacre-specific peptides for the full, complex soluble protein matrix, to better understand their biological control on the molecular level.

The first part of this dissertation (Chapter 2) focuses on the function of surfaces and additives; specifically looking at the interaction between a nacre specific peptide, n16N,[72] with the insoluble organic matrix substrate, β-chitin.[79] Chapter 3 introduces silk fibroin hydrogels, the space filling protein within the organic matrix, and how purification method can affect the properties of the resulting gels. The last

part applies the silk hydrogel to the *in vitro* assay to look at the gel with respect to its structure at surfaces (Chapter 4) and in the entire synthetic matrix construct for calcium carbonate crystallization (Chapter 5).

REFERENCES

1. Lowenstam, H. A.; Weiner, S., *On Biomineralization*. Oxford University Press: New York, 1989.

2. Colfen, H.; Mann, S., *Angew. Chem.-Int. Edit.* **2003,** 42, (21), 2350-2365.

3. Qiao, L.; Feng, Q. L.; Li, Z., *Cryst. Growth Des.* **2007,** 7, (2), 275-279.

4. Meldrum, F. C., *International Materials Reviews* **2003,** 48, (3), 187-224.

5. Lippmann, F., *Sedimentary carbonate minerals*. Springer-Verlag: Berlin, 1973.

6. Bernstein, J., *Polymorphism in Molecular Crystals*. Oxford University Press: New York, 2002.

7. Lowenstam, H. A.; Abbott, D. P., *Science* **1975,** 188, (4186), 363-365.

8. Hasse, B.; Ehrenberg, H.; Marxen, J. C.; Becker, W.; Epple, M., *Chem. Eur. J.* **2000,** 6, (20), 3679-3685.

9. Gauldie, R. W., *J. Morphol.* **1993,** 218, (1), 1-28.

10. Lee, S. W.; Choi, C. S., *Cryst. Growth Des.* **2007,** 7, (8), 1463-1468.

11. Schaffer, T. E.; IonescuZanetti, C.; Proksch, R.; Fritz, M.; Walters, D. A.; Almqvist, N.; Zaremba, C. M.; Belcher, A. M.; Smith, B. L.; Stucky, G. D.; Morse, D. E.; Hansma, P. K., *Chem. Mater.* **1997,** 9, (8), 1731-1740.

12. Politi, Y.; Arad, T.; Klein, E.; Weiner, S.; Addadi, L., *Science* **2004,** 306, (5699), 1161-1164.

13. Weiss, I. M.; Tuross, N.; Addadi, L.; Weiner, S., *J. Exp. Zool.* **2002,** 293, (5), 478-491.

14. Raz, S.; Hamilton, P. C.; Wilt, F. H.; Weiner, S.; Addadi, L., *Adv. Funct. Mater.* **2003,** 13, (6), 480-486.

15. Amos, F. F.; Sharbaugh, D. M.; Talham, D. R.; Gower, L. B.; Fricke, M.; Volmer, D., *Langmuir* **2007,** 23, (4), 1988-1994.

16. Zhang, Z. P.; Gao, D. M.; Zhao, H.; Xie, C. G.; Guan, G. J.; Wang, D. P.; Yu, S. H., *J. Phys. Chem. B* **2006,** 110, (17), 8613-8618.

17. Wolf, S. E.; Leiterer, J.; Kappl, M.; Emmerling, F.; Tremel, W., *J. Am. Chem. Soc.* **2008,** 130, (37), 12342-12347.

18. Wilbur, K. M.; Saleuddin, A. S. M., Shell Formation. In *The Mollusca, Volume 4: Physiology*, Academic Press: New York, 1983; pp 235-287.

19. DiMasi, E.; Sarikaya, M., *J. Mater. Res.* **2004,** 19, (5), 1471-1476.

20. Shen, Y. T.; Zhu, J.; Zhang, H. B.; Zhao, F., *Biomaterials* **2006,** 27, (2), 281-287.

21. Gilbert, P.; Metzler, R. A.; Zhou, D.; Scholl, A.; Doran, A.; Young, A.; Kunz, M.; Tamura, N.; Coppersmith, S. N., *J. Am. Chem. Soc.* **2008,** 130, (51), 17519-17527.

22. Metzler, R. A.; Abrecht, M.; Olabisi, R. M.; Ariosa, D.; Johnson, C. J.; Frazer, B. H.; Coppersmith, S. N.; Gilbert, P., *Phys. Rev. Lett.* **2007,** 98, (26).

23. Gregoire, C., *Journal of Biophysical and Biochemical Cytology* **1957,** 3, (5), 797-808.

24. Wise, S. W., *Science* **1970,** 167, (3924), 1486-1488.

25. Feng, Q. L.; Li, H. B.; Cui, F. Z.; Li, H. D.; Kim, T. N., *J. Mater. Sci. Lett.* **1999,** 18, (19), 1547-1549.

26. Mann, S., *Biomineralization: Principles and Concepts in Bioinorganic Materials Chemistry*. Oxford University Press: Oxford, UK, 2001.

27. Cartwright, J. H. E.; Checa, A. G., *J. R. Soc. Interface* **2007,** 4, (14), 491-504.

28. Bevelander, G.; Nakahara, H., *Calcif. Tissue Res.* **1969,** 3, (1), 84-92.

29. Weiner, S.; Hood, L., *Science* **1975,** 190, (4218), 987-988.

30. Wheeler, A. P.; George, J. W.; Evans, C. A., *Science* **1981,** 212, (4501), 1397-1398.

31. Weiner, S., *Calcif. Tissue Int.* **1979,** 29, (2), 163-167.

32. Weiner, S.; Talmon, Y.; Traub, W., *Int. J. Biol. Macromol.* **1983,** 5, (6), 325-328.

33. Addadi, L.; Moradian, J.; Shay, E.; Maroudas, N. G.; Weiner, S., *Proc. Natl. Acad. Sci. U. S. A.* **1987,** 84, (9), 2732-2736.

34. Sudo, S.; Fujikawa, T.; Nagakura, T.; Ohkubo, T.; Sakaguchi, K.; Tanaka, M.; Nakashima, K.; Takahashi, T., *Nature* **1997,** 387, (6633), 563-564.

35. Weiner, S.; Traub, W., *Philosophical Transactions of the Royal Society of London Series B-Biological Sciences* **1984,** 304, (1121), 425-434.

36. Weiner, S.; Traub, W., *FEBS Lett.* **1980,** 111, (2), 311-316.

37. Rousseau, M.; Lopez, E.; Stempfle, P.; Brendle, M.; Franke, L.; Guette, A.; Naslain, R.; Bourrat, X., *Biomaterials* **2005,** 26, (31), 6254-6262.

38. Meyers, M. A.; Lim, C. T.; Li, A.; Nizam, B. R. H.; Tan, E. P. S.; Seki, Y.; McKittrick, J., *Mater. Sci. Eng. C-Mater. Biol. Appl.* **2009,** 29, (8), 2398-2410.

39. Levi-Kalisman, Y.; Falini, G.; Addadi, L.; Weiner, S., *J. Struct. Biol.* **2001,** 135, (1), 8-17.

40. Addadi, L.; Joester, D.; Nudelman, F.; Weiner, S., *Chem. Eur. J.* **2006,** 12, (4), 981-987.

41. Nudelman, F.; Gotliv, B. A.; Addadi, L.; Weiner, S., *J. Struct. Biol.* **2006,** 153, (2), 176-187.

42. Falini, G.; Albeck, S.; Weiner, S.; Addadi, L., *Science* **1996,** 271, (5245), 67-69.

43. Marin, F.; Luquet, G.; Marie, B.; Medakovic, D., Molluscan shell proteins: Primary structure, origin, and evolution. In *Current Topics in Developmental Biology, Vol 80*, 2008; Vol. 80, pp 209-276.

44. Marin, F.; Pokroy, B.; Luquet, G.; Layrolle, P.; De Groot, K., *Biomaterials* **2007,** 28, (14), 2368-2377.

45. Kim, I. W.; Collino, S.; Morse, D. E.; Evans, J. S., *Cryst. Growth Des.* **2006,** 6, (5), 1078-1082.

46. Blank, S.; Arnoldi, M.; Khoshnavaz, S.; Treccani, L.; Kuntz, M.; Mann, K.; Grathwohl, G.; Fritz, M., *J. Microsc.-Oxf.* **2003,** 212, 280-291.

47. Wustman, B. A.; Weaver, J. C.; Morse, D. E.; Evans, J. S., *Connective Tissue Research* **2003,** 44, 10-15.

48. Marin, F.; Luquet, G., *C. R. Palevol* **2004,** 3, (6-7), 469-492.

49. Kono, M.; Hayashi, N.; Samata, T., *Biochem. Biophys. Res. Commun.* **2000,** 269, (1), 213-218.

50. Samata, T.; Hayashi, N.; Kono, M.; Hasegawa, K.; Horita, C.; Akera, S., *FEBS Lett.* **1999,** 462, (1-2), 225-229.

51. Miyamoto, H.; Miyashita, T.; Okushima, M.; Nakano, S.; Morita, T.; Matsushiro, A., *Proc. Natl. Acad. Sci. U. S. A.* **1996,** 93, (18), 9657-9660.

52. Miyashita, T.; Takagi, R.; Okushima, M.; Nakano, S.; Miyamoto, H.; Nishikawa, E.; Matsushiro, A., *Mar. Biotechnol.* **2000,** 2, (5), 409-418.

53. Marin, F.; Corstjens, P.; de Gaulejac, B.; Vrind-De Jong, E. D.; Westbroek, P., *J. Biol. Chem.* **2000,** 275, (27), 20667-20675.

54. Suzuki, M.; Saruwatari, K.; Kogure, T.; Yamamoto, Y.; Nishimura, T.; Kato, T.; Nagasawa, H., *Science* **2009,** 325, (5946), 1388-1390.

55. Michenfelder, M.; Fu, G.; Lawrence, C.; Weaver, J. C.; Wustman, B. A.; Taranto, L.; Evans, J. S.; Morsel, D. E., *Biopolymers* **2003,** 70, (4), 522-533.

56. Nassif, N.; Pinna, N.; Gehrke, N.; Antonietti, M.; Jager, C.; Colfen, H., *Proc. Natl. Acad. Sci. U. S. A.* **2005,** 102, (36), 12653-12655.

57. Marxen, J. C.; Becker, W.; Finke, D.; Hasse, B.; Epple, M., *Journal of Molluscan Studies* **2003,** 69, 113-121.

58. Addadi, L.; Raz, S.; Weiner, S., *Adv. Mater.* **2003,** 15, (12), 959-970.

59. Aizenberg, J., *Adv. Mater.* **2004,** 16, (15), 1295-1302.

60. Belcher, A. M.; Wu, X. H.; Christensen, R. J.; Hansma, P. K.; Stucky, G. D.; Morse, D. E., *Nature* **1996,** 381, (6577), 56-58.

61. Levi, Y.; Albeck, S.; Brack, A.; Weiner, S.; Addadi, L., *Chem. Eur. J.* **1998,** 4, (3), 389-396.

62. Gotliv, B. A.; Addadi, L.; Weiner, S., *ChemBioChem* **2003,** 4, (6), 522-529.

63. Feng, Q. L.; Fang, Z.; Yan, Z. G.; Xing, R.; Xie, L. P.; Zhang, R. Q., *Acta Biochim. Biophys. Sin.* **2009,** 41, (11), 955-962.

64. Suzuki, M.; Murayama, E.; Inoue, H.; Ozaki, N.; Tohse, H.; Kogure, T.; Nagasawa, H., *Biochemistry Journal* **2004,** 382, 205-213.

65. Kong, Y.; Jing, G.; Yan, Z.; Li, C.; Gond, N.; Zhu, F.; Li, D.; AZHang, Y.; Zheng, G.; Wang, H.; Xie, L.; Zhang, R., *J. Biol. Chem.* **2009,** 284, (16), 10841-10854.

66. Matsushiro, A.; Miyashita, T.; Miyamoto, H.; Morimoto, K.; Tonomura, B.; Tanaka, A.; Sato, K., *Mar. Biotechnol.* **2003,** 5, (1), 37-44.

67. Lao, Y. X.; Zhang, X. Q.; Zhou, J.; Su, W. W.; Chen, R. J.; Wang, Y. G.; Zhou, W. H.; Xu, Z. F., *Comp. Biochem. Physiol. B: Biochem. Mol. Biol.* **2007,** 148, (2), 201-208.

68. Politi, Y.; Mahamid, J.; Goldberg, H.; Weiner, S.; Addadi, L., *CrystEngComm* **2007,** 9, 1171-1177.

69. Kim, I. W.; Darragh, M. R.; Orme, C.; Evans, J. S., *Cryst. Growth Des.* **2006,** 6, (1), 5-10.

70. Collino, S.; Evans, J. S., *Biomacromolecules* **2007,** 8, (5), 1686-1694.

71. Collino, S.; Kim, I. W.; Evans, J. S., *Cryst. Growth Des.* **2006,** 6, (4), 839-842.

72. Kim, I. W.; DiMasi, E.; Evans, J. S., *Cryst. Growth Des.* **2004,** 4, (6), 1113-1118.

73. Gebauer, D.; Verch, A.; Borner, H. G.; Colfen, H., *Cryst. Growth Des.* **2009,** 9, (5), 2398-2403.

74. Evans, J. S., *Chem. Rev.* **2008,** 108, (11), 4455-4462.

75. Weiner, S.; Addadi, L., *Trends Biochem. Sci.* **1991,** 16, (7), 252-256.

76. Amos, F. F.; Evans, J. S., *Biochem. J.* **2009,** 48, (6), 1332-1339.

77. Wustman, B. A.; Morse, D. E.; Evans, J. S., *Biopolymers* **2004,** 74, (5), 363-376.

78. Metzler, R. A.; Kim, I. W.; Delak, K.; Evans, J. S.; Zhou, D.; Beniash, E.; Wilt, F.; Abrecht, M.; Chiou, J. W.; Guo, J. H.; Coppersmith, S. N.; Gilbert, P., *Langmuir* **2008,** 24, (6), 2680-2687.

79. Keene, E. C.; Evans, J. S.; Estroff, L. A., *Cryst. Growth Des.* **2010,** 10, (3), 1383-1389.

80. Arias, J. L.; Fernandez, M. S., *Chem. Rev.* **2008,** 108, (11), 4475-4482.

81. Neira-Carrillo, A.; Yazdani-Pedram, M.; Retuert, J.; Diaz-Dosque, M.; Gallois, S.; Arias, J. L., *J. Colloid Interface Sci.* **2005,** 286, (1), 134-141.

82. Zhang, S. K.; Gonsalves, K. E., *Langmuir* **1998,** 14, (23), 6761-6766.

83. Falini, G.; Weiner, S.; Addadi, L., *Calcif. Tissue Int.* **2003,** 72, (5), 548-554.

84. Manoli, F.; Koutsopoulos, S.; Dalas, E., *J. Cryst. Growth* **1997,** 182, (1-2), 116-124.

85. Veis, A., Mineralization in organic matrix frameworks. In *Biomineralization*, Dove, P. M.; DeYoreo, J. J.; Weiner, S., Eds. Mineralogical Soc America: Washington, 2003; Vol. 54, pp 249-289.

86. Grassmann, O.; Neder, R. B.; Putnis, A.; Lobmann, P., *Am. Mineral.* **2003,** 88, 647-652.

87. Yang, D.; Qi, L. M.; Ma, J. M., *Chemical Communications* **2003**, (10), 1180-1181.

88. Estroff, L. A.; Addadi, L.; Weiner, S.; Hamilton, A. D., *Organic & Biomolecular Chemistry* **2004,** 2, (1), 137-141.

89. Li, H. Y.; Estroff, L. A., *J. Am. Chem. Soc.* **2007,** 129, (17), 5480-5483.

90. Li, H. Y.; Xin, H. L.; Muller, D. A.; Estroff, L. A., *Science* **2009,** 326, (5957), 1244-1247.

91. Li, H. Y.; Estroff, L. A., *Crystengcomm* **2007,** 9, (12), 1153-1155.

92. Grassmann, O.; Lobmann, P., *Chem. Eur. J.* **2003,** 9, (6), 1310-1316.

93. Zhan, J. H.; Lin, H. P.; Mou, C. Y., *Adv. Mater.* **2003,** 15, (7-8), 621-623.

94. Cheng, C.; Shao, Z. Z.; Vollrath, F., *Adv. Funct. Mater.* **2008,** 18, 2172-2179.

95. An, X. Q.; Cao, C. B., *J. Phys. Chem. C* **2008,** 112, (40), 15844-15849.

96. Jiang, F. G.; Yao, J. R.; Chen, X.; Shen, Z. Z., *Acta Chim. Sin.* **2009,** 67, (14), 1675-1679.

97. Feng, Q. L.; Pu, G.; Pei, Y.; Cui, F. Z.; Li, H. D.; Kim, T. N., *J. Cryst. Growth* **2000,** 216, (1-4), 459-465.

98. Kim, I. W.; Morse, D. E.; Evans, J. S., *Langmuir* **2004,** 20, (26), 11664-11673.

99. Aizenberg, J.; Muller, D. A.; Grazul, J. L.; Hamann, D. R., *Science* **2003,** 299, (5610), 1205-1208.

100. Greenfield, E. M.; Wilson, D. C.; Crenshaw, M. A., *American Zoologist* **1984,** 24, (4), 925-932.

101. Crenshaw, M. A., *Biological Bulletin* **1972,** 143, (3), 506-512.

102. Colfen, H.; Antonietti, M., *Langmuir* **1998,** 14, (3), 582-589.

103. Donners, J.; Nolte, R. J. M.; Sommerdijk, N., *J. Am. Chem. Soc.* **2002,** 124, (33), 9700-9701.

104. Mann, S.; Heywood, B. R.; Rajam, S.; Birchall, J. D., *Nature* **1988,** 334, (6184), 692-695.

105. Gower, L. A.; Tirrell, D. A., *J. Cryst. Growth* **1998,** 191, (1-2), 153-160.

106. Falini, G., *Int. J. Inorg. Mater.* **2000,** 2, (5), 455-461.

107. Gao, Y. X.; Yu, S. H.; Guo, X. H., *Langmuir* **2006,** 22, (14), 6125-6129.

108. Manoli, F.; Kanakis, J.; Malkaj, P.; Dalas, E., *J. Cryst. Growth* **2002,** 236, (1-3), 363-370.

109. Shivkumara, C.; Singh, P.; Gupta, A.; Hegde, M. S., *Mater. Res. Bull.* **2006,** 41, (8), 1455-1460.

110. Orme, C. A.; Noy, A.; Wierzbicki, A.; McBride, M. T.; Grantham, M.; Teng, H. H.; Dove, P. M.; DeYoreo, J. J., *Nature* **2001,** 411, (6839), 775-779.

111. Wolf, S. E.; Loges, N.; Mathiasch, B.; Panthofer, M.; Mey, I.; Janshoff, A.; Tremel, W., *Angew. Chem.-Int. Edit.* **2007,** 46, (29), 5618-5623.

112. Kitano, Y.; Hood, D. W., *Geochim. Cosmochim. Acta* **1965,** 29, (1), 29-41.

113. Davis, K. J.; Dove, P. M.; De Yoreo, J. J., *Science* **2000,** 290, (5494), 1134-1137.

114. Heywood, B. R.; Rajam, S.; Mann, S., *J. Chem. Soc.-Faraday Trans.* **1991,** 87, (5), 735-743.

115. Aizenberg, J.; Black, A. J.; Whitesides, G. H., *J. Am. Chem. Soc.* **1999,** 121, (18), 4500-4509.

116. Pokroy, B.; Aizenberg, J., *Crystengcomm* **2007,** 9, (12), 1219-1225.

117. Heywood, B. R.; Mann, S., *Adv. Mater.* **1994,** 6, (1), 9-20.

118. Rajam, S.; Heywood, B. R.; Walker, J. B. A.; Mann, S.; Davey, R. J.; Birchall, J. D., *J. Chem. Soc.-Faraday Trans.* **1991,** 87, (5), 727-734.

119. Heywood, B. R.; Mann, S., *Chem. Mater.* **1994,** 6, (3), 311-318.

120. Mann, S.; Heywood, B. R.; Rajam, S.; Walker, J. B. A., *Journal of Physics D-Applied Physics* **1991,** 24, (2), 154-164.

121. Walker, J. B. A.; Heywood, B. R.; Mann, S., *J. Mater. Chem.* **1991,** 1, (5), 889-890.

122. Berman, A.; Ahn, D. J.; Lio, A.; Salmeron, M.; Reichert, A.; Charych, D., *Science* **1995,** 269, (5223), 515-518.

123. Litvin, A. L.; Valiyaveettil, S.; Kaplan, D. L.; Mann, S., *Adv. Mater.* **1997,** 9, (2), 124-127.

124. Volkmer, D.; Fricke, M.; Vollhardt, D.; Siegel, S., *Journal of the Chemical Society-Dalton Transactions* **2002**, (24), 4547-4554.

125. Popescu, D. C.; Smulders, M. M. J.; Pichon, B. P.; Chebotareva, N.; Kwak, S. Y.; van Asselen, O. L. J.; Sijbesma, R. P.; DiMasi, E.; Sommerdijk, N., *J. Am. Chem. Soc.* **2007,** 129, (45), 14058-14067.

126. Fricke, M.; Volkmer, D.; Krill, C. E.; Kellermann, M.; Hirsch, A., *Cryst. Growth Des.* **2006,** 6, (5), 1120-1123.

127. Kuther, J.; Tremel, W., *Thin Solid Films* **1998,** 327, 554-558.

128. Lee, J. R. I.; Han, T. Y. J.; Willey, T. M.; Wang, D.; Meulenberg, R. W.; Nilsson, J.; Dove, P. M.; Terminello, L. J.; van Buuren, T.; De Yoreo, J. J., *J. Am. Chem. Soc.* **2007,** 129, (34), 10370-10381.

129. Kuther, J.; Nelles, G.; Seshadri, R.; Schaub, M.; Butt, H. J.; Tremel, W., *Chem. Eur. J.* **1998,** 4, (9), 1834-1842.

130. Han, Y. J.; Wysocki, L. M.; Thanawala, M. S.; Siegrist, T.; Aizenberg, J., *Angew. Chem.-Int. Edit.* **2005,** 44, (16), 2386-2390.

131. Hosoda, N.; Sugawara, A.; Kato, T., *Macromolecules* **2003,** 36, (17), 6449-6452.

132. Sakamoto, T.; Oichi, A.; Nishimura, T.; Sugawara, A.; Kato, T., *Polymer Journal* **2009,** 41, (7), 522-523.

133. Sugawara, A.; Oichi, A.; Suzuki, H.; Shigesato, Y.; Kogure, T.; Kato, T., *J. Polym. Sci. Pol. Chem.* **2006,** 44, (17), 5153-5160.

134. Hosoda, N.; Kato, T., *Chem. Mater.* **2001,** 13, 688-693.

CHAPTER 2

MATRIX INTERACTIONS IN BIOMINERALIZATION: ARAGONITE NUCLEATION BY AN INTRINSICALLY DISORDERED NACRE POLYPEPTIDE, N16N, ASSOCIATED WITH A β-CHITIN SUBSTRATE[*]

2.1 Abstract

Previous literature by Falini et al. suggests that the cooperation between β-chitin, proteins, and a silk fibroin-like hydrogel determines polymorph selectivity within the nacreous layer of mollusk shells (favoring aragonite over calcite formation). Here I present an *in vitro* assay in which I combine functionalized organic surfaces with soluble peptides to probe the role of surface-peptide interactions in calcium carbonate polymorph selectivity. Specifically, I combined n16N (a 30 amino acid peptide from the Japanese pearl oyster *Pinctada fucata*) and its sequence variants, n16Ns (randomly scrambled) and n16NN (global Asp → Asn, Glu → Gln substitution), with different forms of chitin (α and β). I found that the combination of n16N adsorbed onto β-chitin leads to the formation of aragonite *in vitro* as well as demonstrated chitin binding ability. Negative controls, including sequence modified versions of n16N (n16Ns and n16NN) exhibit variation in β-chitin binding and the ability to nucleate aragonite. The peptide + α-chitin combination exhibits very little chitin binding, and nucleates exclusively calcite with minor morphological effects. The n16N and n16Ns peptides used in this study are considered intrinsically disordered and have previously been shown to interact with calcium carbonate. I propose n16N's intrinsically disordered structure also allows the peptide to interact

[*] Portions reproduced with permission from E. C. Keene, J. S. Evans, and L. A. Estroff, *Crystal Growth and Design,* **2010**, 10 (3), 1383-1389. Copyright 2010 American Chemical Society.

with the substrate creating a new organic matrix interface. The cooperation between the peptide and substrate may explain the polymorph specificity among these samples.

2.2 Introduction

As described in Chapter 1, the invertebrate mollusk represents an important model materials system due to the presence of a bilayer shell in some bivalves that is comprised of two different polymorphs of calcium carbonate (the calcitic prismatic and the aragonitic nacre layers).[1] The materials properties of each shell layer are different and these properties arise in part from the presence of biomacromolecules in each layer.[2] A challenge to the materials science community is to establish how these biomacromolecules facilitate polymorph selection and materials properties. In order to develop molecular principles for the synthesis of new materials, based upon mollusk shells, we need to identify how proteins and polysaccharides assemble to form chemical environments that lead to polymorph selectivity. Here, I present a synthetic system with which to assay interactions among different matrix components and to evaluate which of these interactions lead to the selective nucleation of aragonite.

Extracting, purifying, and characterizing individual macromolecules is difficult, but can lead to information regarding the nucleating capabilities of specific macromolecules. Experiments have investigated the function of the total organic matrix assembly extracted from the mollusk shell.[1, 3, 4] These experiments have tried to distinguish between different protein functions in the assembly by isolating individual matrix components, and the results suggest that a subset of the macromolecules are important for polymorph selectivity.[5, 6]

Over the years, many nacre specific proteins have been identified and characterized, all of which are species specific.[7-11] Nacre specific proteins are often

hydrophilic and charged, while their specific functions are still being explored. One particular nacre specific protein, n16, from the dorsal region of the Japanese pearl oyster *Pinctada fucata,* is thought to be an aragonite promoter protein.[9] With the addition of n16, when grown in combination with magnesium and the water insoluble matrix from *P. fucata,* spherical or plate-like crystals form, and under certain conditions aragonite mineral deposits were observed.[9] The full protein is a 108 amino acid, acidic (pI 5.1), non-glycosolated protein rich in Gly, Tyr, Asn, and Cys.[9] A 30 amino acid N-terminal fragment of the n16 protein, n16N has been prepared to elucidate the effects of this protein on $CaCO_3$ nucleation and growth.[12-14] The peptide n16N is unfolded under "normal" conditions, but folds into a β-strand conformation under other conditions (i.e., concentration and solvent).[12, 13] Due to this property (unfolded in the monomeric state, but can undergo folding upon interaction with a "target") n16N is considered an intrinsically disordered peptide (IDP).[13, 15-19]

In previous *in vitro* mineralization studies with n16N, calcite crystals with "staircase" structures, in which both acute and obtuse edges of calcite were affected (a phenomenon not previously seen with other nacre proteins) promoting non-rhombohedral calcite geometries.[12, 14] NMR studies have found that n16N can form complexes with Ca^{2+} and its metal ion analogues (i.e., $CdCl_2$, $LaCl_3$, $EuCl_3$) indicating the presence of metal binding sites within the peptide sequence such as Asp and Glu residues.[13] Solid state ^{13}C-CP/MAS NMR experiments detected the presence of bound n16N peptide on geological calcite crystals "rescued" from overgrowth assays (the bound peptide could not be removed with successive washings).[13] Experiments with x-ray adsorption near edge spectromicroscopy (XANES) further explored the n16N-calcite association.[20] This experiment indicated that n16N undergoes significant peptide side chain rearrangement when adsorbed to the mineral, as compared to n16N in solution. From both the XANES and NMR experiments, it is as of yet unknown

whether n16N is localized exclusively at exposed organic-mineral interfaces, or if the n16N becomes occluded within the crystal during mineral formation. However, some recent n16N crystallization work, characterized with x-ray photoelectron emission spectromicroscopy (X-PEEM), found small amounts of lamellar aragonite (5%), where the layers are interspersed with organic material (n16N).[21]

Amino acid substitutions (global Asp → Asn and Glu → Gln substitution, n16NN) or sequence scrambling (n16Ns) of n16N were made to determine the participation of single residues in the mineralization process.[14, 22] The change in peptide sequence affects *in vitro* mineralization activities associated with each native polypeptide sequence. The scrambled sequence, n16Ns, still possessed the ability to affect calcite growth with the "staircase" structure, but to a smaller degree compared to the native n16N.[14] This type of mineralization activity, however, is absent from n16NN assays, but instead a "biofilm" coating forms over some rhombohedral calcite crystals.[22] It appears that n16NN may self-assemble to form thin films that become mineralized *in vitro.* The loss of mineralization activity is a result of the loss of Ca^{2+} binding sites (i.e., Asp and Glu) as NMR studies find that n16NN no longer forms metal-peptide complex as the native n16N.[22]

Here, I present an *in vitro* assay in which I combine functionalized organic surfaces with n16N (and its mutants) to probe the role of this particular peptide-surface interaction in calcium carbonate polymorph selectivity. Previous studies have shown that n16N interacts with calcium carbonate,[12, 14] but an interaction between peptide and chitin, to form a new matrix interface, has not previously been identified. My results demonstrate that the intrinsically disordered n16N sequence is responsive to multiple targets (i.e., mineral and polysaccharide) and preferentially nucleates aragonite once it is bound to β-chitin.

2.3 Results

2.3.1 Effect of nacre peptide sequence on polymorph selection.

My approach was to combine n16N and its sequence variants (Table 2.1), n16Ns (randomly scrambled) and n16NN (global Asp → Asn, Glu → Gln substitution),[22] with different forms of chitin (α and β) to establish the effects of different polysaccharide scaffolds and n16N on the formation of calcium carbonates. The chitin substrates were regenerated α-chitin (from reacetylated chitosan films),[23, 24] and β-chitin from purified squid pen[1, 23, 25] (see experimental for further details). The resultant polysaccharide + peptide combinations utilized in the experiments are summarized in Table 2.1. The n16N variants (n16Ns and n16NN) are peptide controls to determine the role of peptide sequence (n16Ns) and charge (n16NN) in the function of n16N. Crystallization and fluorescence microscopy experiments investigated different peptide-chitin assemblies and their role in determining polymorph selectivity.

The β-chitin + n16N combination yielded poly-crystalline aragonite, compared to negative control assays containing β-chitin alone, which resulted in rhombohedral calcite single crystals (Figures 2.1A, B and 2.2; Table 2.1). Aragonite crystals were identified by morphology (needle-like clusters) and verified by x-ray diffraction and Raman spectroscopy (Figure 2.2). Parallel assays were also run, using samples where n16N was initially adsorbed onto a β-chitin surface and subsequently rinsed to remove adventitiously bound peptide. Here, I observed the formation of aragonite and a minority vaterite component (Figure 2.3). This result indicates that residual n16N still remains bound to the β-chitin substrate after the washing procedures. Hence, I conclude that the n16N + β-chitin two-component system is capable of favoring the nucleation and growth of aragonite over calcite.

Table 2.1 Peptide-Substrate Interactions: Polymorph and Peptide Binding Results

Peptide	Substrate	Polymorph[1]	Peptide Binding[2]
n16N	β-chitin	Calcite 3% **Aragonite 89%** Vaterite 10%	Strong fluorescence
	α-chitin	**Calcite 97%** Aragonite 0% Vaterite 3%	No fluorescence
n16NN	β-chitin	Calcite 7% **Aragonite 71%** Vaterite 11%	Moderate fluorescence
	α-chitin	**Calcite 91%** Aragonite 2% Vaterite 7%	No Fluorescence
n16Ns	β-chitin	**Calcite 55%** Aragonite 34% Vaterite 11%	Weak Fluorescence
	α-chitin	**Calcite 93%** Aragonite 1% Vaterite 6%	No fluorescence

[1] The mineral phase percentages determined by counting more than 250 crystals from SEM images, over the triplicate experiments. Polymorph in bold highlights the majority mineral phase.

[2] Peptide binding was assessed by fluorescent labeling studies with a BODIPY maleimide dye. Fluorescence levels are described by pixel brightness levels: strong >200, moderate 100-200, and weak <100.

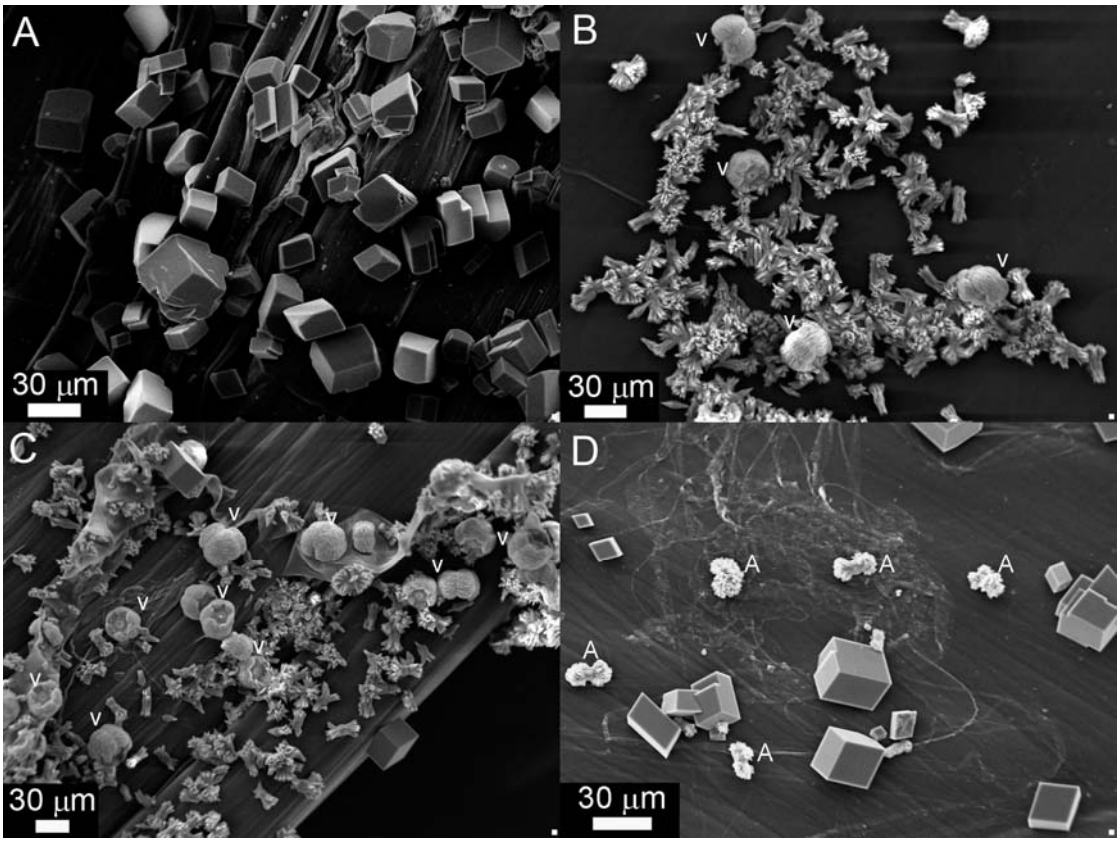

Figure 2.1 SEM micrographs of crystallization studies on β-chitin substrates with A) no additives (control), B) n16N, C) n16NN, and D) n16Ns. All crystals are calcite in (A). Vaterite crystals are designated by *V*'s in (B & C) while all other crystals are aragonite (majority phase) and aragonite crystals are designated by *A*'s in figure D while all other crystals are calcite. All peptide concentrations were 10 μM, and Ca^{2+} concentrations were 10 mM.

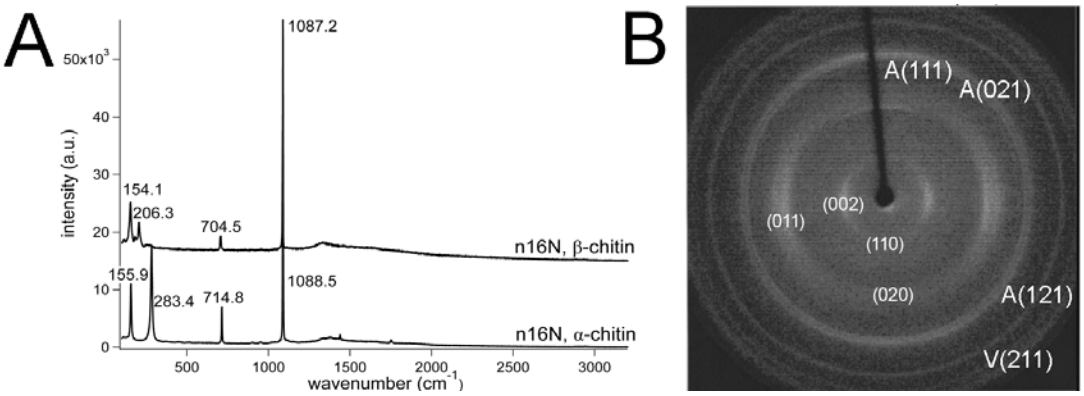

Figure 2.2 (A) Raman spectra of $CaCO_3$ crystals grown in the presence of n16N on α- and β-chitin substrates. These spectra correspond to calcite and aragonite, respectively. (B) XRD plot of $CaCO_3$ crystals grown on β-chitin in the presence of n16N. Smaller indices written on plot index the β-chitin structure. Indices preceded by an *A* index aragonite and a *V* index vaterite.

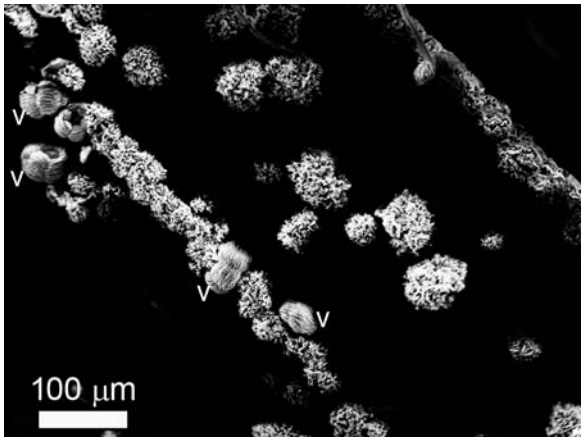

Figure 2.3 SEM micrograph of a piece of β-chitin that was incubated with 5 μM n16N, rinsed, then used for crystallization studies. Both aragonite and vaterite polymorphs are present, vaterite crystals are designed by white *V*'s; all other crystal aggregates are aragonite.

The β-chitin + n16NN crystallization assays produce similar results to those obtained with n16N (Table 2.1). Here, the majority of the crystals formed are aragonite, with a minority of vaterite and some calcite as well (Figure 2.1C). Crystallization studies conducted with n16Ns + β-chitin, however, exhibit a majority phase of calcite with the minority being aragonite (Figure 2.1D). Regions of high nucleation density contain exclusively calcite, while regions of lower nucleation density have a mixture of aragonite and calcite. This spatial variation in polymorph selectivity suggests that the n16Ns may still interact with the β-chitin surface, but not as effectively as native n16N. These control experiments (n16NN and n16Ns) show that the replacement of anionic residues with amide counterparts and the random scrambling of the n16N sequence led to a reduction in the ability of the two-component system to produce aragonite, although residual polymorph selectivity is still retained in spite of the amino acid sequence changes (Table 2.1).

Two other nacre-specific peptides, AP7N[26, 27] and AP24N,[26] along with a simple anionic polypeptide, poly-L-glutamic acid (p-Glu), were also tested in the β-chitin assay. For all three additives, only calcite forms (Figure 2.4). While there were interesting morphological effects with p-Glu, there was no polymorph selectivity (Figure 2.4A).

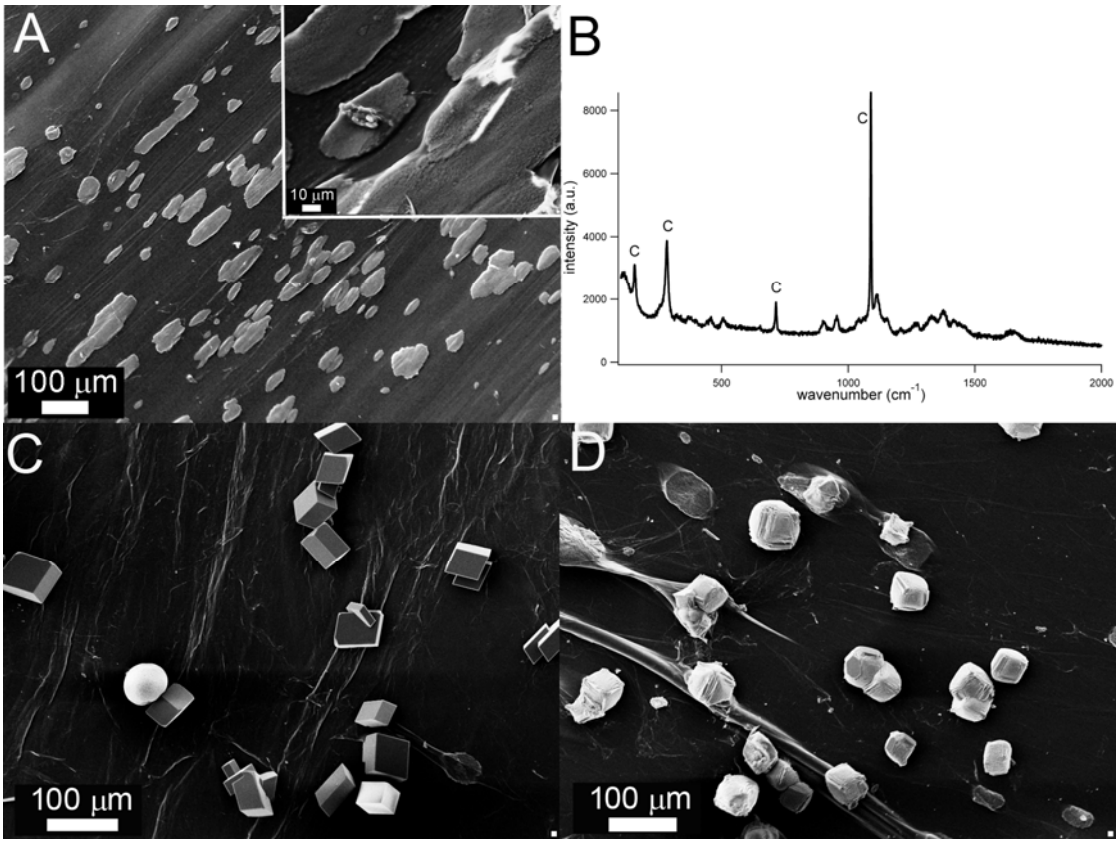

Figure 2.4 Calcium carbonate crystallization on β-chitin (A) SEM micrograph with magnified inset of crystals grown with p-Glu. (B) Raman spectrum of crystals grown with p-Glu. Characteristic calcite peaks are designated by *C*'s on the graph. SEM micrographs (C) with 10 μM AP7N and (D) with 10 μM AP24N.

2.3.2 Effect of the molecular structure of the substrate on polymorph selection.

To investigate the specificity of the surface for determining polymorph selectivity, I ran parallel assays using α-chitin + n16 peptide combinations (Table 2.1, see Figure 1.7 for the structure of α- versus β-chitin). Compared to the parallel repeat structure of β-chitin, α-chitin features an anti-parallel chain repeat. Using α-chitin, I observed that the majority of crystals grown in the presence of all three n16 peptides are calcite, with many calcite crystals being elongated along the *c*-axis (Figure 2.5). As compared to the β-chitin surfaces, α-chitin nucleated very few crystals. In addition to the calcite crystals, I observed small mineral particles on the α-chitin surfaces, which are presumably amorphous calcium carbonate (ACC), that were not observed on β-chitin (Figure 2.5B). As further controls for surface functionality, self-assembled monolayers (methyl and carboxylate-terminated SAMs) of alkanethiols on gold were also tested within this experimental assay. All combinations of the nacre-specific peptides and SAMs yielded randomly oriented calcite, whose rhombohedral morphologies are comparable to control calcite crystals (Figures 2.6, 2.7, and 2.8) while p-Glu results in polycrystalline calcite (Figure 2.8C).

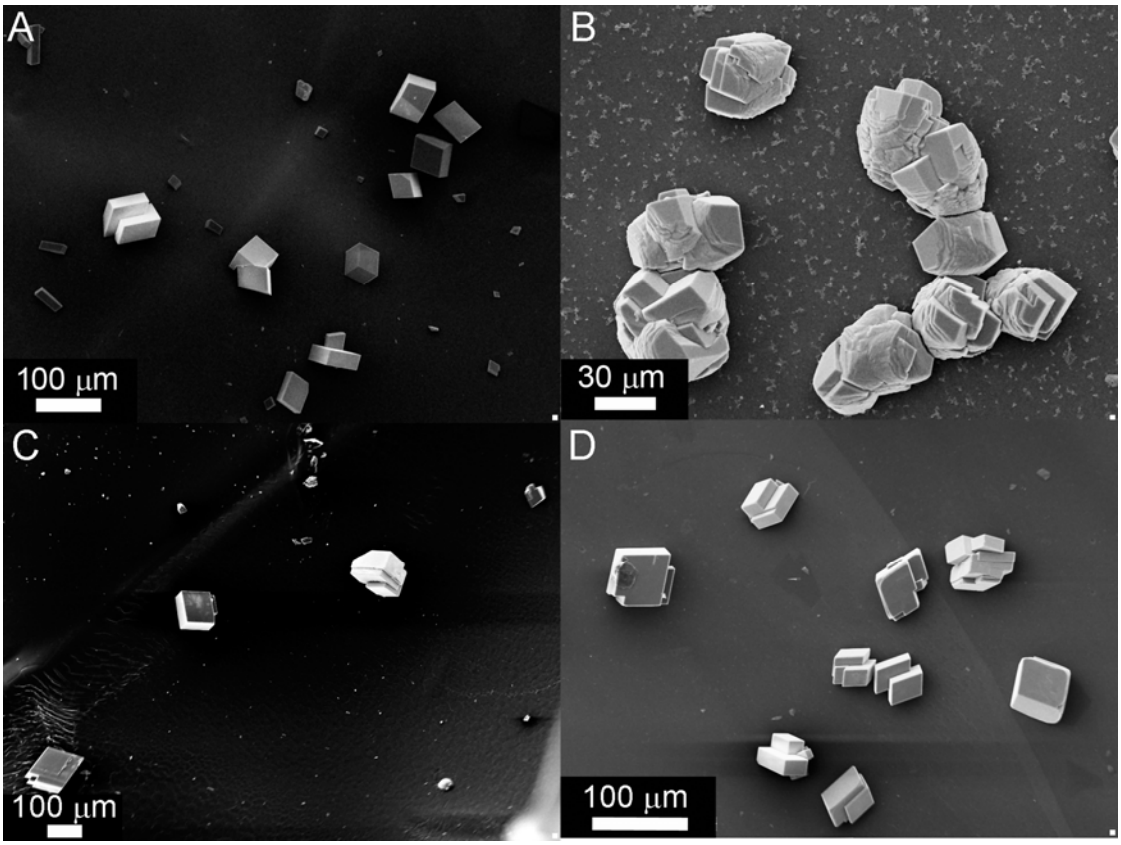

Figure 2.5 SEM micrographs of crystallization studies on α-chitin substrates with (A) no additives (control), (B) n16N, (C) n16NN, and (D) n16Ns. All crystals are calcite, except smaller mineral particulates in (B) may be amorphous calcium carbonate. All peptide concentrations were 10 μM, and Ca^{2+} concentrations were 10 mM.

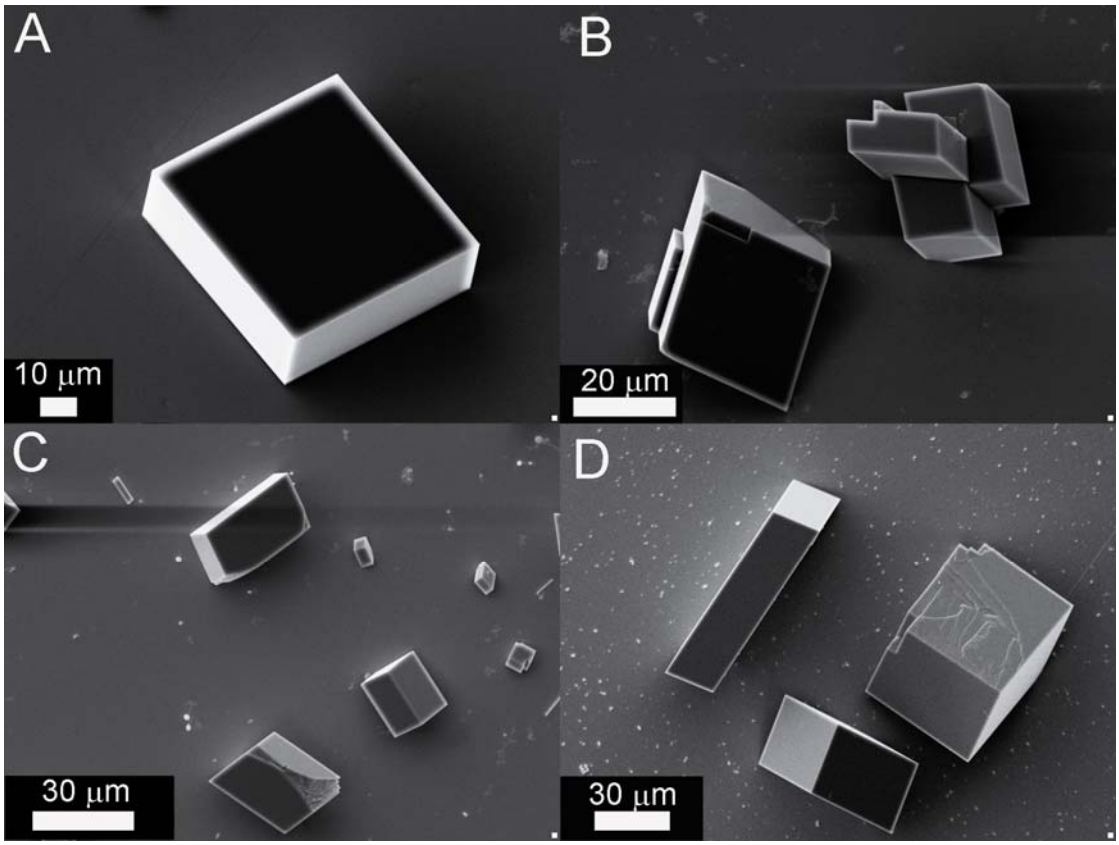

Figure 2.6 SEM micrographs of crystallization studies with n16N and SAMs with the following functionalities: (A) control (without n16N and functionality) (B) none (C) carboxylic acid and (D) methyl. All peptide concentrations are 10 μM.

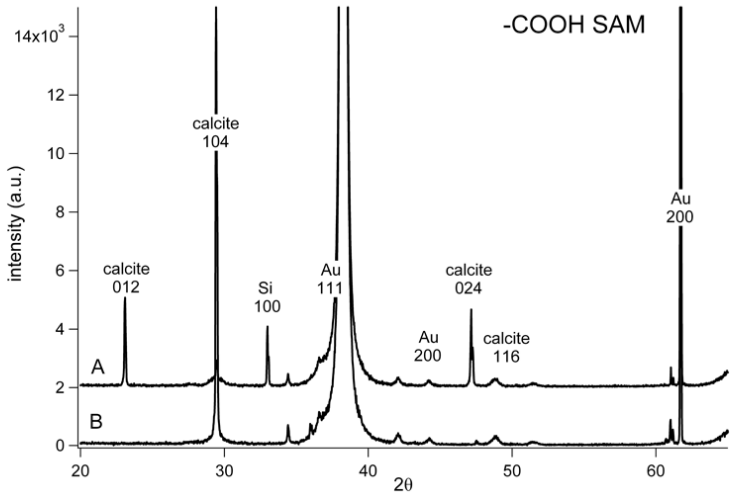

Figure 2.7 XRD spectra of crystals grown on a carboxylic acid terminated SAMs with and without the addition of the n16N peptide.

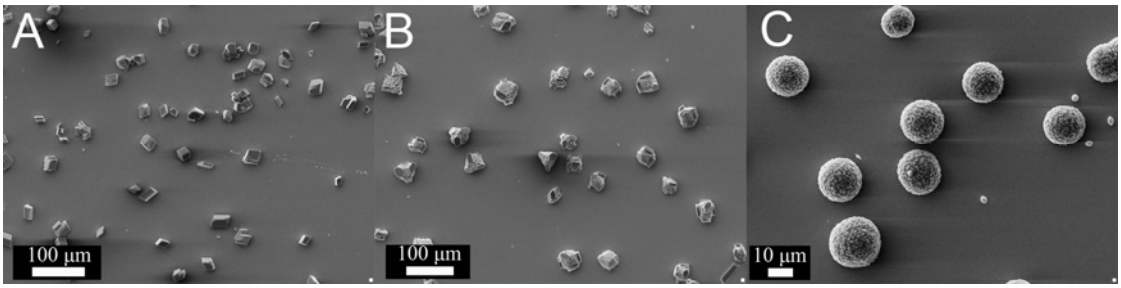

Figure 2.8 SEM micrograph of crystals grown on a carboxylic acid terminated SAM with the addition of (A) AP7N, (B) AP24N, and (C) p-Glu. All peptide concentrations are 10 µM.

2.3.3 Peptide – polysaccharide binding studies.

To investigate the binding of n16N to both α- and β-chitin, fluorescence labeling was used to image the peptides bound to the different surfaces (Figure 2.10 and Table 2.1). The peptides were adsorbed onto the surfaces, washed, and labeled using a maleimide fluorescent dye, BODIPY FL. BODIPY was chosen for the

experiments due to its ability to selectively bind to the Cys groups in the peptide and not to the chitin surface. In addition, BODIPY is a neutrally charged dye, which will minimally affect the pI of the peptide as well as limit any non-specific labeling due to charge interactions between the peptide and the dye.[28]

Prior to labeling, the α- and β-chitin substrates were imaged by fluorescence microscopy to quantify substrate auto-fluorescence (Figure 2.9). After labeling, the β-chitin surface incubated with n16N peptide fluoresces at all brightness levels above the auto-fluorescence level of β-chitin (>50 pixel brightness level, Figure 2.10), indicating that n16N binds to the β-chitin substrate. The peptide variants n16NN and n16Ns bind to lesser degrees. The n16NN has a similar mid-range fluorescence (100-150 pixel levels) as n16N, but does not have the brighter regions present in the n16N samples (>175). The n16Ns peptide does not fluoresce as brightly as either the n16N or n16NN and, therefore, it is likely that n16Ns does not bind as effectively to the chitin substrates. All α-chitin samples have little to no fluorescence, suggesting poor binding interactions between the peptides and this polysaccharide surface as compared to β-chitin (Figure 2.10).

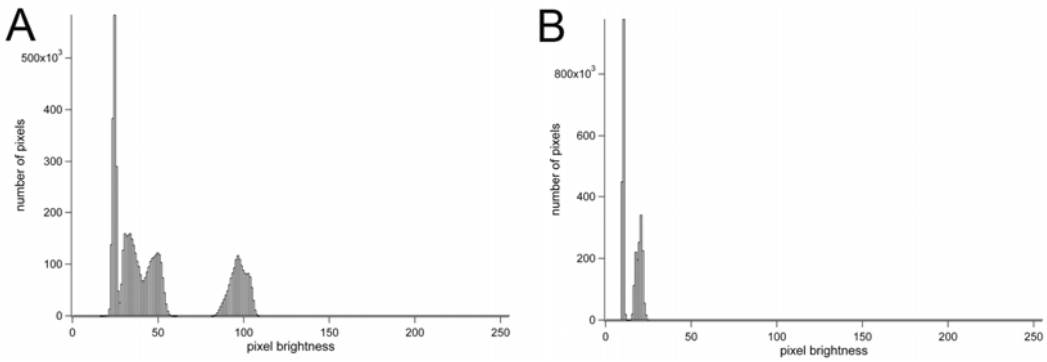

Figure 2.9 Histograms quantifying the auto-fluorescence of β-chitin (A) and α-chitin (B) without the adsorption of any peptide or dye.

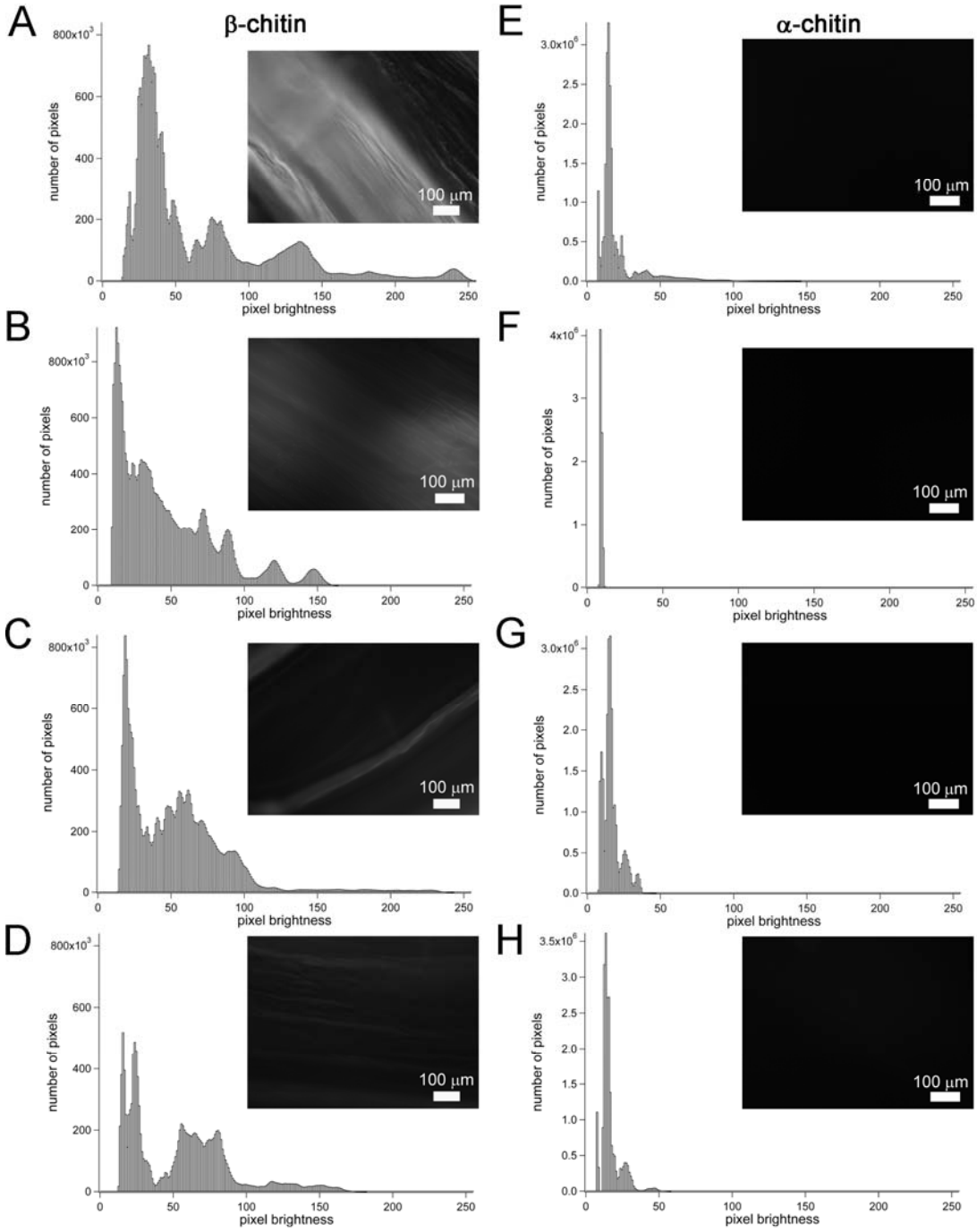

Figure 2.10 Representative fluorescence micrographs and summed histograms compiled from triplicate experiments of chitin substrates incubated with n16N (A & E), n16NN (B & F), n16Ns (C & G), and BSA (D & H). The left column (A, B, C, and D) are β-chitin and the right column are α-chitin (E, F, G, and H). All images were taken at the same exposure time and camera gain.

In parallel assays, bovine serum albumin (BSA) was used as a negative control; with proper washing techniques, BSA should be removed from β-chitin surfaces (Figure 2.10D and H).[8, 29, 30] I found that after treatment of α- and β-chitin with BSA, both substrates fluoresce weakly (barely above the auto-fluorescence of the substrate itself, Figure 2.9). This result suggests that most of the BSA has been removed from the substrates during the washing procedure. While it does appear that some non-specifically bound BSA is still present on the chitin surface after washing, note that the n16N fluorescence on β-chitin is much greater compared to the BSA fluorescence signal. The reader should be aware that BSA has 35 Cys residues compared to the 3 Cys found in n16N and its variants. Thus, even if trace amounts of BSA do survive the washing procedure, a significant background signal will still be detected. To check this, another nacre protein sequence, AP24N (contains 1 Cys residue/30 AA)[31] was utilized in my peptide-chitin adsorption/washing experiments. Here, I found that AP24N does not fluoresce on either chitin substrate and, therefore, does not have a significant binding ability (Figure 2.11).

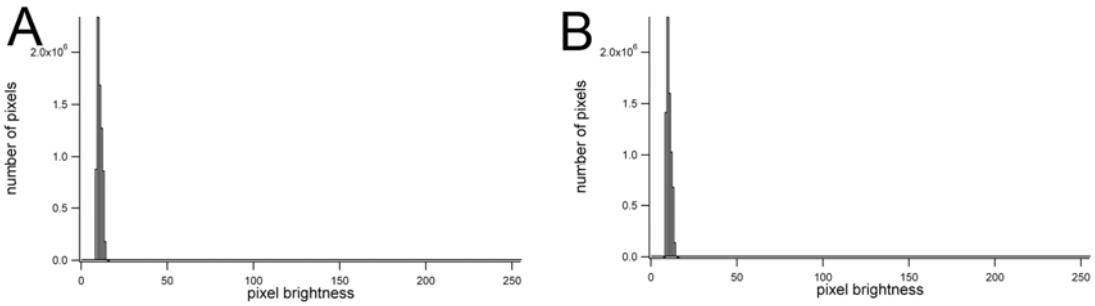

Figure 2.11 Histograms of fluorescence data of β-chitin (A) and α-chitin (B) incubated with AP24N.

2.4 Discussion

This study demonstrates that cooperative interactions between an insoluble matrix (i.e., β-chitin) and a hydrophilic nacreous matrix protein sequence (i.e., n16N) lead to polymorph selectivity *in vitro*. The binding of n16N to β-chitin and the resultant nucleation and growth of aragonite, suggests that the n16 protein is an interactive matrix protein, which may promote the growth of aragonite crystals in the nacreous layer of the mollusk shell. In the experiments presented here, the combination of β-chitin + n16N is required for polymorph selectivity; the separate components alone are not capable of nucleating aragonite. It has been shown that β-chitin has the correct epitaxial match with aragonite but not the correct chemistry,[32, 33] therefore, n16 is necessary to interact with chitin to form a new molecular interface capable of controlling polymorph selectivity.

The intrinsic disorder of the n16N sequence[13] is probably a key factor that allows this peptide to simultaneously interact with β-chitin and the nucleating mineral phase. It is known that intrinsically disordered protein (IDP) sequences can bind to multiple targets[15-19] and in some cases the conformation of the protein sequence is target-dependent. Previous work has demonstrated that n16N modulates the growth of calcite by changing its morphology, and thus can interact with calcium carbonates.[12, 14] This work now establishes that n16N is capable of a second interaction: with β-chitin. The specificity of n16N for β-chitin (over α-chitin) suggests that this IDP sequence can discriminate between polysaccharide chains.

I suggest that the unstable, partially unfolded structure of n16N facilitates interactions with β-chitin, such that internal stabilization (i.e., folding) of the n16N sequence occurs upon binding. Subsequently, the binding of n16N to β-chitin could trigger a polypeptide disorder-to-order transition,[15-19] which may then lead to a rearrangement of the n16N side chain groups. In turn, this new arrangement of

chemical groups may favor the nucleation of aragonite. The fact that n16N undergoes side chain rearrangement upon binding to calcite[20] lends support to this proposal. Whether the n16N peptide becomes ordered on the β-chitin surface, and the arrangement of n16N polypeptide chemical groups required to nucleate aragonite is currently not known.

The two n16N variants, n16NN and n16Ns, were useful for studying the effects of charge and sequence of the peptide, respectively, on polymorph selectivity. These variants also shed light on the molecular requirements for β-chitin binding and inorganic phase selection. The Asn and Gln substituted n16NN variant, which has an α-helical structure,[22] retains the β-chitin binding capability but not at the same level as the random-coil/β-strand n16N. This result suggests that the peptide's secondary structure, which is influenced by the anionic groups, plays a role in mediating the binding interaction between the peptide and the β-chitin. Crystallization studies conducted with n16NN + β-chitin show a reduction in aragonite nucleation, accompanied by the appearance of vaterite and calcite crystals, as compared to the matrix formed with the n16N. This result suggests that the absence of anionic groups (though crystallization results with p-Glu on β-chitin demonstrated that more than a negative charge is necessary for polymorph selectivity) and the loss of intrinsic disorder in the n16NN peptide reduce the ability of this peptide to selectively nucleate aragonite over calcite and vaterite.

The random coil n16Ns + β-chitin matrix primarily leads to the growth of calcite, which is consistent with previous mineralization studies with n16Ns.[14, 22] This loss of polymorph selectivity, coupled with the observed reduction in n16Ns affinity for β-chitin, also indicates that the linear arrangement of amino acids is critical for IDP – target interactions. Given that n16Ns is disordered, similar to n16N,[22] I speculate that the loss of chitin binding and polymorph selectivity may be attributed to

sequence scrambling affecting n16Ns' IDP disorder-to-order transformation (or lack thereof) upon chitin binding.[15-19] Alternatively, since the linear positions of the Cys residues have changed in n16Ns compared to n16N, it is possible that the labeling efficiency of n16Ns by the fluorescence dye may have been altered relative to n16N, resulting in decreased fluorescence signal for the n16Ns + β-chitin combination. The change in Cys positions, though, would have no effect on polymorph selectivity.

To date, only two macromolecules from mollusks have been characterized to possess β-chitin binding capability: Prismalin-14 and Prisilkin-39.[8, 30] This work demonstrates that n16 can be added to this list. I have shown that n16N interacts more favorably with β-chitin than α-chitin, and that this interaction leads to aragonite nucleation on β-chitin only. The binding of n16N to β-chitin may help to explain the role of the full length protein, n16, in polymorphic control over calcium carbonate nucleation and growth. As previously discussed, n16N is an IDP and I speculate that there is a disorder-to-order transformation upon binding to the β-chitin, such that the chitin structures the protein and exposes anionic functional groups with the proper arrangement/orientation to nucleate aragonite. The new interface (with the n16N peptide), however, is not structured enough to produce oriented aragonite crystals, as observed in nacre. A recent report suggests that n16 is part of a larger protein complex and it is possible that other components from this cluster are responsible for the oriented growth.[6]

In summary, I have demonstrated that a 30 AA N-terminal nacreous protein sequence, n16N, exhibits β-chitin binding activity and aragonite phase selectivity *in vitro* without the need for additional additives other than β-chitin. The n16N + β-chitin complex presents a molecular interface that is able to promote the preferential formation of aragonite. Further studies will establish the orientation and structure of n16N on β-chitin, as well as the side chain groups responsible for aragonite selectivity

and β-chitin - peptide affinity. This *in vitro* system can be further increased in complexity to probe the role of other matrix components in controlling not only polymorph, but also crystal morphology and orientation. The interaction of other matrix elements (i.e., silk fibroin hydrogels), in this system, will be explored in subsequent chapters.

2.5 Materials and Methods

2.5.1 Peptide Synthesis and Purification

The 30-mer polypeptide, n16N, representing the 1-30 AA domain of native n16 (Table 2, was synthesized using the protocol described in earlier work.[12-14] The 30 AA randomly scrambled version of n16N (n16Ns), and the globally substituted Asp → Asn, Glu → Gln version, n16NN were also synthesized and purified as described (Table 2.2).[22] All three peptides were synthesized in the C-amide "capped" form. Poly-L-glutamic acid (Sigma-Aldrich) was used without further purification.

Table 2.2 Nacre n16 polypeptide sequences

Designation	Primary Sequence[1]
n16N	AYHKKCGRYSYCWIPYDIERDRYDNGDKKC
n16Ns	EPRYCKWCDNKHGDRAGCKYSIDYYKIRDY
n16NN	AYHKKCGRYSYCWIPYNIQRNRYNNGNKKC

[1]For clarity cationic amino acid residues are highlighted in blue, anionic residues are highlighted in red, and Cysteine residues are highlighted in green.

AP7N (DDNGNYGNGMASVRTQGNTYDDLASLISYL) and AP24N (ADDDEDASSGLCNQYNQNVTTRPNNKPKMF) were synthesized using the protocol described in earlier work.[26] Poly-L-glutamic acid (Sigma-Aldrich) was used without further purification.

2.5.2 Chitin Purification/Preparation

The β-chitin from the pen of the *Loligo* species of squid was purified by refluxing the pen in 1M sodium hydroxide (NaOH) solution for 3 days, changing the NaOH purifying solution daily.[1, 23, 25] The polysaccharide was then extensively washed with DI water and stored dry until use. The β-chitin substrates were rehydrated in 10 mM $CaCl_2$ solutions for a minimum of 2 hours prior to crystallization studies.[1]

For studies involving α-chitin, chitosan films were obtained by evaporation of a solution of 1.25 w/v% chitosan (medium molecular weight, Sigma) in 1% acetic acid.[23, 24] The solution was filtered and placed on glass cover slips and air dried at room temperature. Films were immersed in a solution of dilute ammonia in methanol (15 mL NH_4OH 33%, 35 mL DI water, 500 mL methanol) for 1 hour to regenerate the free amino form of chitosan.[24] The chitosan films were then reacted with 1 M acetic anhydride in methanol for 6 hours on a rocking table at room temperature to acetylate the chitosan to form regenerated α-chitin.[23] The reaction was terminated by removal of the films from the reaction solution, washing with methanol, then water, and air drying. N-acetylation of chitosan was verified by FTIR (not shown).[34] Films were stored dry at room temperature until use.

2.5.3 Crystallization experiments

Crystal growth experiments were carried out using a 24 well plate (Nunc, non-treated multi-dishes) mini-desiccator via the vapor diffusion method. Solid ammonium carbonate ($(NH_4)_2CO_3$, Sigma) was placed in one corner of the plate and covered with crystallization tape (Fisherbrand Adhesive Plate Seals) with one small hole poked in the center. Solid, anhydrous calcium chloride ($CaCl_2$, Sigma) as well as aqueous, 7 mM $CaCl_2$ (high purity calcium chloride dihydrate was used for solution crystal growth, Sigma) were placed in between the carbonate source and the crystallization experiment wells to slow diffusion and prevent condensation from forming within the

sealed 24 well plate. 1 cm^2 substrates were put in the bottom of the crystallization wells and covered with 0.5 mL of solution of 10 mM $CaCl_2$ and 10 μM peptide (controls are without the presence of peptide). The plate perimeter was then sealed with Parafilm®. Crystallization experiments were carried out at room temperature for 24 hours, after which substrates were removed, rinsed with DI water, and dried before characterization. All crystallization experiments were done in triplicate, in 3 separate mini-desiccators.

2.5.4 Morphology and Polymorph Analysis

The morphology of the grown crystals was examined via scanning electron microscopy (SEM, Leica Stereoscan 440, 15 kV, 900 pA) after they were coated with a thin layer of Au/Pd. For each set of conditions, greater than 250 crystals were counted from SEM images among the 3 experiments, and the percentage of each polymorph calculated. The polymorph of the crystals was determined via Raman (Renishaw InVia micro-Raman system, 785 nm excitation frequency) and x-ray diffraction (Bruker General Area Detector System, transmission mode, 40 kV, 40 mA or Scintag Theta-Theta Diffractometer, $CuK_{\alpha 1}$ radiation, 45 kV, 40 mA, 4.00 deg/min scan rate).

2.5.5 Adsorption experiments

Chitin substrates were incubated with 5 μM solutions of n16N or bovine serum albumin (BSA, Fisher Scientific) on a rocking table at room temperature for 24 hours to allow the peptide/protein time to adsorb from the solution onto the chitin substrate. After 24 hours, substrates were washed with DI water, saline solution (0.2 M NaCl), buffer (10 mM Tris, pH 7.2), and finally DI water again to remove any unbound peptide/protein. Substrates were immediately used for crystal growth or fluorescence experiments.

2.5.6 Fluorescence experiments

Substrates with adsorbed peptide were reacted with BODIPY FL *N*-(2-aminoethyl) maleimide (Invitrogen) according to manufacturers instructions with the following modifications: nitrogen purged 10 mM Tris buffer (pH 7.2) and 1 μM Tris (2-carboxy-ethyl) phosphine hydrochloride (TCEP, Sigma) was added to each sample and reacted for 30 minutes to reduce any disulfides prior to the addition of the maleimide dyes. After 30 minutes, 1 μM dye is added to the reaction solution and reacted for 2 hours at room temperature on a rocking table. All dyeing steps were performed in a dark, oxygen minimum environment to reduce the chance of disulfide formation as well as photobleaching of the dyes before fluorescence imaging could be carried out. After the reaction was complete, the samples were extensively rinsed to remove excess dye and imaged.

Specimens were imaged via fluorescence microscopy (Olympus BX51 equipped with a Roper Cool Snap CCD Camera, 100 msec exposure time). A mercury lamp with a "green" filter (λ_{ex} = 460-500 nm, λ_{em} = 510-560 nm, Dichroic filter = 505 nm) was used for fluorescence imaging. A neutral density filter was used to reduce the intensity of the mercury lamp by 25%. All images were recorded in grayscale (12 bit image, capture area 1394 x 1040 pixels, gain of 1, and 1 x 1 binning) and were scaled to the same intensity values using the Image Pro imaging software package. Histograms were made in ImageJ to quantify fluorescence brightness distributions among grayscale sample images, white was assigned 256 and black was assigned 0 by ImageJ with all levels of gray in between. All fluorescence experiments were done in triplicate.

REFERENCES

1. Falini, G.; Albeck, S.; Weiner, S.; Addadi, L., *Science* **1996,** 271, (5245), 67-69.

2. Bevelander, G.; Nakahara, H., *Calcif. Tissue Res.* **1969,** 3, (1), 84-92.

3. Levi-Kalisman, Y.; Falini, G.; Addadi, L.; Weiner, S., *J. Struct. Biol.* **2001,** 135, (1), 8-17.

4. Belcher, A. M.; Wu, X. H.; Christensen, R. J.; Hansma, P. K.; Stucky, G. D.; Morse, D. E., *Nature* **1996,** 381, (6577), 56-58.

5. Gotliv, B. A.; Addadi, L.; Weiner, S., *ChemBioChem* **2003,** 4, (6), 522-529.

6. Suzuki, M.; Saruwatari, K.; Kogure, T.; Yamamoto, Y.; Nishimura, T.; Kato, T.; Nagasawa, H., *Science* **2009,** 325, (5946), 1388-1390.

7. Suzuki, M.; Murayama, E.; Inoue, H.; Ozaki, N.; Tohse, H.; Kogure, T.; Nagasawa, H., *Biochemistry Journal* **2004,** 382, 205-213.

8. Kong, Y.; Jing, G.; Yan, Z.; Li, C.; Gond, N.; Zhu, F.; Li, D.; AZHang, Y.; Zheng, G.; Wang, H.; Xie, L.; Zhang, R., *J. Biol. Chem.* **2009,** 284, (16), 10841-10854.

9. Samata, T.; Hayashi, N.; Kono, M.; Hasegawa, K.; Horita, C.; Akera, S., *FEBS Lett.* **1999,** 462, (1-2), 225-229.

10. Bedouet, L.; Marie, A.; Dubost, L.; Peduzzi, J.; Duplat, D.; Berland, S.; Puissegur, M.; Boulzaguet, H.; Rousseau, M.; Milet, C.; Lopez, E., *Mar. Biotechnol.* **2007,** 9, (5), 638-649.

11. Marin, F.; Luquet, G., *C. R. Palevol* **2004,** 3, (6-7), 469-492.

12. Kim, I. W.; DiMasi, E.; Evans, J. S., *Cryst. Growth Des.* **2004,** 4, (6), 1113-1118.

13. Collino, S.; Evans, J. S., *Biomacromolecules* **2008,** 9, (7), 1909-1918.

14. Kim, I. W.; Darragh, M. R.; Orme, C.; Evans, J. S., *Cryst. Growth Des.* **2006,** 6, (1), 5-10.

15. Oldfield, C. J.; Cheng, Y.; Cortese, M. S.; Brown, C. J.; Uversky, V. N.; Dunker, A. K., *Biochem. J.* **2005,** 44, (6), 1989-2000.

16. Xie, H. B.; Vucetic, S.; Iakoucheva, L. M.; Oldfield, C. J.; Dunker, A. K.; Uversky, V. N.; Obradovic, Z., *J. Proteome Res.* **2007,** 6, (5), 1882-1898.

17. Dunker, A. K.; Oldfield, C. J.; Meng, J.; Romero, P.; Yang, J. Y.; Chem, J. W.; Vacic, V.; Obradovic, Z.; Uversky, V. N., *BMC Genomics* **2008,** 9, 1-26.

18. Delak, K.; Collino, S.; Evans, J. S., *Biochem. J.* **2009,** 48, (16), 3669-3677.

19. Delak, K.; Harcup, C.; Lakshminarayanan, R.; Sun, Z.; Fan, Y. W.; Moradian-Oldak, J.; Evans, J. S., *Biochem. J.* **2009,** 48, (10), 2272-2281.

20. Metzler, R. A.; Kim, I. W.; Delak, K.; Evans, J. S.; Zhou, D.; Beniash, E.; Wilt, F.; Abrecht, M.; Chiou, J. W.; Guo, J. H.; Coppersmith, S. N.; Gilbert, P., *Langmuir* **2008,** 24, (6), 2680-2687.

21. Metzler, R. A.; Evans, J. S.; Killian, C. E.; Zhou, D.; Churchill, T. H.; Appathurai, N. P.; Coppersmith, S. N.; Gilbert, P. U. P. A., *J. Am. Chem. Soc.* 10.1021/ja909735y.

22. Delak, K.; Collino, S.; Evans, J. S., *Langmuir* **2007,** 23, (24), 11951-11955.

23. Falini, G.; Weiner, S.; Addadi, L., *Calcif. Tissue Int.* **2003,** 72, (5), 548-554.

24. Chatelet, C.; Damour, O.; Domard, A., *Biomaterials* **2001,** 22, (3), 261-268.

25. Darmon, S. E.; Rudall, K. M., *Discuss. Faraday Soc.* **1950**, (9), 251-260.

26. Wustman, B. A.; Morse, D. E.; Evans, J. S., *Biopolymers* **2004,** 74, (5), 363-376.

27. Kim, I. W.; Morse, D. E.; Evans, J. S., *Langmuir* **2004,** 20, (26), 11664-11673.

28. Tyagarajan, K.; Pretzer, E.; Wiktorowicz, J. E., *Electrophoresis* **2003,** 24, (14), 2348-2358.

29. Weiss, I. M.; Schonitzer, V., *J. Struct. Biol.* **2006,** 153, (3), 264-277.

30. Suzuki, M.; Nagasawa, H., *FEBS J.* **2007,** 274, (19), 5158-5166.

31. Michenfelder, M.; Fu, G.; Lawrence, C.; Weaver, J. C.; Wustman, B. A.; Taranto, L.; Evans, J. S.; Morsel, D. E., *Biopolymers* **2003,** 70, (4), 522-533.

32. Weiner, S.; Traub, W., *FEBS Lett.* **1980,** 111, (2), 311-316.

33. Weiner, S.; Talmon, Y.; Traub, W., *Int. J. Biol. Macromol.* **1983,** 5, (6), 325-328.

34. Baxter, A.; Dillon, M.; Taylor, K. D. A.; Roberts, G. A. F., *Int. J. Biol. Macromol.* **1992,** 14, (3), 166-169.

CHAPTER 3

HYDROGELATION OF SILK FIBROIN: THE EFFECT OF PURIFICATION METHOD

3.1 Abstract

This chapter evaluates hydrogel formation by silk fibroin solutions purified from silkworm cocoons by three purification methods: deionized water (pH 6.5), 5 w.v% Marseilles soap (pH 8.25), and 0.02 M Na_2CO_3 (pH 10.5). The primary aim of the purification is to remove silk sericin, the main contaminate, with minimal hydrolysis to the silk fibroin protein. Depending on the purification method used, the kinetics of hydrogel formation and the rheology of the final hydrogels varied. The fibroin purified with Marseilles soap and water produced the stiffest hydrogels with higher yield stresses than the Na_2CO_3 purified material. These two gels also formed more quickly than the gel formed from Na_2CO_3 purified silk. The macroscopic kinetics of gelation, as monitored by CD spectroscopy, is correlated with a random coil to β-sheet transformation of the fibroin protein chains. The morphological and structural characteristics of freeze dried gel samples were assessed by SEM and XRD respectively. Possible explanations for variations among the samples are that the three purification methods differ in the amount of sericin removed (quantified by mass loss and Direct Red 80 Staining) and the degree of degradation of the fibroin protein (assessed by SDS-PAGE): water was ineffective at removing sericin but does minimal damage to the fibroin protein; Na_2CO_3 removed all of the sericin but also hydrolyzed the fibroin into shorter protein chains; Marseilles soap was as effective at removing sericin as Na_2CO_3 but with less hydrolysis of the fibroin. Based on these trends, I conclude that the purification method of silk fibroin is a key variable in determining

the characteristics of the resulting silk fibroin hydrogels. This work suggests that for applications involving silk fibroin hydrogels, the choice of purification method is a key factor in determining the final properties of the gel.

3.2 Introduction

As discussed in Chapter 1, a silk fibroin-like protein hydrogel plays an important role in the formation of nacre. Therefore, to clarify the role of this biomolecule in biomineralization, reproducible silk fibroin hydrogels with specific properties (i.e., secondary structure or viscoelasticity), must be utilized in synthetic systems.

Silk fibroin from *Bombyx mori* (silkworms) is processed into a variety of structures including fibers, films, and hydrogels. This versatility leads to diverse applications of silk in textiles, medical implants,[1-3] tissue engineering,[1, 4, 5] and biomineralization.[6-10] Aqueous solutions of silk readily form hydrogels under a variety of conditions including heat,[11] application of shear stress,[12, 13] treatment with methanol,[14, 15] or decreasing pH.[16-18] The hydrophobic regions of random coil silk fibroin assemble in aqueous solutions via hydrophobic interactions and organize into β-sheets, physically cross-linking the hydrogels.[17, 19] These hydrogels are viscoelastic, polymer networks whose biocompatibility,[1, 2] biodegradability,[20] and mechanical properties[21-23] make them ideal candidates as biomaterials. In this chapter I examine the effect of three different purification methods of silk fibroin on the properties of the resulting hydrogels for later use in *in vitro* experiments discussed in subsequent chapters.

Silkworm cocoons are composed of silk fibroin (a hydrophobic protein) and silk sericin (a mixture of hydrophilic polypeptides), which account for approximately

75 and 25 wt% of the native silk, respectively.[24] The structure of silk fibroin has been extensively studied using X-ray diffraction,[25-27] electron diffraction and microscopy, [11, 28, 29] infrared spectroscopy,[16, 25-28] NMR spectroscopy,[25-27] and circular dichroism spectroscopy.[30-34] Silk fibroin, extracted *in vivo* from silk-producing glands in silkworms, contains heavy and light polypeptide chains, of ~350 kDa and ~25 kDa, respectively, connected together by disulfide linkages. The heavy chain is largely constructed from repeating sequences of glycine, alanine, and serine (GAGAGS), along with a high tyrosine content.[25, 35]

Before silk fibroin is used for most applications (especially biomedical purposes) the immunogenic sericin is removed to improve the properties as well as the biocompatibility of the silk materials.[2] Silk sericin content has previously been shown to influence the characteristics of regenerated silk fibers by retarding the crystallization process of silk fibroin, increasing the total β-sheet content of the regenerated silk, and increasing the tensile strength of individual fibers.[36, 37] There are many methods, which require harsh chemical conditions, to degum (remove the sericin) and to solubilize the silk fibroin from silkworm cocoons.[9, 11, 28, 35, 38-41] Typically, cocoons are boiled in an alkaline degumming solution, sometimes with the addition of surfactants, to remove the silk sericin. Sericin removal is thought to occur via several mechanisms including base hydrolysis of the sericin polypeptides and solubilization of the sericin by surfactants.[38, 40] The use of different purification methods can cause inconsistencies among reports regarding the characteristics of the silk fibroin (e.g., molecular weight and β-sheet content) [11, 17, 39] and characteristics of the resulting hydrogels (e.g., kinetics of gelation and rheology).[26, 35, 42]

Here I report a comparison of three representative degumming methods: a neutral solution (water, pH 6.5), a weakly alkaline solution with surfactant (5 w/v% Marseilles soap, pH 8.25), and a strongly alkaline solution with no surfactant (0.02 M

Na_2CO_3, pH 10.5). The clean silk fibroin fibers are then dissolved using chaotropic reagents (usually 9.3 M LiBr), followed by dialysis to remove the salts. In this chapter, gels are formed from the purified silk solutions by heating. I focus on comparing the kinetics of gelation and rheological properties of the resulting gels, and found that the gel properties vary with purification method. These variations may be due to the effectiveness of sericin removal and the degradation of the fibroin protein chains during purification.

3.3 Results and Discussion

3.3.1. Characterization of Silk Hydrogels

3.3.1.1. Gelation

Hydrogels were prepared from solutions of purified silk fibroin (~5 w/v %). Two different gelation methods were investigated: gelation at room temperature and in a 60º C hot water bath.[11] The length of time it takes for the silk solution to gel is dependent on the purification method and the temperature (Table 3.1). Room temperature gelation is slower for all samples as compared to incubation at 60º C. At 60º C, W-gel (gel formed from water purified, method 1, silk solutions) formed the fastest of the three samples, while SC-gel (gel from sodium carbonate, method 3, silk solutions) formed the slowest. At room temperature, the W-gel formed faster than the MS-gel (gel from Marseilles soap, method 2, silk solutions), while the solution from method 3 did not gel, even after 15 days. Upon gelation, the macroscopic appearance of the hydrogels depends on the temperature: solutions that were incubated at 60º C resulted in clear gels, while solutions kept at room temperature formed opaque gels.

Table 3.1 Gelation times and gelation rates as a function of purification method.

Preparation method	degumming agent	Gel name	60° C gelation time (days)[a]	Room temperature gelation time (days)[a]	rate'$_{\beta\text{-sheet}}$, (mdeg mg^{-1} hr^{-1})[b,c]	rate''$_{\beta\text{-sheet}}$, (mdeg mg^{-1} hr^{-1})[b,c]
1	water	W-gel	< 1	2	62.5 ± 11.2	4.5 ± 1.4
2	5 w/v % Marseilles soap	MS-gel	2	9	38.9 ± 9.8	4.3 ± 0.6
3	0.02 M Na_2CO_3	SC-gel	4	> 15	4.2 ± 1.1	1.0 ± 0.5

[a] All silk solutions were 5 ± 0.5 mg/mL

[b] Silk (20 μg/mL) incubated at 60° C in the CD spectrometer.

[c] Slope coefficient values of ellipticity/milligram at 217 nm versus time ± range of values from 2-3 trials calculated by Equation 3.1.

3.3.1.2. CD spectroscopy

Changes in the protein secondary structure during gelation were investigated by variable temperature circular dichroism (CD) spectroscopy. CD spectroscopy measures the differences in the adsorption of left- and right-handed polarized light, which arise due to structural asymmetry within a molecule. Protein secondary structure can be determined by CD in the far UV region (190-250 nm). The CD signal arises from the protein chromophore, the peptide bond. Each secondary structure (α-helix, β-sheet, random coil) has a characteristic shape spectrum, and like all spectroscopic techniques, the CD signal represents an average of the total secondary structure present.[43]

All CD spectra were recorded for diluted (~20 μg/mL) fibroin solutions to obtain good signal to noise ratios. Immediately after dialysis, the CD spectra of all three fresh silk fibroin samples are similar with minima at 195 nm, indicating a random coil conformation (Figure 3.1). Upon gelation, either at room temperature or at 60° C, the CD spectra change to have maxima at 195 nm and minima at 217 nm, indicating the formation of β-sheets (Figure 3.2).

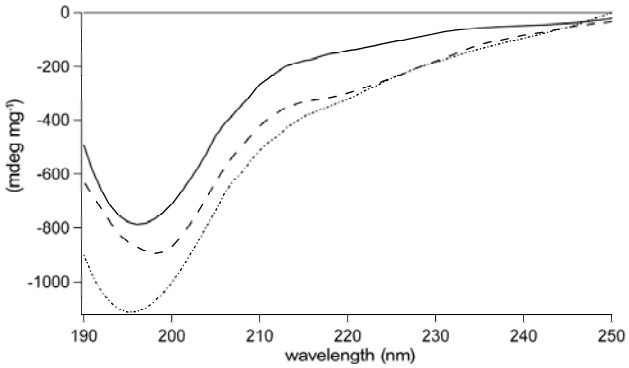

Figure 3.1 CD spectra of fresh silk fibroin samples at 25º C. Water purified fibroin (method 1, 25 μg/mL, ---), Marseilles soap purified fibroin (method 2, 21 μg/mL, ——), and Na_2CO_3 purified fibroin (method 3, 22 μg/mL, ·····).

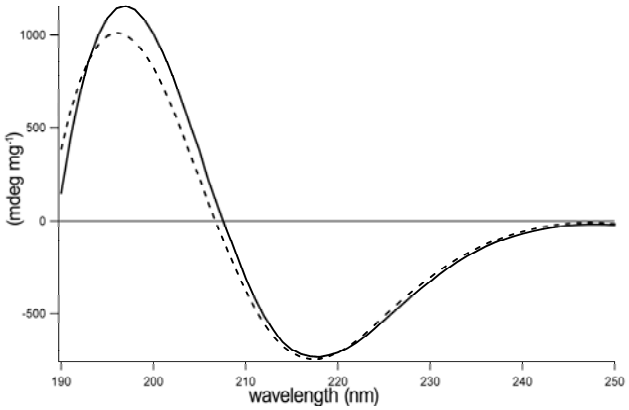

Figure 3.2 Overlay of a diluted silk fibroin heated at 60º C (solid line) for 48 hours and a mature gel aged at 60º C for 48 hours diluted to the same concentration (dashed line). Both samples are Marseilles soap purified silk (20 μg/mL).

CD spectra of fresh, diluted silk solutions (~20 μg/mL), at 60º C, were recorded every hour for 24 hours to monitor the conformational changes of silk fibroin as a function of time (Figure 3.3A). Over time, the conformation changes from a random coil to a β-sheet structure. There is an isosbestic point at 210 nm indicating that there is a two-state transformation from a random coil to a β-sheet structure.

Previous CD studies of fibroin have shown similar results.[32-34] The CD spectrum of a diluted sample, heated in the CD, was compared to the CD spectrum of a mature gel, diluted to the same concentration. These two spectra had similar β-sheet signals (mdeg/mg) which indicates that the diluted and the concentrated solutions underwent similar conformational transformations over time at 60º C (Figure 3.2). The diluted solutions, however, do not form a gel inside of the cuvette.

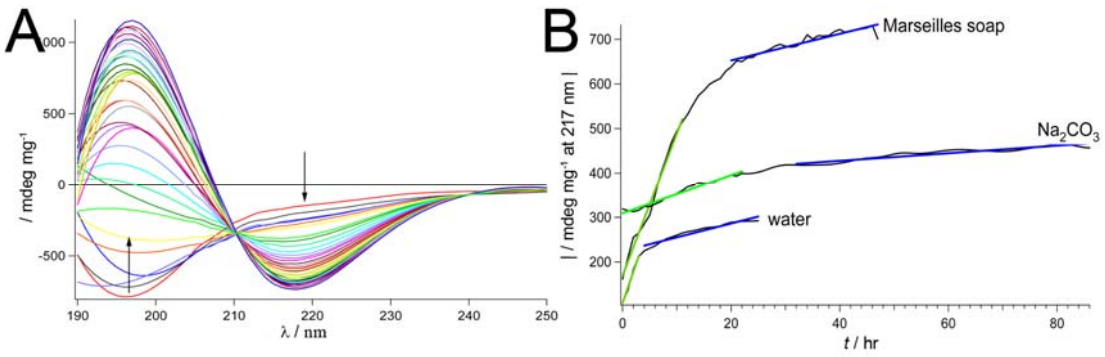

Figure 3.3 (A) Representative CD spectra over time, samples were held at 60º C; Marseilles soap purified silk (method 2), 20 µg/mL, spectra taken every hour for 24 hours. (B) Kinetic experiments at 60º C with method 1 silk (19 µg/mL), method 2 silk (20 µg/mL), and method 3 silk (23 µg/mL) tracing the absolute value of the CD signal at 217 nm over time as the sample is heated at 60º C. Green lines indicate the best fits to region 1 ($rate'_{\beta\text{-sheet}}$) and the blue lines indicate best fits to region 2 ($rate''_{\beta\text{-sheet}}$).

When the evolution of the 217 nm peak is plotted versus time, two distinct rate regimes are evident: fast (region 1) and slow (region 2) (Figure 3.3B).[44] The value of the CD signal (mdeg/mg) at 217 nm is proportional to the concentration of protein with β-sheet character present in solution. From this assumption, the rate of random

coil to β-sheet conversion is proportional to the slope of a linear best fit to each region of Figure 3.3B (equation 3.1)**.**

$$rate_{\beta-sheet} \propto slope \approx \frac{[\beta - sheet]}{time} \qquad [3.1]$$

Region 1 is hypothesized to be associated with the random coil to β-sheet transformation, while region 2 is associated with the slower aggregation of β-sheets into extended networks (Figure 3.4). This mechanism is supported by literature,[17, 32, 45] as well as the kinetic spectra that show two distinct transition regimes. During the slower phase (region 2), the positive absorbance at 197 nm continues to increase indicating that further processes are occurring (Figure 3.3A). The rates of conformational change in dilute solutions (Table 3.1) follow the same trends as the macroscopic gelation times observed for concentrated solutions: W-gel forms the fastest while SC-gel forms the slowest. This correlation between rates further supports the relationship between β-sheet formation and gelation.[17, 46-48]

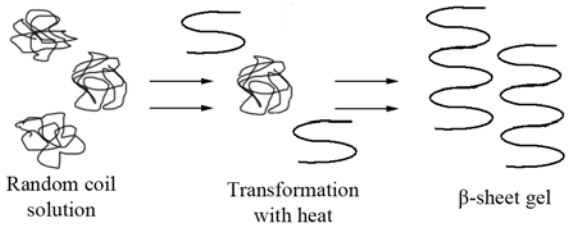

Figure 3.4 Schematic of proposed transformation of silk solutions to gel. Initial structure of protein is entirely random coil, then over time transforms into β-sheet which later aggregate together in anti-parallel β-sheet stacks.

3.3.1.3 X-ray diffraction

Powder x-ray diffraction was used to further investigate the molecular arrangement of the silk hydrogels (Figure 3.5). All freeze dried hydrogels, prepared from silk fibroin solutions (60º C gelation), show two sharp peaks at 9.4º and 28.4º, one broad peak around 20º, and a shoulder around 24º. The 9.4º, 20º, and 24º peaks are indicative of the β-sheet crystalline structure of silk fibroin and correspond to 9.4 Å, 4.3 Å, and 3.7 Å spacing, respectively.[11, 26, 27] The 28.4º peak indicates that there is also another silk structure present which is sometimes seen in the random coil or silk I structure.[30] This peak suggests that the β-sheet content never reached 100% such that there is still residual unfolded (random coil) silk remaining in the hydrogel.

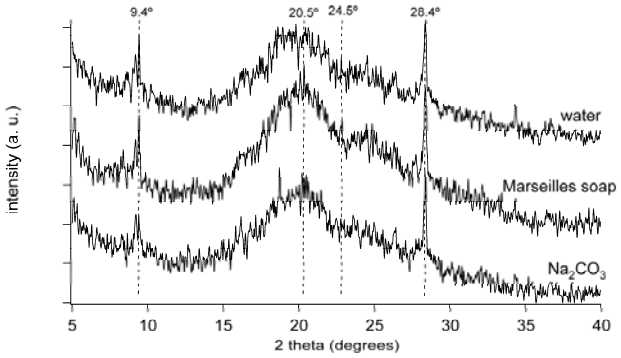

Figure 3.5 X-ray diffraction patterns of freeze dried silk fibroin hydrogels prepared from aqueous silk fibroin solutions at 60º C.

3.3.1.4. Rheology

Rheology was used to characterize the mechanical properties of the gels formed from silk fibroin purified by different methods. Constant stress measurements (frequency sweeps) were performed in the linear viscoelastic region of each gel. These measurements (Figure 3.6) show that the storage and loss moduli (G' and G", respectively) are independent of angular frequency at low frequencies (<10 rad/s), and

over the entire range of frequencies G' > G". Both of these behaviors are characteristic of gel-like, elastic solids.[49] The absolute values of G', or stiffness of the material, demonstrate that the MS-gel is the stiffest gel (~50 Pa) while the SC-gel is the least stiff gel (~6 Pa).

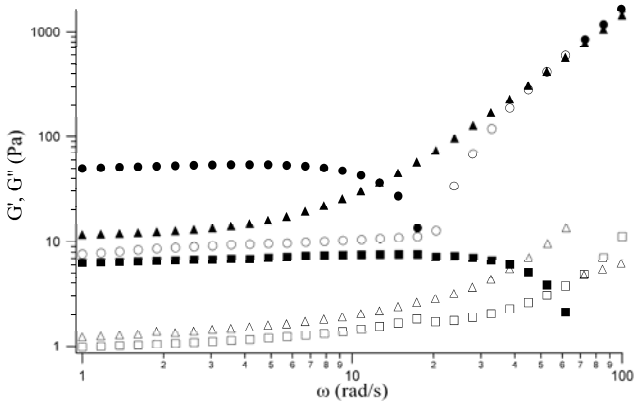

Figure 3.6 Representative frequency sweep of 5 wt% silk fibroin hydrogels at 25º C. Solid shapes denote G' data and empty shapes denote G" data. ▲Δ is water purified gel (W-gel), ●○ is Marseilles soap purified gel (MS-gel), ■□ is Na_2CO_3 purified gel (SC-gel).

The yield stress of a gel is a measure of the robustness of a gel under applied shear.[50] To determine the yield stresses of the three different silk fibroin hydrogels, I performed creep experiments, which monitor the evolution of deformation in the hydrogels over time. In a log-log plot of the viscosity of the gels as a function of shear stress, the yield stress is defined as the stress at which shear thinning begins (Figure 3.7). For the silk fibroin hydrogels, the yield stress is dependent on purification method. W-gel and MS-gel both have a constant viscosity at low stresses (zero-shear viscosity). At the point of shear thinning (yield stress), both the W-gel and MS-gel yield by several orders of magnitude. The plot for the SC-gel is different from the

other two and does not have an obvious zero-shear viscosity or yield stress. Instead, the SC-gel gradually yields to the applied stress. A possible explanation for this behavior is that its zero-shear viscosity occurs at much lower stresses (below the range of the rheometer).[49]

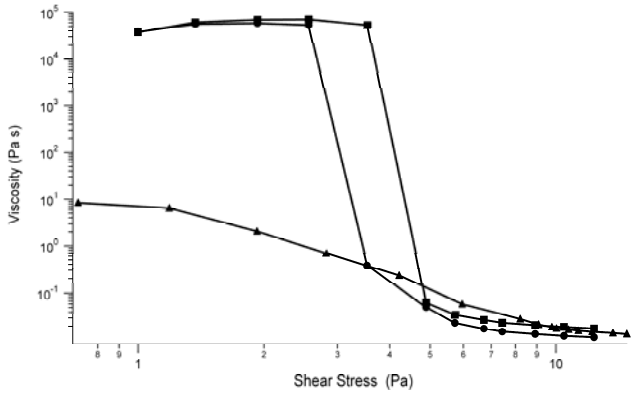

Figure 3.7 Representative log-log plots of viscosity versus shear stress of 5 wt% silk fibroin hydrogels at 25º C. ● water purified silk gel (W-gel), ■ Marseilles soap purified silk gel (MS-gel), and ▲ Na_2CO_3 purified silk gel (SC-gel).

3.3.2 Characterization of Purified Silk Fibroin

The rates of gelation and β-sheet formation, as the silk converts from a solution to a gel, depend on purification method. A gel forms when a polymer in solution can cross-link with other segments (covalently or non-covalently), either on the same chain or other chains.[51] The rate of gelation will depend on the concentration of the polymer solution and the molecular weight of the polymer, which will affect the degree of chain entanglement and number of cross-links. For example, in fibroin gels, β-sheet formation physically cross-links the gels.[17] The presence of residual sericin has been shown to increase β-sheet content in regenerated silk fibers and, therefore,

may also act as a cross-linker and accelerate gel formation.[37] In another study, high molecular weight, undegraded silk fibroin has been shown to gel almost instantaneously.[39]

The yield stresses of the silk fibroin gels also vary with purification method. The rheological properties (i.e., stiffness and yield stress) of a gel depend on the degree of entanglement of the chain networks, which is itself dependent on the number of cross-links, chain length, molecular weight, and concentration of the polymer in solution. [23, 49, 51] The presence of residual sericin has been proven to increase the mechanical strength of silk fibers in comparison to pure silk fibroin (no silk sericin), [37] and thus may also increase the strength of silk fibroin hydrogels. To the best of my knowledge, no studies to date have addressed the relationship between silk fibroin molecular weight and gel strength.

To interpret the kinetic and rheology results in the context of previous studies, I quantified sericin removal by mass loss and Direct Red 80 staining and the degree of degradation of the fibroin protein by SDS-PAGE and light scattering, as a function of purification method.

3.3.2.1. Sericin Removal

I assessed the effectiveness of the three purification methods at removing silk sericin by determining the mass lost during the purification process. The mass lost from degumming includes sericin as well as any dirt associated with the cocoons. When the degummed mass loss was 25 wt%, the silk sericin was considered completely removed.[37, 39] Method 1 removes 18 wt%, while methods 2 and 3 remove ~25 wt% of the original cocoon mass (Table 3.2). During degumming, some small fibers detached from the silk mass and were observed in solution. These fibers were recovered by centrifugation and accounted for in the total mass loss calculation.

Method 3 resulted in a significant amount of recovered fibers (up to 30% of the total mass was recovered fibers) from solution as compared to the other two methods (a few percent). I also used Direct Red 80 (DR 80, a sericin selective dye) to stain the silk fibers and found similar trends to the mass loss data (Figure 3.8, Table 3.2).[40, 52, 53] The concentration of DR 80, determined by UV spectroscopy after dyed silk fibers were dissolved with 9.3 M LiBr to solubilize the stained sericin, is directly related to the amount of silk sericin present in solution (Table 3.2). All samples were compared to stained, untreated cocoons to determine the amount of sericin removed by each degumming treatment. While micro-molar concentration of dye is reported in Table 3.2, the exact amount of sericin removed is unknown. Therefore, DR80 is used to qualitatively see sericin removal and determine relative trends in comparison with mass loss calculations (Figure 3.8).

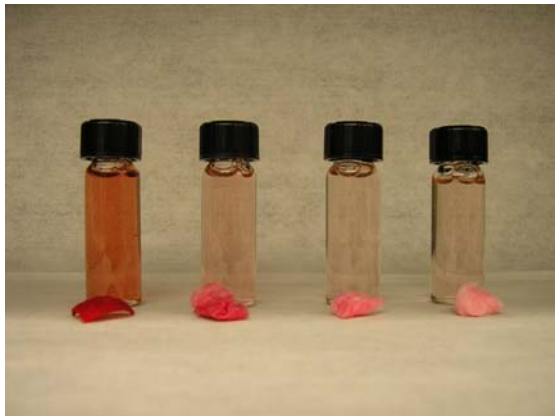

Figure 3.8 Representative Direct Red 80 dyed silk fibroin fibers and dissolved solutions. From left to right are dyed silk fibers of: unpurified, methods 1, 2, and 3.

Table 3.2 Silk sericin removal as a function of purification method.

Preparation method	"degumming" agent	Total mass loss (%)[a]	Concentration DR 80 (μM)[b, c]
cocoons	-	-	51.2 ± 5.5
1	water	18.4 ± 2.5	32.3 ± 1.3
2	5 w/v% Marseilles soap	25.0 ± 3.5	12.4 ± 0.5
3	0.02 M Na_2CO_3	24.6 ± 2.0	11.8 ± 2.1

[a] Average values ± range of values from 3 trials

[b] Average values ± range of values from 2-3 trials

[c] A silk sericin selective dye

The presence of more sericin in the W-gel may explain why the W-gel forms more quickly than either the MS- or SC-gel. The faster gelation of the MS-gel, as compared to the SC-gel, and the lack of gelation of the SC-gel at room temperature, however, cannot be explained by different amounts of residual sericin; mass loss after degumming shows that these samples have equal amounts of sericin (Table 3.2). The yield stresses and the zero-shear viscosities, of the three hydrogels also do not correlate with the amount of residual sericin since the W-gel and the MS-gel show similar mechanical behavior but have different amounts of residual sericin.

3.3.2.2. Protein Degradation

Another possible explanation for the observed differences among the hydrogels is the molecular weight of the silk fibroin protein itself. The high temperatures (~100º C) and alkaline solutions (pH > 8) used in the purification process can promote hydrolysis of the native protein. The degradation of the silk fibroin after the purification processes was evaluated by SEM (condition of the fibers) and by SDS-PAGE and static light scattering (the molecular weights of the fresh silk solutions).

There are qualitative differences in the appearance of the fibers among the three samples (Figure 3.9). Fibers purified with water alone (method 1) are uniform in size, but appear rough, possibly due to residual silk sericin contaminants (Figure 3.9A, white arrows). Cocoons that were boiled in a Marseilles soap solution (method 2) resulted in fibers that were smooth, but were different diameters (Figure 3.9B). The fibers purified by method 3 appear split and damaged without any apparent silk sericin contamination (Figure 3.9C).

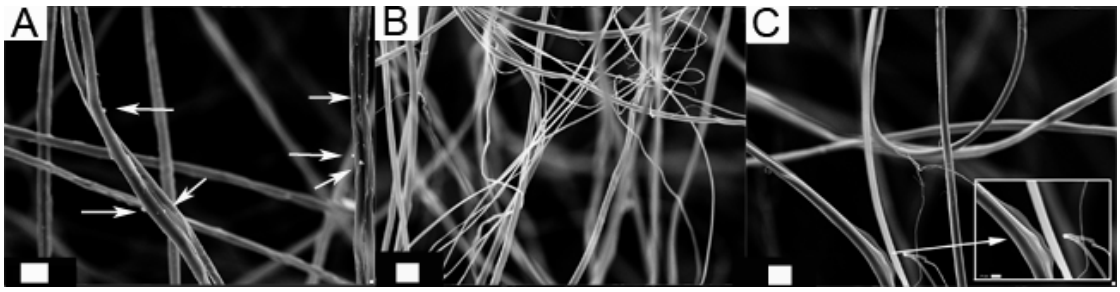

Figure 3.9 Representative SEM micrographs of silk fibers. (A) Silk fibers purified with water (method 1) contaminated by silk sericin as indicated by white arrows, (B) silk purified with Marseilles soap (method 2), (C) silk fibers purified with 0.02 M Na_2CO_3 appear damaged (inset: magnification of damaged fiber) (method 3). Scale bars in A, B, C: 30 μm, and inset: 10 μm.

SDS-PAGE gel electrophoresis was used to characterize the molecular weight of the silk fibroin proteins after purification (Figure 3.10). In agreement with previous studies on silk fibroin purified from cocoons, broad protein bands were observed for proteins from all purification methods.[35, 39, 54] These broad bands correspond to mixtures of polypeptides with wide distributions of molecular weights. Figure 3.10 shows that all protein fragments from method 3 have molecular weights below 350 kDa (the molecular weight of the heavy native protein chain), while the largest

fragments from methods 1 and 2 are approximately 350 kDa. The lower molecular weights (<350 kDa) observed for Method 3, as compared to the other two methods, suggests that the high pH (pH 10.5) of the sodium carbonate solution (method 3) coupled with the refluxing solution, leads to more hydrolysis of the silk fibroin chains than the other methods with lower pH values.[39] Interestingly, literature values from light scattering techniques give molecular weights for silk fibroin that vary by orders of magnitude ($3.7 \times 10^5 - 1.6 \times 10^7$ Da).[45, 55-57] This variability could be the result of the purification methods used in the different studies.

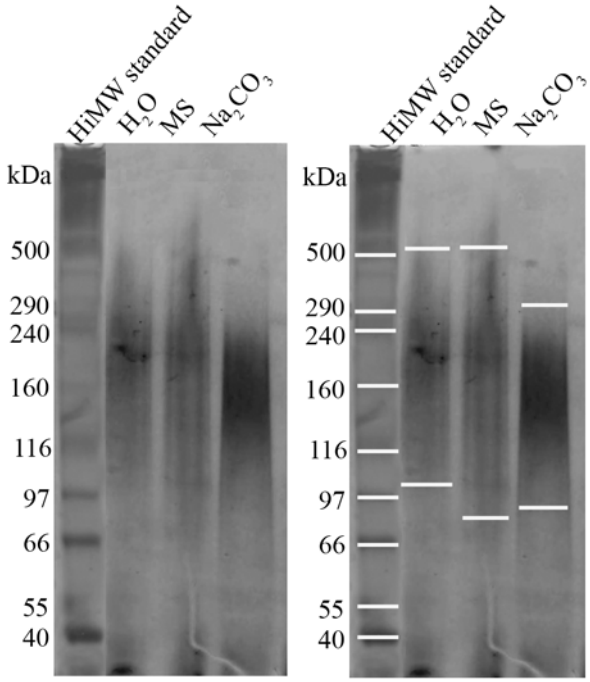

Figure 3.10 Representative SDS-PAGE analysis of reduced samples, stained with silver. Labeled version on the right with white lines indicating molecular weight distribution range of silk fibroin. Key: H_2O (method 1), MS = Marseilles soap purified silk (method 2), and Na_2CO_3 (method 3).

My static light scattering (SLS) data agrees with reported variability as well as with the SDS-PAGE data. Method 3 has the lowest molecular weight and method 1 the largest (Figure 3.11). For more details regarding experimental molecular weight calculations, based on SLS measurements, refer to the Materials and Methods section (3.5.9). The molecular weight calculations produced large standard deviations among samples. The error is most likely from variations in the molecular weights within a single solution (also seen by SDS-PAGE gels) as well as possible protein aggregation during the time scale of the measurements.

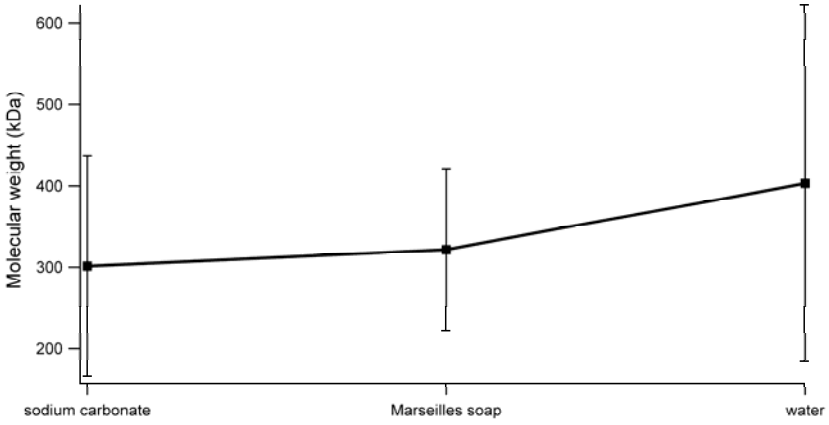

Figure 3.11 Calculated molecular weights of the three silk purification methods by static light scattering measurements.

Differences in the molecular weights of polymer chains can lead to different degrees of entanglement of the chains [49, 51] and may explain the observed differences in the kinetics of gelation and yield stresses among the three samples. The kinetics of β-sheet and gel formation correlate directly with the observed trends in molecular weight of the fibroin chains. Methods 1 and 2 produce silk fibroin with the largest observed average molecular weight (Figure 3.10 and 3.11). Long chains readily entangle, which can explain the observed rapid gelation of W-gel, as compared to the

other purification methods (Table 3.1). Method 3 has the lowest observed molecular weight and the SC-gel forms the slowest. The observed shear stresses and the zero-shear viscosities also correlate with the observed molecular weight distributions of the polymer chains in the three fibroin samples. The molecular weight distributions of the W- and MS-gels are similar to each other (and higher than the SC-gel), as are the zero-shear viscosities and the yield stresses. The SC-gel has the lowest average molecular weight (from SDS-PAGE and SLS, Figure 3.10 and 3.11) and the lowest inferred yield stress (Figure 3.7), of the three samples.

3.4 Conclusion

There is a tradeoff between effective sericin removal (required for biocompatibility of the resulting hydrogels) and minimal hydrolysis of the fibroin peptide chains during the purification of silk fibroin from silkworm cocoons. Depending on the tolerance for silk sericin in the final application, gels with different properties can be obtained. Boiling water alone (method 1) is insufficient to remove sericin from the silk fibers. The two alkaline degumming solutions are equally effective at removing sericin (~100% removed), despite the difference in pH (method 2, pH 8.25 versus method 3, pH 10.50). The lower pH of the soap solution (method 2) is either sufficiently alkaline to solubilize the sericin, and/or the presence of the surfactant assists in dissolving the sericin. While silk sericin contamination may partially contribute to the observed differences in rheology and gelation kinetics, MS- and SC- gels have equal amounts of silk sericin contamination (within error) and yet have drastically different properties. MS- and SC-purified silk fibroin also differs in both the highest molecular weight and the range of molecular weights of the peptide chains. Longer polymer chains should lead to faster gelation times and larger yield stresses due to the higher degree of chain entanglement and cross-linking.[14, 23]

Consistent with this prediction, the MS- and W-gels form faster and have higher yield stresses when compared with the SC-gel.

Chapters 4 and 5 use silk fibroin that has been purified with a combination of Marseilles soap and sodium carbonate. Marseilles soap is used for the majority of the purification time due to the gentle purification method, while sodium carbonate is used for a short time (30 minutes) at the end to ensure optimal sericin removal. The combination method produces gels with properties similar to those purified with Marseilles soap alone, but gels take longer to form. The slower β-sheet formation is advantageous because I then have more time flexibility to use the aqueous, random coil silk in experiments prior to gelation. This work suggests that for applications involving silk fibroin hydrogels, the choice of purification method is a key factor in determining the final properties of the gel.

3.5 Materials and Methods

3.5.1 Purification

Bombyx mori cocoons were cut into approximately 1.5 cm pieces and any insect remnants were manually removed. The cocoon material (0.5 g) was boiled in 500 mL of one of the following solutions: 1) deionized water[28] (18.2 MΩ, Barnstead EASYpure RoDI), 2) 5 w/v % Marseilles soap solution (an olive oil based soap from Marseilles, France),[9] or 3) 0.02 M sodium carbonate [11] (Na_2CO_3, J.T. Baker) for 2 hours, changing the solution every 15 minutes to solubilize and remove the silk sericin. After boiling, the silk was rinsed with copious amounts of water to remove excess salts or surfactants. The resulting silk mass was dissolved overnight, at room temperature, in 9.3 M lithium bromide (LiBr, Reagent Plus ≥99%, Sigma-Aldrich). The concentration of the resulting silk solution was approximately 25 wt%. The

solubilized silk was then filtered (Whatman filter paper) and dialyzed (Slide-a-Lyzer dialysis cassettes, Pierce, MWCO 3,500). Silk solutions (30 mL) were dialyzed against DI water (3 L) for three days at room temperature, changing the water twice daily. The resulting silk solutions are approximately 5 wt%, which was determined by weighing the remaining solid after air drying.

3.5.2 Degumming mass loss

Air dried silk fibers were massed before and after degumming (as described above before dissolution in 9.3 M LiBr). After degumming, the solution containing the fibers was centrifuged. The fibers were removed from the supernatant, copiously rinsed with DI water and air dried. Mass loss values are based on the average of 3 trials.

3.5.3 Direct Red 80 staining

Dry, degummed silk fibers were stained in a 1 wt% aqueous solution of Direct Red 80 (DR 80, Fluka) at 100º C for 1 minute.[52] Fibers were then copiously rinsed with DI water to remove all excess stain. Stained fibers were dissolved in 9.3M LiBr to give a 5 wt% solution of the dyed silk, and then centrifuged at 500 g for 10 minutes to remove any undissolved fibers. Solutions were then analyzed in a UV transparent 96 well plate (Costar) with a Spectramax Plus 384 Spectrophotometer at room temperature. A calibration curve of various concentrations of DR 80 (9 μM - 0.5 mM) in 9.3 M LiBr was constructed to determine the molar absorptivity of DR 80 in 9.3 M LiBr at 490 nm using the Beer's Law (Equation 3.2).

$$A = \varepsilon l c \qquad [3.2]$$

Concentration values based on the average of 2-3 trials.

3.5.4 Gelation

Fresh aqueous silk solutions (3 mL), in capped glass test tubes, were either incubated in a hot water bath at 60º C or kept at room temperature to gel. A sample

was considered a gel when the vial was inverted and the solution did not fall after 30 seconds.[11] A water purified silk hydrogel will be referred to as a W-gel, a Marseilles soap purified hydrogel as a MS-gel, and a Na_2CO_3 purified hydrogel as a SC-gel.

3.5.5 Circular Dichroism (CD)

Spectra were recorded using a Model 400 Aviv spectrometer with a Peltier thermocouple temperature control. The spectra were recorded from 190 to 250 nm with a 1 nm step for all wavelength experiments. Kinetic experiments recorded theta values at 217 nm over time. For both wavelength and kinetic experiments, samples were held at 60º C and spectra were recorded every hour for 24 to 48 hours. Rates, from kinetic experiments, were determined by averaging slope coefficients from 2 to 3 trials. Fresh silk solutions or gels were used for all experiments. A quartz cuvette (Helma Worldwide) with a 1 cm path length was used for measurements, and was capped to prevent evaporation. Silk samples were diluted with DI water to a concentration of ~20 μg/mL for the best signal to noise ratio. Background spectra (DI water) were recorded and subtracted from each sample. Background subtracting and spectra smoothing were all done within the CD software. All theta values are reported as millidegree per milligram (mdeg/mg).

3.5.6 X-Ray Diffraction

The measurements were performed using a Scintag Theta-Theta Diffractometer with CuKα radiation at 45 kV and 40 mA. Freeze dried silk fibroin hydrogels were placed on the no background beryllium sample holder. Each sample was scanned over a 2θ range of 5-40º with a step size of 0.02º and a scan rate of 2.40 degrees/minute.

3.5.7 Rheology

Rheological measurements were obtained on a Paar Physica Modular Compact Rheometer (MCR 300). A cone and plate measurement system was employed with a

25 mm diameter and 4.5º cone angle. Rheological measurements were conducted on samples with protein concentrations of ~5 wt%. To ensure complete β-sheet transformation, all gel samples were aged for 7 days at 60° C before rheological testing.[17] Samples were allowed to equilibrate to room temperature for 1 hour prior to loading into the rheometer. All samples (0.4 mL) were slowly added to the rheometer plate, using a syringe, to prevent the buildup of bubbles. A small amount of mineral oil was added to the rim of the cone-and-plate setup to slow the evaporation of water. Frequency sweep experiments were performed within the linear viscoelastic region. All flow curves were taken using creep experiments, where a constant stress is applied and the strain of the gel is measured as a function of time. Age of the hydrogel is not a determining factor; measurements were reproducible on the same gel sample after several days.

3.5.8 Scanning Electron Microscopy (SEM)

Degummed fibers were mounted on an SEM stub with double-sided carbon tape. To increase conductivity, the samples were sputtered with a thin layer of Au-Pd. The images were obtained using a Leica 440 SEM at 25kV.

3.5.9 Gel Electrophoresis

Samples were run on a 3-8% NuPAGE Novex Tris-Acetate Gel (Invitrogen) for molecular weights between 40-500 kDa. The solutions contained 6.5 μL fresh silk solution, 2.5 μL NuPAGE sample buffer (Invitrogen), and 1 μL NuPAGE Reducing Agent (Invitrogen). The solutions were mixed and then loaded into the gel. The gel ran at 150V for 1.25 hours. HiMark Pre-Stained High Molecular Weight Protein Standard (Invitrogen) was used. Gels were stained with a silver stain kit (SilverQuest Silver Stain, Invitrogen) and then scanned (Canon CanoScan 4200 F) to record.

3.5.10 Static Light Scattering

Static light scattering measurements were performed at room temperature in a Malvern Zetasizer NanoZS equipped with a 4 mW HeNe laser light source at a wavelength of 633 nm. Measurements were made on silk solutions of varying concentrations (5 mg/mL to 0.05 mg/mL) by diluting the initial stock solution with DI water. All experiments were input from lowest concentration to highest to ensure large aggregates from more concentrated samples would not contaminate weaker dilutions. Background standards (toluene and DI water) were first referenced for initial background scattering. Molecular weight (M_w) and the 2nd Virial Cofficient (A_2) were determined by applying the Rayleigh equation (Equation 3.3) at different sample concentrations.

$$\frac{KC}{R_\theta} = \left(\frac{1}{M_W} + 2A_2C \right) P(\theta) \qquad [3.3]$$

The intensity of scattered light ($KC/R_\theta P(\theta)$) is measured by the instrument where R_θ is the ratio of the scattered light to the incident light of the sample (known as the Rayleigh ratio), K is an optical constant which is dependent on the wavelength of the light source as well as the refractive index as a function of concentration change, and $P(\theta)$ is the angular dependence of the sample scattering intensity.

Debye plots of the intensity of the scattered light ($KC/R_\theta P(\theta)$) versus sample concentration (C) were plotted. The intercept of the line extrapolated to zero concentration gives the reciprocal molecular weight ($1/ M_w$) and the gradient of the line gives the 2nd Virial Coefficient (A_2). A_2 is a property describing the interaction strength between particles and the solvent.

REFERENCES

1. Altman, G. H.; Diaz, F.; Jakuba, C.; Calabro, T.; Horan, R. L.; Chen, J. S.; Lu, H.; Richmond, J.; Kaplan, D. L., *Biomaterials* **2003,** 24, (3), 401-416.

2. Panilaitis, B.; Altman, G. H.; Chen, J. S.; Jin, H. J.; Karageorgiou, V.; Kaplan, D. L., *Biomaterials* **2003,** 24, (18), 3079-3085.

3. Moy, R. L.; Lee, A.; Zalka, A., *American Family Physician* **1991,** 44, (6), 2123-2128.

4. Li, C. M.; Vepari, C.; Jin, H. J.; Kim, H. J.; Kaplan, D. L., *Biomaterials* **2006,** 27, (16), 3115-3124.

5. Wang, Y. Z.; Blasioli, D. J.; Kim, H. J.; Kim, H. S.; Kaplan, D. L., *Biomaterials* **2006,** 27, (25), 4434-4442.

6. Addadi, L.; Joester, D.; Nudelman, F.; Weiner, S., *Chem. Eur. J.* **2006,** 12, (4), 981-987.

7. Falini, G.; Albeck, S.; Weiner, S.; Addadi, L., *Science* **1996,** 271, (5245), 67-69.

8. Levi, Y.; Albeck, S.; Brack, A.; Weiner, S.; Addadi, L., *Chem. Eur. J.* **1998,** 4, (3), 389-396.

9. Falini, G.; Weiner, S.; Addadi, L., *Calcif. Tissue Int.* **2003,** 72, (5), 548-554.

10. Collins, A. M.; Skaer, N. J. V.; Gheysens, T.; Knight, D.; Bertram, C.; Roach, H. I.; Oreffo, R. O. C.; Von-Aulock, S.; Baris, T.; Skinner, J.; Mann, S., *Adv. Mater.* **2009,** 21, (1), 75-78.

11. Kim, U. J.; Park, J. Y.; Li, C. M.; Jin, H. J.; Valluzzi, R.; Kaplan, D. L., *Biomacromolecules* **2004,** 5, (3), 786-792.

12. Magoshi, J.; Magoshi, Y.; Nakamura, S. In *Mechanism of Fiber Formation of Silkworm*, Silk Polymers, 1994; Kaplan, D. L., Ed. 1994; pp 292-310.

13. Rossle, M.; Panine, P.; Urban, V. S.; Riekel, C., *Biopolymers* **2004,** 74, (4), 316-327.

14. Rammensee, S.; Huemmerich, D.; Hermanson, K. D.; Scheibel, T.; Bausch, A. R., *Appl. Phys. A-Mater. Sci. Process.* **2006,** 82, (2), 261-264.

15. Gil, E. S.; Frankowski, D. J.; Bowman, M. K.; Gozen, A. O.; Hudson, S. M.; Spontak, R. J., *Biomacromolecules* **2006,** 7, (3), 728-735.

16. Ayub, Z. H.; Arai, M.; Hirabayashi, K., *Polymer* **1994,** 35, (10), 2197-2200.

17. Matsumoto, A.; Chen, J.; Collette, A. L.; Kim, U. J.; Altman, G. H.; Cebe, P.; Kaplan, D. L., *J. Phys. Chem. B* **2006,** 110, (43), 21630-21638.

18. Hanawa, T.; Watanabe, A.; Tsuchiya, T.; Ikoma, R.; Hidaka, M.; Sugihara, M., *Chem. Pharm. Bull.* **1995,** 43, (2), 284-288.

19. Jin, H. J.; Kaplan, D. L., *Nature* **2003,** 424, (6952), 1057-1061.

20. Zuo, B.; Dai, L.; Wu, Z., *J. Mater. Sci.* **2006,** 41, (11), 3357-3361.

21. Junghans, F.; Morawietz, M.; Conrad, U.; Scheibel, T.; Heilmann, A.; Spohn, U., *Appl. Phys. A-Mater. Sci. Process.* **2006,** 82, (2), 253-260.

22. Holland, C.; Terry, A. E.; Porter, D.; Vollrath, F., *Nat. Mater.* **2006,** 5, (11), 870-874.

23. Terry, A. E.; Knight, D. P.; Porter, D.; Vollrath, F., *Biomacromolecules* **2004,** 5, (3), 768-772.

24. Jiang, P.; Liu, H.; Wang, C.; Wu, L.; Huang, J.; Guo, C., *Mater. Lett.* **2006,** 60, 919-925.

25. Lotz, B.; Cesari, F. C., *Biochimie* **1979,** 61, (2), 205-214.

26. Asakura, T.; Kuzuhara, A.; Tabeta, R.; Saito, H., *Macromolecules* **1985,** 18, (10), 1841-1845.

27. Ha, S. W.; Tonelli, A. E.; Hudson, S. M., *Biomacromolecules* **2005,** 6, (3), 1722-1731.

28. Muller, W. S.; Samuelson, L. A.; Fossey, S. A.; Kaplan, D. L., *Langmuir* **1993,** 9, (7), 1857-1861.

29. Valluzzi, R.; Gido, S. P.; Zhang, W. P.; Muller, W. S.; Kaplan, D. L., *Macromolecules* **1996,** 29, (27), 8606-8614.

30. Asakura, T.; Yamane, T.; Nakazawa, Y.; Kameda, T.; Ando, K., *Biopolymers* **2001,** 58, (5), 521-525.

31. Kenney, J. M.; Knight, D.; Wise, M. J.; Vollrath, F., *Eur. J. Biochem.* **2002,** 269, (16), 4159-4163.

32. Dicko, C.; Knight, D.; Kenney, J. M.; Vollrath, F., *Biomacromolecules* **2004,** 5, (3), 758-767.

33. Dicko, C.; Knight, D.; Kenney, J. M.; Vollrath, F., *Biomacromolecules* **2004,** 5, (6), 2105-2115.

34. Li, G. Y.; Zhou, P.; Shao, Z. Z.; Xie, X.; Chen, X.; Wang, H. H.; Chunyu, L. J.; Yu, T. Y., *Eur. J. Biochem.* **2001,** 268, (24), 6600-6606.

35. Tsuboi, Y.; Ikejiri, T.; Shiga, S.; Yamada, K.; Itaya, A., *Appl. Phys. A-Mater. Sci. Process.* **2001,** 73, (5), 637-640.

36. Lee, K. H., *Macromol. Rapid Commun.* **2004,** 25, (20), 1792-1796.

37. Ki, C. S.; Kim, J. W.; Oh, H. J.; Lee, K. H.; Park, Y. H., *Int. J. Biol. Macromol.* **2007,** 41, (3), 346-353.

38. Freddi, G.; Mossotti, R.; Innocenti, R., *J. Biotechnol.* **2003,** 106, 101-112.

39. Yamada, H.; Nakao, H.; Takasu, Y.; Tsubouchi, K., *Materials Science and Engineering C* **2001,** 14, 41-46.

40. *Chemical testing of Textiles*. CRC Press LLC: Boca Raton, 2005; p 325.

41. Phillips, D. M.; Drummy, L. F.; Conrady, D. G.; Fox, D. M.; Naik, R. R.; Stone, M. O.; Trulove, P. C.; De Long, H. C.; Mantz, R. A., *J. Am. Chem. Soc.* **2004,** 126, (44), 14350-14351.

42. Chen, X.; Knight, D. P.; Shao, Z. Z.; Vollrath, F., *Polymer* **2001,** 42, (25), 9969-9974.

43. Fasman, G. D., *Circular Dichroism and the Conformational Analysis of Biomolecules*. Plenum Press: New York, 1996.

44. As the silk converts from a random coil to a b-sheet, the value of 217 nm becomes less negative. For convenience, the absolute value of 217 nm CD signal is plotted in Figure 1b.

45. Hossain, K. S.; Ohyama, E.; Ochi, A.; Magoshi, J.; Nemoto, N., *J. Phys. Chem. B* **2003,** 107, (32), 8066-8073.

46. Wang, H.; Zhang, Y. P.; Shao, H. L.; Hu, X. C., *Int. J. Biol. Macromol.* **2005,** 36, (1-2), 66-70.

47. Ayub, Z. H.; Arai, M.; Hirabayashi, K., *Bioscience Biotechnology and Biochemistry* **1993,** 57, (11), 1910-1912.

48. Kang, G. D.; Nahm, J. H.; Park, J. S.; Moon, J. Y.; Cho, C. S.; Yeo, J. H., *Macromol. Rapid Commun.* **2000,** 21, (11), 788-791.

49. Ferry, J. D., *Viscoelastic Properties of Polymers*. John Wiley & Sons, Inc.: NY, 1980.

50. Li, H.; Yu, G. E.; Price, C.; Booth, C., *Macromolecules* **1997,** 30, 1347-1354.

51. Kavanagh, G. M.; Ross-Murphy, S. B., *Progress in Polymer Science* **1998,** 23, (3), 533-562.

52. Mahall, K.; Goebel, I., *Textilveredlung* **1988,** 23, 8-16.

53. Knott, J.; Freddi, G.; Belly, M., *Melliand Textilberichte* **1983,** 63, 481-483.

54. Horan, R. L.; Antle, K.; Collette, A. L.; Huang, Y. Z.; Huang, J.; Moreau, J. E.; Volloch, V.; Kaplan, D. L.; Altman, G. H., *Biomaterials* **2005,** 26, (17), 3385-3393.

55. Hyde, A. J.; Wippler, C., *Journal of Polymer Science* **1962,** 58, (166), 1083-&.

56. Hossain, K. S.; Nemoto, N.; Magoshi, J., *Langmuir* **1999,** 15, (12), 4114-4119.

57. Iizuka, E., *Rep. Prog. Polym. Phys. Jpn.* **1963,** 6, 343.

CHAPTER 4

INVESTIGATION OF ORGANIC MATRIX INTERFACES OF NACRE: SILK FIBROIN ADSORPTION AND CALCIUM CARBONATE MINERALIZATION ON FUNCTIONALIZED SURFACES[*]

4.1 Abstract

Assemblies of organic matrices, and the interface between the various components, are essential to many biological processes. This study describes an *in vitro* model for the organic matrix of nacre by investigating organic-organic (silk – chitin) and organic-inorganic (silk – chitin – mineral) interfaces. Self-assembled monolayers (SAMs) of alkanethiols on gold were used as substrates for calcium carbonate mineralization to model the chitin-protein interface. In the presence of silk, there was a loss of calcite orientation as well as a change in crystal nucleation density as compared to control surfaces, as characterized by x-ray diffraction and SEM analysis. To further understand the *in vitro* mineralization results, as well as gain insight into the structure of the *in vivo* organic matrix in nacre, I carried out protein adsorption studies of silk fibroin (aqueous and hydrogel) and BSA (control) on SAMs. The roles of protein starting conformation (random coil, β-sheet, and α-helix, as confirmed by CD spectroscopy and FTIR), protein state (aqueous versus hydrogel), and surface functionality (methyl-, carboxylate-, ethylene glycol-terminated SAMs, and bare gold) were examined. Grazing angle Fourier transform spectroscopy (GAFTIR) was used to verify surface functionality, determine protein secondary structure on the surface, and determine relative amounts of protein adsorbed on the surfaces by monitoring both amide I (1600-1700 cm^{-1}) and amide II (1500-1600 cm^{-1})

[*] E. C. Keene, A. M. Richter, V. Ravichandran, and L. A. Estroff, in preparation.

peak positions. The random coil, aqueous silk fibroin adsorbed the most to all surfaces, while the β-sheet silk fibroin hydrogel adsorbed the least. Across surfaces, the bare gold (unfunctionalized) substrate adsorbed the most protein. These results demonstrate the importance of surface chemistry and protein starting conformation on protein adsorption.

4.2 Introduction

Understanding the role of the organic-inorganic and organic-organic interfaces within biological systems (such as nacre) has implications for synthesis of new materials based upon the interactions among functionalized surfaces, biomacromolecules, and mineral. Here I present a synthetic system to probe the organic-organic matrix interface, between functionalized gold surfaces and the protein silk fibroin, and the organic-inorganic interface between protein/surfaces and mineral, and their implications for nacre formation (Figure 4.1).

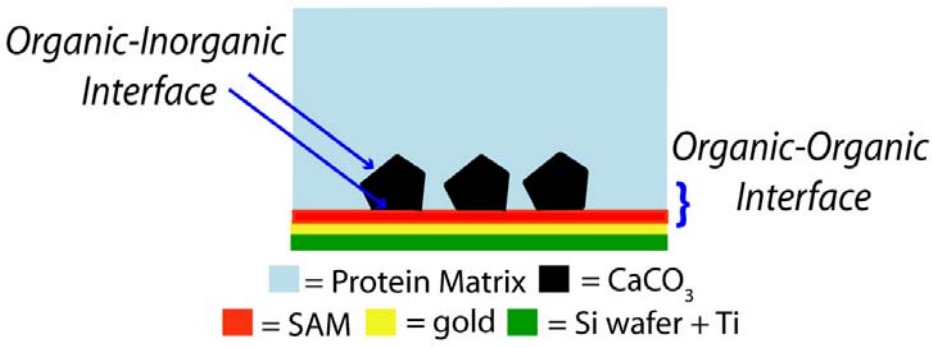

Figure 4.1 Schematic of experimental design. The interface between the SAM and the protein is referred to as the organic-organic interface. The growth interface (mineral-protein) and the nucleating interface (mineral-SAM) are both referred to as the organic-inorganic interface.

Histochemical studies of decalcified nacre have shown that carboxylate and sulfate groups are localized on an organic substrate (interlamellar chitin sheets between nacre tablets) to form possible nucleation sites for $CaCO_3$.[1, 2] Chapter 2 demonstrated a nacre specific peptide, n16N, specifically binds to β-chitin.[3] This interaction creates a new organic matrix interface (chitin + bound peptide together are a new organic substrate for crystal nucleation) that selectively nucleates aragonite over calcite. While the structure/orientation of the peptide on the chitin substrate is unknown, Chapter 2 suggests that the interface between the insoluble organic matrix (β-chitin) with the other organic matrix components is a complex molecular interface worthy of further study.[3, 4]

A recent study by Weiss et al. looked at the relationship between chitin and proteins in the insoluble shell organic matrices of the bivalve *Mytilus galloprovincialis* of both adult and larval mollusk development.[5] Based on data from mass spectroscopy they proposed that there is an "intimate link" between the two separate phases (β-chitin and silk-like proteins). The data demonstrated a significant change in the surface activity of the chitin-protein complex as compared to pure chitin. They also suggested the chitin-silk complex is crucial for mollusk shell biomineralization, as the complex is present in both adult and larval development stages. Therefore, based upon these studies, further investigation of silk at interfaces, analogous to the β-chitin – silk-like protein in nacre, is necessary. In this study, I focus on protein-surface interactions (i.e., protein conformation and amount adsorbed) of silk fibroin, and the effects the adsorbed protein have on calcium carbonate mineralization.

Self assembled monolayers (SAMs), of ω-functionalized alkanethiols on metals (typically gold), have become a universal model surface to study the structures and properties of organic surfaces and their influence on protein adsorption[12] as well as control over crystal growth.[6, 7] SAMs on gold are well-characterized and form

stable organic layers on metal surfaces with various terminal functional groups.[8] Extensive work by Aizenberg and others, have shown that surface chemistry and orientation of the terminal functional group determines the crystallographic orientation of calcium carbonate crystals nucleated on SAMs.[7, 9-12] To further extend the SAM model to biomineralization, proteins can also be introduced into the SAM-mineralization assay. The chemical nature of the surface and its properties (charge, hydrophobicity, etc.) may affect protein adsorption,[13-21] as well as, the conformation of the adsorbed protein layer.[17, 19, 20, 22-24] Therefore, the presence of protein may affect the ability of the surface to template the nucleation of calcium carbonate crystals.

To characterize the protein-SAM system, I chose Fourier transform infrared spectroscopy (FTIR) as a widely available, well-established tool for the characterization of protein secondary structure [25] (including both silk fibroin[26-28] and BSA[17, 29, 30]). Grazing angle FTIR (GAFTIR) is a surface sensitive technique that can non-destructively look at monolayer functionalities on reflective surfaces (i.e., gold), such that after analysis, the surface can then be used for other experiments (i.e., crystal growth) unlike XPS or AFM. While many techniques have been utilized to measure protein adsorption on SAMs (FTIR,[17, 22, 26, 29-32] SPR,[14, 16, 18, 33] QCM,[17, 34] ellipsometry,[13, 14, 35] contact angle,[14, 32] AFM,[23, 36] and XPS[13, 16, 35]), only FTIR is sensitive to protein secondary structure. Sample characterization by FTIR is both a qualitative and quantitative technique. It can verify surface chemical functionalities (qualitative),[37-40] while based on peak positions it can determine protein secondary structure (qualitative)[25, 26] as well as relative amounts of protein adsorbed based on peak areas (semi-quantitative).[41]

4.3 Results and Discussion

4.3.1 Crystallization of calcium carbonate on Self Assembled Monolayers with silk fibroin

I examined $CaCO_3$ growth on 4 surfaces (bare gold, methyl,[37] carboxylic acid,[38] and ethylene glycol[39, 40] terminated SAM functionalities) in the presence and absence of silk fibroin gels (Figure 4.2). Calcite orientation and nucleation density on SAMs were determined. For further tangential crystallization experiments with silk fibroin, see Appendix 3.

4.3.1.1 Crystal Orientation

In agreement with literature,[7, 42, 43] calcite crystals grown on a carboxylic acid terminated SAM are (012) oriented, as demonstrated by SEM and x-ray diffraction results (Figure 4.2A and C). Calcite grown on bare gold, methyl, and PEG-terminated SAMs, however, are randomly oriented (Figure 4.3). Initial attempts to combine silk fibroin and carboxylate SAMs, to model nacre formation, resulted in a loss of crystal orientation and a change in crystal morphology (Figure 4.4). Previous results have shown that carboxylate-terminated SAMs retain their control over orientation in the presence of an agarose hydrogel.[44] The loss of calcite orientation on this SAM, when combined with silk, suggests the protein is binding to the surface and masking the carboxylate functionality or altering its configuration. Proteins may have a greater affinity for the SAMs than the polysaccharide agarose hydrogel.

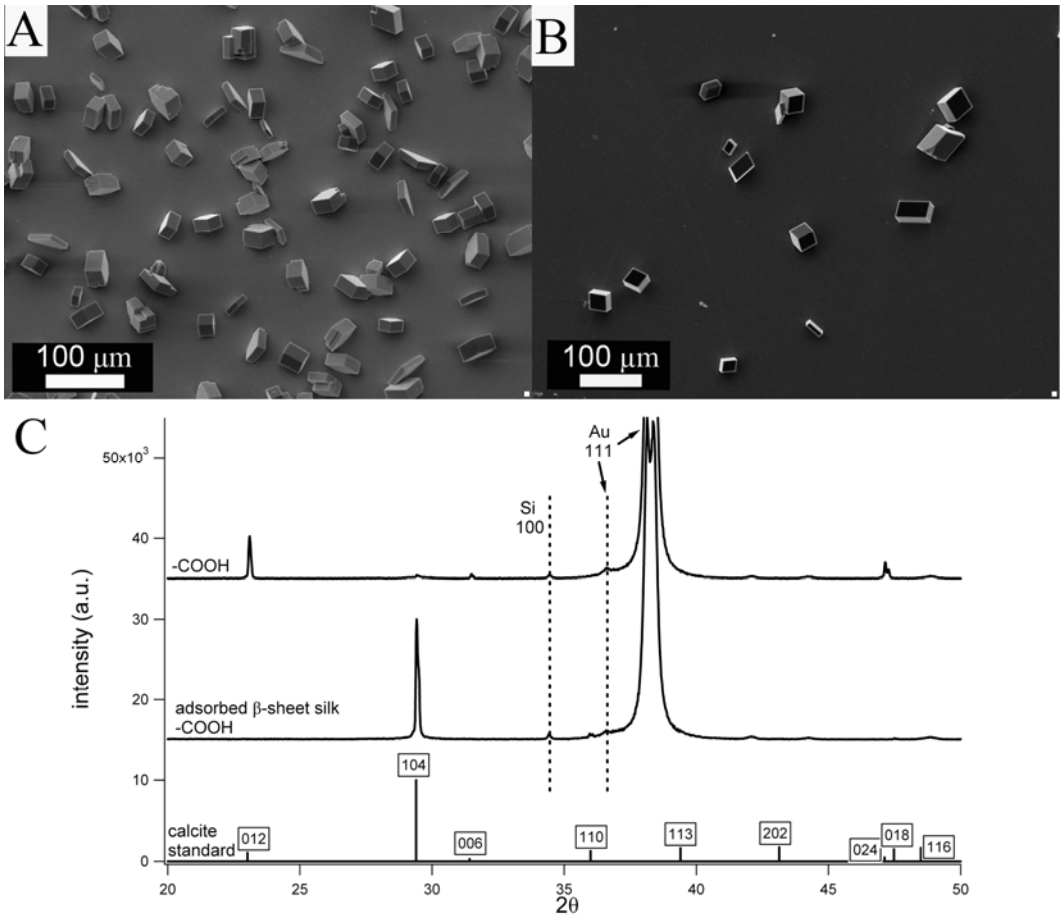

Figure 4.2 Calcite crystallization studies on SAMs. (A) Control crystallization on -COOH (B) Crystallization on –COOH after β-sheet silk adsorption (C) XRD spectra of calcite crystal orientations. Control calcite (top spectra) grown on SAMs show preferred (012) orientation, while calcite grown on SAMs with adsorbed silk (middle) are randomly oriented.

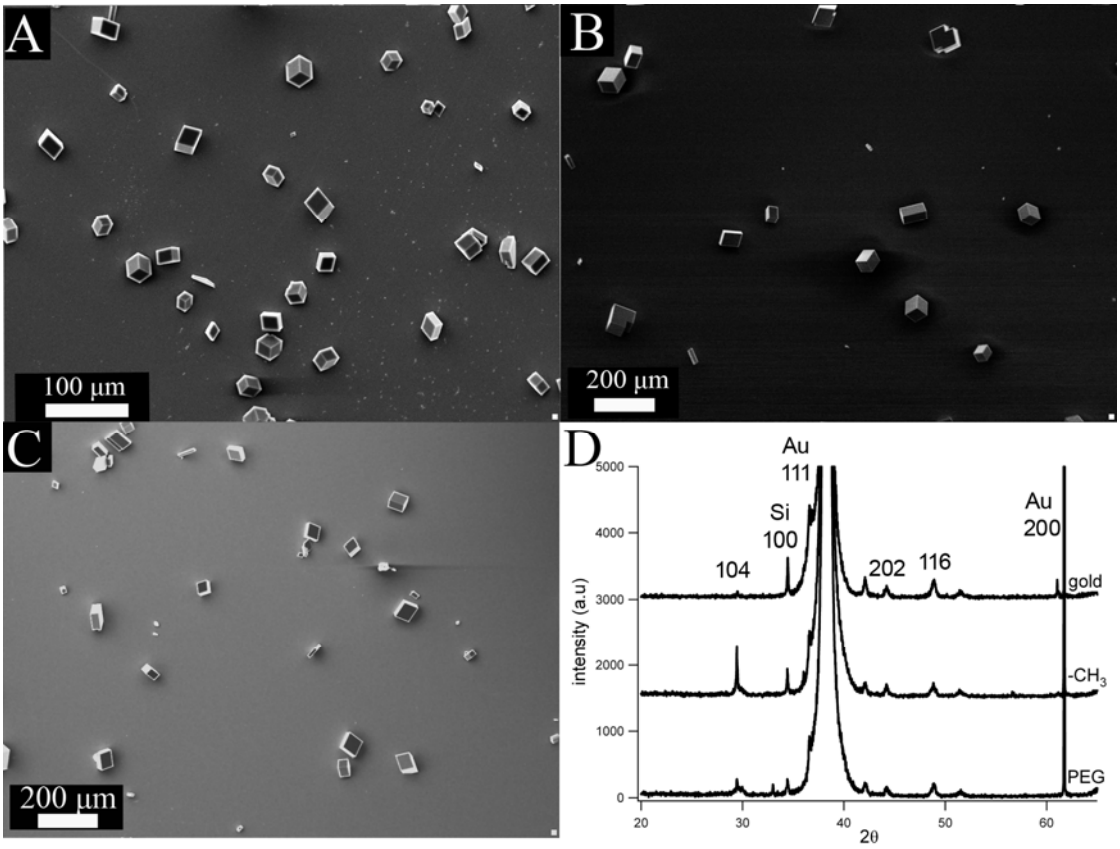

Figure 4.3 SEM micrographs of calcite on (A) bare gold, (B) methyl-, and (C) PEG terminated SAMs. (D) XRD plot of randomly oriented calcite. All labels on graph are calcite reflections, unless otherwise noted.

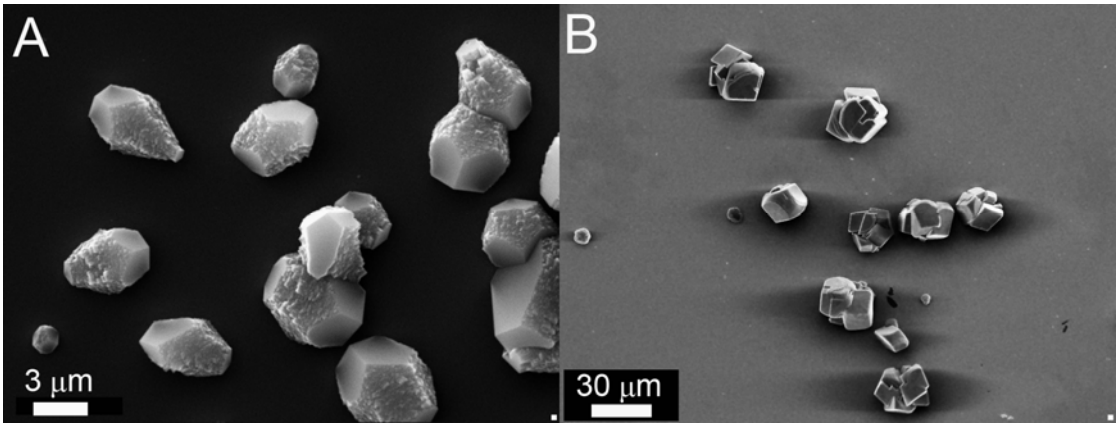

Figure 4.4 Calcite crystallization on carboxylate-terminated SAMs with 2.5 wt% silk fibroin (A) aqueous random coil (crystals are elongated along the *c*-axis) and (B) β-sheet hydrogel (poly-crystalline).

To investigate the nature of the protein-SAM interaction, SAMs were incubated with β-sheet silk (hydrogel), rinsed and used for crystallization (without the addition of other additives). These surfaces also lead to randomly oriented crystals (Figure 4.2B and C). Similar effects on crystallization are seen with surfaces that have been exposed to random coil, aqueous silk fibroin, as well as α-helical BSA (Figure 4.5).

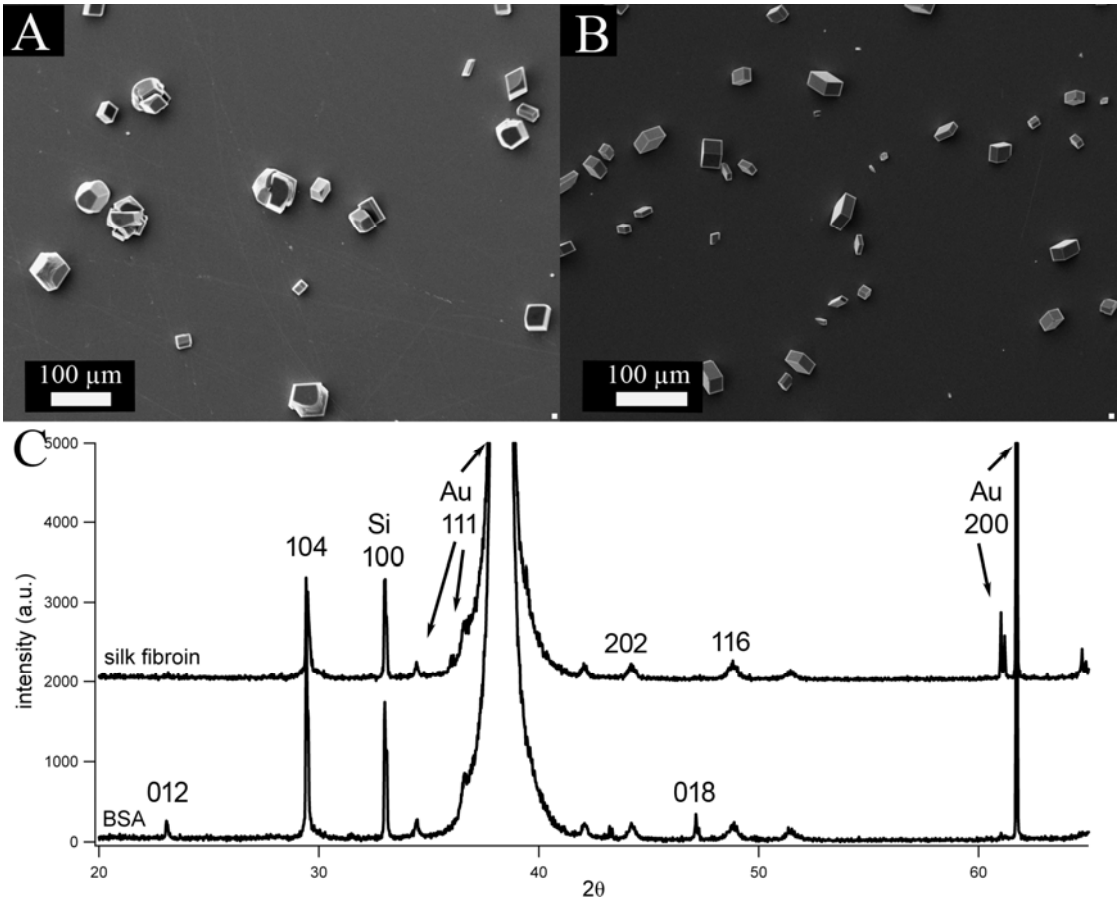

Figure 4.5 SEM micrographs of –COOH SAMs with adsorbed (A) random coil silk fibroin and (B) α-helix BSA. (C) XRD plot of randomly oriented calcite. All labels on graph are calcite reflections, unless otherwise indicated.

4.3.1.2 Nucleation Density

The presence of silk during crystallization also affects the nucleation density of calcite on SAMs. Methyl and carboxylate SAMs were compared for nucleation density studies (Table 4.1, Figure 4.6). In agreement with previous crystallization results,[7] control crystallization (without protein) on carboxylate SAMs promotes nucleation of calcite, while methyl SAMs inhibits nucleation. However, with the addition of silk (either random coil or β-sheet conformation) to the crystallization assay, the nucleation density on methyl SAMs surpasses the carboxylate surface suggesting a change in the organic-inorganic interface (i.e., silk adsorption may present advantageous functional groups for interaction with crystal nuclei).

Table 4.1 Crystal nucleation density on methyl and carboxylate SAMs

SAM Functionality	**Protein present?**	**Protein conformation**	**Nucleation density (crystals/mm^2)[a]**	**Area fraction (%)[a,b]**
-CH_3	No	---	143 ± 72	3 ± 2
	Yes	Random coil	4291 ± 1568	23 ± 6
	Yes	β-sheet	138 ± 48	10 ± 1
-COOH	No	---	1923 ± 192	16 ± 7
	Yes	Random coil	2556 ± 2475	16 ± 5
	Yes	β-sheet	105 ± 21	6 ± 1

[a]± standard deviation over a minimum of six images across three samples

[b]Area fraction accounts for total area covered by crystals (i.e., crystal sizes) over the entire sample area.

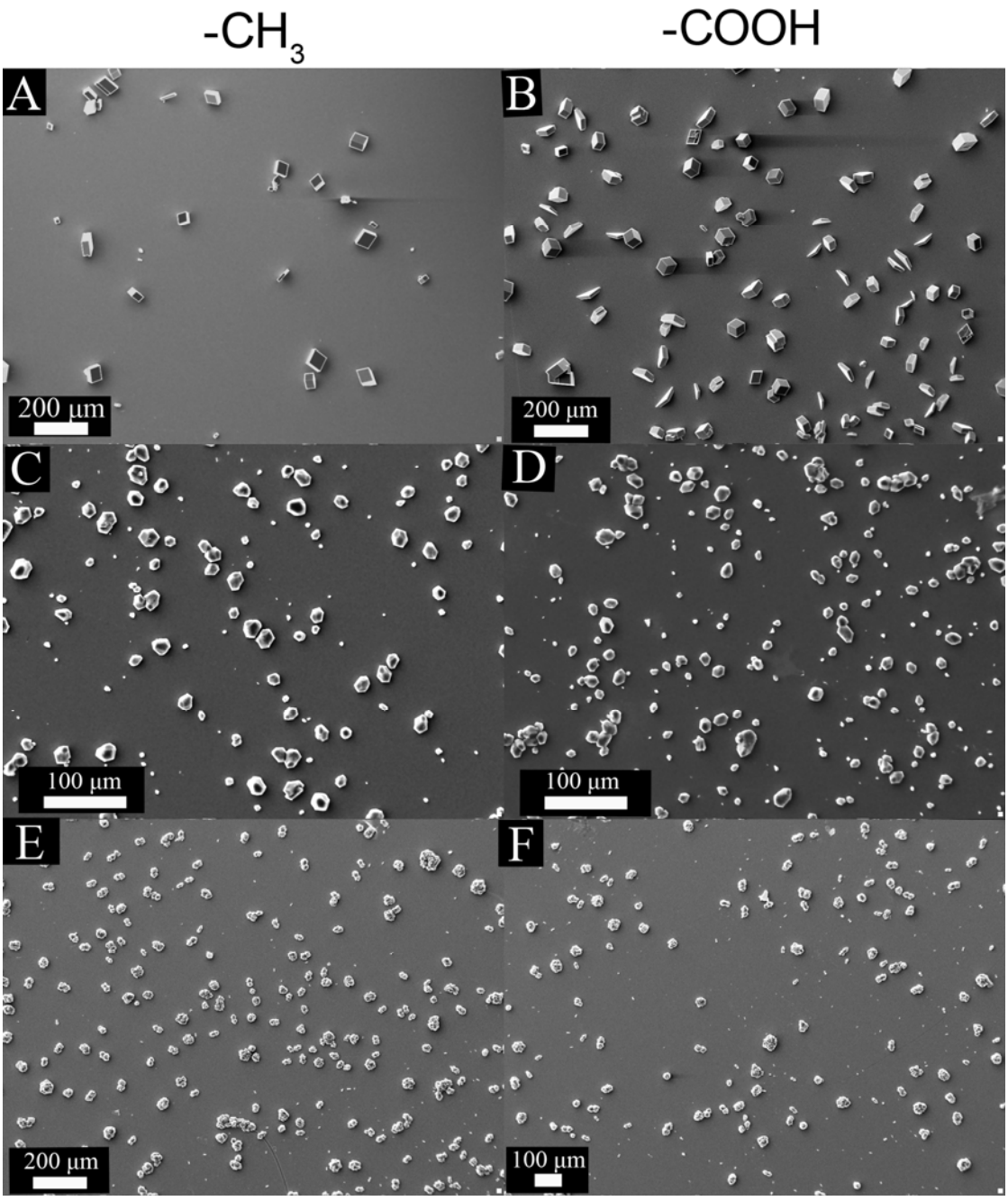

Figure 4.6 Low magnification images of calcite nucleation density studies. (A, C, E) are methyl –terminated SAMs and (B, D, F) are carboxylate-terminated SAMs. (A & B) are controls with no protein additives, (C & D) are with random coil silk fibroin, and (E & F) are with β-sheet silk fibroin.

In nacre, despite the periodic layering of chitin and silk-like proteins within nacre, how the interface is defined between the two different layers is unknown. Early XRD studies by Weiner and Traub proposed that the silk has a β-sheet conformation.[45] More recently, environmental SEM and cryo-TEM studies of nacre have suggested that the silk-like protein is a hydrogel.[46, 47] To provide insight into the nacre organic interface *in vitro*, as well as to explain the loss of crystal orientation on the carboxylate SAM, and change in crystal nucleation density with the addition of protein, protein adsorption on various SAMs was further characterized.

4.3.2 Protein-SAM characterization

I examined three different starting protein conformations (random coil and β-sheet silk fibroin; α-helix bovine serum albumin (BSA)). BSA is a commonly used control protein for many adsorption assays, as it is the "standard" for non-specific protein adsorption on both hydrophobic and hydrophilic surfaces.[48, 49] The random coil silk was an aqueous solution, whereas the β-sheet silk forms a hydrogel.[50, 51] Proteins were adsorbed onto SAMs (methyl,[37] carboxylic acid,[38] and ethylene glycol[39, 40] functionalities) and bare gold surfaces (see experimental section for further details). Before protein adsorption, the SAM functionalities were confirmed by GAFTIR (Figure 4.7). Each SAM was then incubated with protein and subsequently characterized by GAFTIR to quantify protein adsorption on the SAMs, as well as, any change in protein conformation due to surface adsorption.

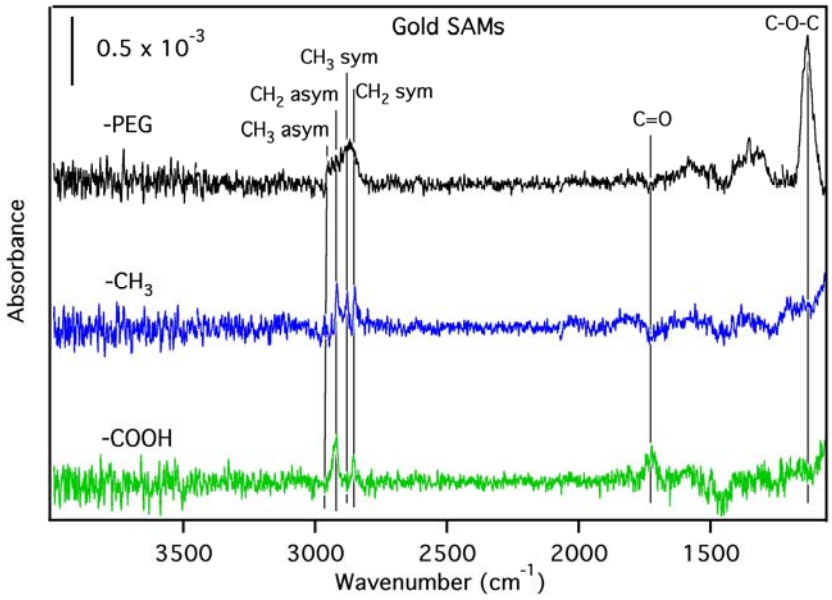

Figure 4.7 GAFTIR spectra of self assembled monolayers on gold (-CH_3, -COOH, -PEG) before protein adsorption. Expected chemistries for each surface are observed and consistent with literature spectra.[37-40]

4.3.2.1 Bulk protein conformation

The secondary structure of all three proteins was confirmed prior to protein adsorption studies. The solutions and gels were analyzed by circular dichroism (CD) spectroscopy (Figure 4.8), and protein films (see experimental for film preparation details) were analyzed by FTIR (Table 4.2). In agreement with literature, both techniques confirmed aqueous silk fibroin as random coil, silk fibroin hydrogels as β-sheet, and aqueous BSA as primarily α-helical.

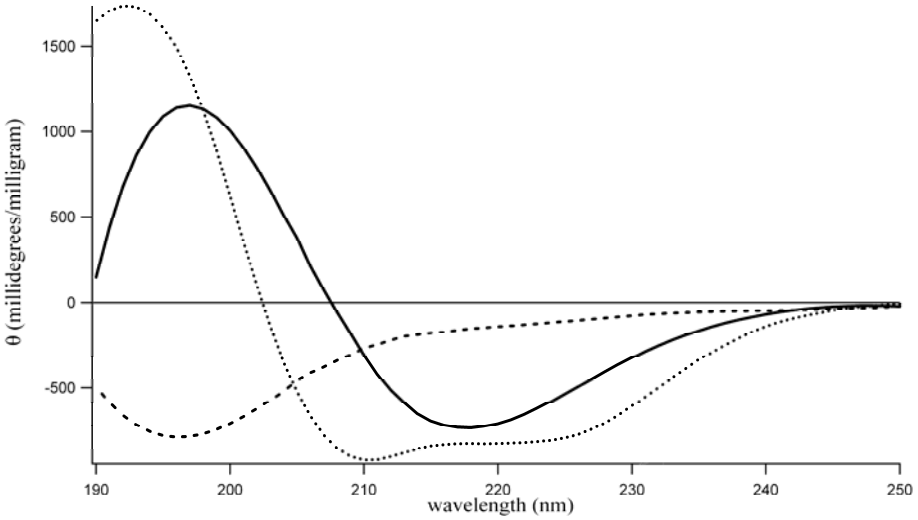

Figure 4.8 Representative CD spectra of aqueous silk fibroin (dashed line, random coil), gelled silk fibroin (solid line, β-sheet), and BSA (dotted line, α-helix) used for SAM incubation experiments. Spectra were taken of 20 μg/mL protein solutions.

Table 4.2 Amide IR peak positions (cm^{-1}) and area ratios of adsorbed proteins on functionalized gold surfaces

Random coil (silk)	**Amide I position (cm^{-1})[d]**	**Amide I area ratios[c]**	**Amide II position (cm^{-1})[d]**	**Amide II area ratios[c]**
Gold	1676 ± 0.7	1.00	1543 ± 2.3	1.00
-CH_3	1670 ± 1.3	0.85	1544 ± 1.1	0.96
-COOH	1673 ± 0.4	0.78	1544 ± 3.2	0.75
-PEG	-	-		-
Film[a]	1644		1520	
β-sheet (silk)				
Gold	1673 ± 2.1	0.17	1542 ± 1.7	0.32
-CH_3	1668 ± 2.3	0.21	1543 ± 0.8	0.38
-COOH	1667 ± 4.9	0.10	1542 ± 0.4	0.16
-PEG	-	-	-	-
Film[a]	1620		1520	
α-helix (BSA)				
Gold	1671 ± 0.6	0.41	1541 ± 1.7	0.47
-CH_3	1669 ± 1.0	0.20	1544 ± 0.6	0.33
-COOH	1670 ± 1.1	0.40	1543 ± 2.6	0.41
-PEG	-	-	-	-
Film[b]	1653		1538	

[a]Values from spectra taken using dried silk films on a diamond ATR

[b]Values for reference[29]

[c]Peak areas normalized to random coil silk - gold surface for each peak

[d]±standard deviation over a minimum of three measurements

4.3.2.2 Protein coverage

GAFTIR show that protein adsorbs on all SAMs except the PEG functionality, a known non-fouling surface (Figure 4.9).[35, 52] The underlying SAM functionality remains after incubation with all three proteins. From these results, the exact protein arrangement (i.e., packing density or orientation) on the surface is not known but relative amounts of protein adsorbed can be compared (semi-quantitatively) based on peak areas. Peak areas were analyzed to account for all protein conformations which may contribute to the amide I band (i.e., peak width and height).[41, 53] Since the amount of protein adsorbed on each surface could be related to the chemistry at the protein-SAM interface, peak areas for amide I and II were monitored for each protein conformation and surface chemistry. Amide peak areas are represented as ratios normalized to the random coil, aqueous silk fibroin on bare gold substrates for amide I and amide II, respectively (Table 4.2). Comparing amide I and II peak areas, bare gold and methyl-terminated SAMs adsorb the highest amount of silk fibroin (random coil or β-sheet), while the bare gold and carboxylate- terminated SAM adsorb the most BSA. Random coil, aqueous silk fibroin adsorbed the most of all three starting conformations for all surface chemistries, while the β-sheet silk hydrogel adsorbs the least.

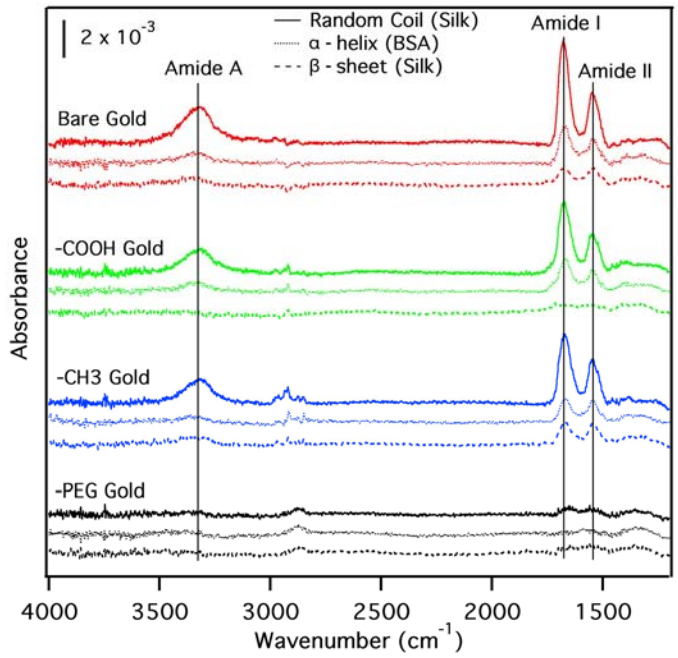

Figure 4.9 GAFTIR spectra of silk (random coil or β-sheet) and BSA (α-helix) proteins, represented by solid, dotted, and dashed lines respectively, adsorbed on functionalized gold surfaces.

The differences in protein adsorption, as a function of starting conformation, may be explained by looking at the inherent structure and stability of the protein. The random coil protein is a labile structure, and can quickly change its structure to effectively lower its surface energy at the protein-SAM interface. In contrast, the β-sheet structure is a folded, stable structure whose conformation is more difficult to change for interaction with a surface. Therefore, the fact that there is less β-sheet and α-helix protein adsorbing onto the various SAM surfaces correlates to the stability of the protein. Several studies within the literature have made similar correlations: less stable proteins attach to surfaces quicker and stronger (i.e., irreversible protein adsorption) than stable, folded structures.[21, 54, 55] Another possible difference between the adsorption amounts of the two silk proteins is the phase; the random coil

conformation (which adsorbs the most) is in solution while the β-sheet (which adsorbs the least) forms a hydrogel. As a hydrogel, the mobility of the proteins may be limited and would be less able to change their conformation to interact with the underlying substrate.

4.3.2.3 Protein conformation on SAMs

Protein-surface interactions play an important role in determining the conformation of the adsorbed proteins. The amide I region (1600-1700 cm^{-1}) is widely used for IR protein conformation studies due to differences in the amide bond orientations within a protein backbone structure that give rise to different vibrational frequencies.[25, 29, 30] The amide II region (1500-1600 cm^{-1}) contains information about the in-plane N-H bend and C-N stretch of the amide bond but is less sensitive to protein conformation.[17, 26, 56] The amide III band (1200-1350 cm^{-1}) is also sensitive to conformation,[41] but was not analyzed in this work due to its weak intensity.

Characteristic amide I peak positions for random coil, β-sheet, and α-helix protein conformations are 1648-1644 cm^{-1}, 1632-1621 cm^{-1}, and 1655-1650 cm^{-1}, respectively.[26] Independent of the starting protein secondary structure and surface functionality, all peak positions shift to higher wavenumbers upon protein adsorption (Table 4.2). The adsorbed protein amide I peak positions were the highest for random coil, aqueous silk fibroin and the lowest for β-sheet, hydrogel silk fibroin. Gold surfaces had the largest peak positions (absolute value) for all three initial protein conformations. The amide I shift to higher wavenumbers may suggest that the proteins are denaturing (irregular secondary structure, ~1671 cm^{-1})[57] or changing to a non-native, aggregated, intramolecular β-sheet structure (1685-1663 cm^{-1})[17, 25, 58] upon adsorption to the substrate. Amide II peak positions are similar for all surfaces and protein conformations.

My *in vitro* FTIR results on SAMs, showing an increase in protein disorder after surface adsorption, are in contrast to the early studies by Weiner and Traub (i.e., silk has β-sheet conformation in nacre).[45] However, recent *in vitro* x-ray and electron diffraction studies of silk – chitin assemblies have not detected any β-sheet silk structure, even though silk is a major organic component.[47, 59] The previous *in vitro* results, as well as those presented in this chapter, suggest silk is disordered at the chitin-silk interface. The increase in protein disorder could be due to the introduction of a functionalized substrate, causing a change in protein stability and structure.[19, 30, 54, 55, 60] The degree of conformational change of a protein adsorbed on a surface will be dependent on the protein-surface interactions and the strength of the internal bonds (i.e., H-bonding) holding the protein in its particular conformation.[17] The β-sheet silk fibroin had the greatest shift in amide I on all surfaces, with the largest change on gold from 1620 to 1673 cm^{-1} (a change of 53 cm^{-1}) indicating the greatest change in conformation upon bonding to the surface. The α-helical BSA had the smallest change in peak position on all surfaces, with the smallest shift on the methyl SAM. Interestingly, the already disordered random coil silk fibroin had a greater shift in peak position than the α-helical structure. The smaller peak shift suggests that BSA has a high surface affinity for each surface functionality based on its inherent secondary structure, whereas the already disordered random coil silk fibroin shows a larger amount of conformation change on bonding. These results indicate that adsorbed proteins rearrange to reach a minimum surface energy regardless of starting conformation.[29, 61, 62]

Based upon literature trends, the interaction of proteins with hydrophobic surfaces is expected to be greater than with hydrophilic surfaces. Hydrophobic surfaces tend to denature adsorbed proteins by forcing proteins to expose internal, hydrophobic residues.[17, 18] My results, however, do not show a clear trend with surface

hydropathy and protein denaturation. All samples have the greatest shift in peak position (i.e., denaturation/rearrangement) on bare gold surfaces, as opposed to methyl terminated SAMs. In addition, proteins adsorbed to all surfaces shift peak positions to higher values as compared to bulk, film values. This result suggests that the presence of a surface alone, regardless of the hydropathy, can cause a protein to change its conformation.

Similar to my results, there are exceptions in literature to the generalization that proteins have a greater interaction with hydrophobic surfaces. For example, a recent study by Jeyachandran and co-workers found that BSA had 95% coverage on hydrophilic surfaces compared to 53% on hydrophobic polystyrene coated surfaces.[30] Other exceptions within the literature present similar exceptions for α-chymotrypsin, albumin, fibrinogen, and kininogen.[48, 63, 64] These examples, coupled with my results, indicate that each protein/surface pair needs to be studied individually rather than making broad assumptions regarding general protein interfacial behavior.

4.3.2.4 Protein adsorption on β-chitin

Previous attempts to obtain FTIR information, from demineralized nacre shell matrices, about the structure of the β-chitin – silk-like protein hydrogel interface have been unsuccessful since the chitin and protein amide peaks overlap making them indistinguishable from each other.[59] *In vitro* protein adsorption on β-chitin was also investigated with FTIR in this study, but the amide stretches (1500-1700 cm^{-1}) from the chitin overshadow any protein amide peaks making accurate protein analysis difficult (Figure 4.10).

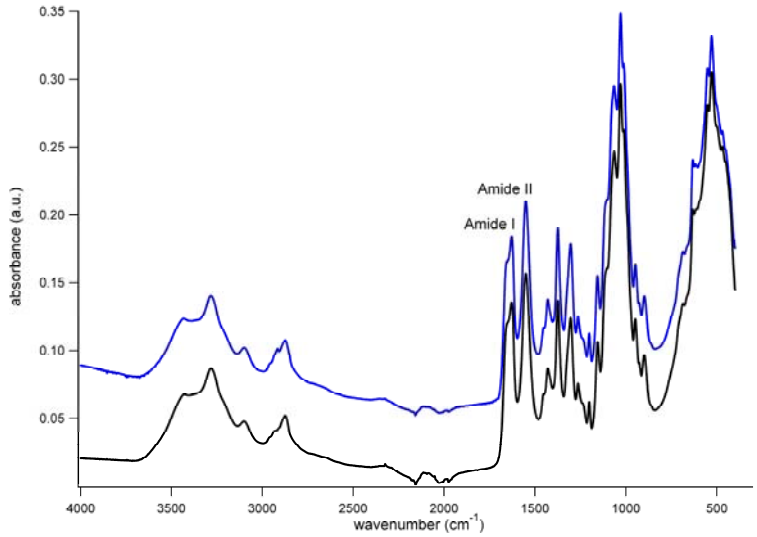

Figure 4.10 FTIR of β-chitin (black) and random coil silk fibroin adsorbed on β-chitin (blue).

4.3.3 Interpretation of Crystallization Results

Based upon the characterization of the organic-organic interface results between silk fibroin and SAMs, the crystallization results (Figures 4.2, 4.3, 4.6, and Table 4.1) can be re-examined.

The higher amounts of silk adsorbed on the methyl SAMs (as compared to the carboxylate SAMs) may explain the observed increase in crystal nucleation density in the presence of silk gels. The silk adsorbs to the surface, which may expose new functional groups to promote crystal nucleation, as compared to control surfaces. Evidence of adsorbed silk on all surfaces can also explain the loss of crystal orientation on the carboxylate SAM. Even though the β-sheet silk adsorbed the least on all surfaces, there is still enough protein to affect calcite orientation. The presence of silk, even in small amounts, may shield or disrupt the carboxylate functionality such that it is no longer able to orient the calcite crystals.

In this study, however, silk fibroin may play a similar role to prisilkin-39, a mollusk prismatic protein with a repetitive amino acid sequence comparable to silk fibroin.[65] Prisilkin-39 simultaneously interacts with both chitin and mineral to inhibit aragonite formation *in vivo*. Other acidic macromolecules, rich in carboxylic acid groups, are known to bind/adsorb onto the chitin surface, which may lead to oriented mineralization.[47] The presence of preferentially adsorbed proteins (i.e., the carboxylic acid rich proteins) *in vivo* may minimize the silk interaction with the substrate. In this model system, other proteins are not present to prevent silk adsorption to the SAMs. The silk, therefore, adsorbs on the surface affecting crystal orientation *in vitro*. The crystallization results, coupled with surface characterization, suggest that studying the complex molecular interfaces (organic-organic and organic-inorganic) *in vitro* can lead to insight into the structure-function relationships of these interfaces *in vivo*.

4.4 Summary

The interaction of protein structure, conformation, and chemistry play an important role in understanding the nacre model system at the organic-inorganic and the organic-organic interfaces. This study highlights that protein adsorption changes the SAM-mineral interface, resulting in a change in calcite crystallization on SAMs with regards to crystal orientation and nucleation density. Upon surface adsorption, protein conformation changes regardless of the initial protein conformation and surface chemistry, whereas, the amount of surface adsorbed protein can be related to the initial protein conformation. Further understanding of these types of interactions at organic matrix interfaces is necessary to better model the origins of biological control over the mineralization process.

4.5 Materials and Methods

4.5.1 Silk fibroin purification

Silk fibroin from *Bombyx mori* cocoons were cut into approximately 1.5 cm pieces and any insect remnants were manually removed. The cocoon material (0.5 g) was boiled in 500 mL of 2 w/v % Marseilles soap (an olive oil based soap originating from Marseilles France) solution for an hour and a half (changing the solution every 30 minutes) followed by 30 minutes in boiling 0.02 M sodium carbonate (Na_2CO_3, J.T. Baker) to solubilize and remove the silk sericin. This purification method was modified from previous procedures.[50, 59] After boiling, the silk was rinsed with copious amounts of water to remove excess salts and/or surfactants. The resulting silk mass was dissolved overnight, at room temperature, in 9.3 M lithium bromide (LiBr, Reagent Plus ≥99%, Sigma-Aldrich). The concentration of the resulting silk solution was approximately 25 wt%. The solubilized silk was then filtered (Whatman filter paper) and dialyzed (Slide-a-Lyzer dialysis cassettes, Pierce, MWCO 3,500). Silk solutions (30 mL) were dialyzed against DI water (3 L) for three days at room temperature, changing the water twice daily. The resulting silk solutions are approximately 5 wt%, which was determined by weighing the remaining solid after air drying. Fresh aqueous silk solutions were either used immediately or capped in glass test tubes (3 mL of solution) and incubated in a hot water bath at 60º C to induce β-sheet formation (resulting in silk gelation). A sample was considered a gel when the vial was inverted and the solution did not fall after 30 seconds.[50]

Silk films were made by drying silk solutions at room temperature. Films were either characterized after drying (for random coil conformation) or treated the films with methanol to induce β-sheet transformation. Dried films were also made from silk gels, but were more brittle and harder to handle.

4.5.2 Self-Assembled Monolayer formation

Gold coated silicon (100) wafers (50 Å titanium adhesion layer then 1000 Å gold) were purchased from Platypus Technologies. The wafer was cut into 1 cm^2 pieces and plasma cleaned immediately before SAM preparation. Methyl ($-CH_3$), carboxyl (-COOH), or poly-ethylene glycol (PEG) terminated SAMs were formed on gold substrates by exposing the surfaces to 10 mM solution of the thiol (1-hexadecanethiol, 16-mercaptohexadecanoic acid, or (1-mercapto-11-undecyl)tetra(ethylene glycol), Sigma) in absolute ethanol for 24 hours, followed by washing with ethanol, then DI water.[7, 44, 66] The carboxylate SAM was formed using acidic ethanol (~pH 2) to increase ordering of the SAM surface by assuring that the carboxyl terminus is protonated during SAM formation, reducing multilayer formation. After rinsing, slides were transferred to petri dishes and immediately used for adsorption GAFTIR and/or crystallization studies.

4.5.3 Protein Adsorption

SAM coated or plasma cleaned bare gold slides were incubated in 5 mg/mL protein solutions (silk fibroin or bovine serum albumin (BSA, Fisherbrand, used without any further purification)) for 24 hours. To avoid variability among protein batches, four SAMs (one of each surface chemistry) was placed in a single petri dish and incubated with the same protein solution for 24 hours. After incubation, slides were removed, rinsed with deionized water, dried under nitrogen, and immediately characterized with GAFTIR.

4.5.4 Circular Dichroism (CD)

The secondary structures of silk fibroin and BSA were verified via CD spectroscopy before use for adsorption studies. Spectra were recorded using a Model 400 Aviv spectrometer with a Peltier thermocouple temperature control. The spectra were recorded from 190 to 250 nm with a 1 nm step. A quartz cuvette (Helma

Worldwide) with a 1 cm path length was used for measurements, and was capped to prevent evaporation. All samples were diluted with DI water to a concentration of ~20 μg/mL for the best signal to noise ratio. Background spectra (DI water) were recorded and subtracted from each sample. Background subtracting and spectra smoothing were all done within the CD software. All theta values are reported as millidegree per milligram (mdeg/mg).

4.5.5 Grazing Angle Fourier Transform Infrared Spectroscopy (GAFTIR)

Infrared analysis of SAM functionality and surface adsorbed protein was conducted using a Bruker Vertex 80v FTIR with a VeeMax II grazing angle accessory and a MCTA detector. The grazing angle was set to 75º and p-polarized light was used to obtain the best spectra for gold coated monolayers. A freshly plasma cleaned bare gold surface was used as the background for all spectra. A Pike Technologies Miracle Diamond ATR was used for control silk film characterization.

The FTIR was vacuum purged for 15 minutes prior to spectra acquisition to ensure elimination of CO_2 and water vapor. Spectra were recorded at 2 cm^{-1} resolution and 256 scans. Spectra were analyzed (peak fitting, position, area, and baseline subtracted) using Igor analysis software.

4.5.6 X-Ray Diffraction (XRD)

X-ray diffraction measurements were performed using a Scintag Theta-Theta Diffractometer with CuKα radiation at 45 kV and 40 mA. Each sample was scanned over a 2θ range of 20-50º with a step size of 0.02º and a count time of 0.3 seconds.

4.5.7 Calcium Carbonate Crystallization

Crystal growth experiments were carried out using a 24 well plate (Nunc) mini-desiccator via the vapor diffusion method. Solid ammonium carbonate ($(NH_4)_2CO_3$, Sigma) was placed in one corner of the plate and covered with crystallization tape with one small hole poked in the center. Solid, anhydrous calcium

chloride ($CaCl_2$, Sigma) as well as aqueous, 7 mM $CaCl_2$ (high purity calcium chloride dihydrate was used for solution crystal growth, Sigma) were placed in between the carbonate source and the crystallization experiment wells to slow diffusion and prevent condensation from forming within the sealed 24 well plate. 1 cm^2 carboxylic acid functionalized gold substrates were put in the bottom of the crystallization wells and covered with 0.5 mL of solution of 10 mM $CaCl_2$. Crystallization experiments were carried out at room temperature for 24 hours, after which substrates were removed, rinsed with DI water, and dried before characterization.

Crystal nucleation densities were tabulated with the use of ImageJ. Grayscale images were thresholded and analyzed. Number of crystals, crystal areas, as well as area fraction (crystal coverage per sample area) was recorded.

REFERENCES

1. Nudelman, F.; Gotliv, B. A.; Addadi, L.; Weiner, S., *J. Struct. Biol.* **2006,** 153, (2), 176-187.

2. Addadi, L.; Moradian, J.; Shay, E.; Maroudas, N. G.; Weiner, S., *Proc. Natl. Acad. Sci. U. S. A.* **1987,** 84, (9), 2732-2736.

3. Keene, E. C.; Evans, J. S.; Estroff, L. A., *Cryst. Growth Des.* **2010,** 10, (3), 1383-1389.

4. Suzuki, M.; Saruwatari, K.; Kogure, T.; Yamamoto, Y.; Nishimura, T.; Kato, T.; Nagasawa, H., *Science* **2009,** 325, (5946), 1388-1390.

5. Weiss, I. M.; Kaufmann, S.; Heiland, B.; Tanaka, M., *J. Struct. Biol.* **2009,** 167, (1), 68-75.

6. Mrksich, M.; Whitesides, G. M., *Annu. Rev. Biophys. Biomolec. Struct.* **1996,** 25, 55-78.

7. Aizenberg, J.; Black, A. J.; Whitesides, G. H., *J. Am. Chem. Soc.* **1999,** 121, (18), 4500-4509.

8. Love, J. C.; Estroff, L. A.; Kriebel, J. K.; Nuzzo, R. G.; Whitesides, G. M., *Chem. Rev.* **2005,** 105, (4), 1103-1169.

9. Aizenberg, J.; Black, A. J.; Whitesides, G. M., *Nature* **1999,** 398, (6727), 495-498.

10. Travaille, A. M.; Kaptijn, L.; Verwer, P.; Hulsken, B.; Elemans, J.; Nolte, R. J. M.; van Kempen, H., *J. Am. Chem. Soc.* **2003,** 125, (38), 11571-11577.

11. Aizenberg, J., *Adv. Mater.* **2004,** 16, (15), 1295-1302.

12. Travaille, A. M.; Steijven, E. G. A.; Meekes, H.; van Kempen, H., *J. Phys. Chem. B* **2005,** 109, (12), 5618-5626.

13. Prime, K. L.; Whitesides, G. M., *Science* **1991,** 252, (5009), 1164-1167.

14. Ostuni, E.; Grzybowski, B. A.; Mrksich, M.; Roberts, C. S.; Whitesides, G. M., *Langmuir* **2003,** 19, (5), 1861-1872.

15. Arima, Y.; Iwata, H., *Biomaterials* **2007,** 28, (20), 3074-3082.

16. Chapman, R. G.; Ostuni, E.; Yan, L.; Whitesides, G. M., *Langmuir* **2000,** 16, (17), 6927-6936.

17. Roach, P.; Farrar, D.; Perry, C. C., *J. Am. Chem. Soc.* **2005,** 127, (22), 8168-8173.

18. Sigal, G. B.; Mrksich, M.; Whitesides, G. M., *J. Am. Chem. Soc.* **1998,** 120, (14), 3464-3473.

19. Servagent-Noinville, S.; Revault, M.; Quiquampoix, H.; Baron, M. H., *J. Colloid Interface Sci.* **2000,** 221, (2), 273-283.

20. Ishiguro, R.; Yokoyama, Y.; Maeda, H.; Shimamura, A.; Kameyama, K.; Hiramatsu, K., *J. Colloid Interface Sci.* **2005,** 290, (1), 91-101.

21. Roach, P.; Farrar, D.; Perry, C. C., *J. Am. Chem. Soc.* **2006,** 128, (12), 3939-3945.

22. Green, R. J.; Hopkinson, I.; Jones, R. A. L., *Langmuir* **1999,** 15, (15), 5102-5110.

23. Taborelli, M.; Eng, L.; Descouts, P.; Ranieri, J. P.; Bellamkonda, R.; Aebischer, P., *J. Biomed. Mater. Res.* **1995,** 29, (6), 707-714.

24. Lenk, T. J.; Horbett, T. A.; Ratner, B. D.; Chittur, K. K., *Langmuir* **1991,** 7, (8), 1755-1764.

25. Byler, D. M.; Susi, H., *Biopolymers* **1986,** 25, (3), 469-487.

26. Miyazawa, T.; Blout, E. R., *J. Am. Chem. Soc.* **1961,** 83, (3), 712-719.

27. Muller, W. S.; Samuelson, L. A.; Fossey, S. A.; Kaplan, D. L., *Langmuir* **1993,** 9, (7), 1857-1861.

28. Ha, S. W.; Tonelli, A. E.; Hudson, S. M., *Biomacromolecules* **2005,** 6, (3), 1722-1731.

29. Mielczarski, J. A.; Dong, J.; Mielczarski, E., *J. Phys. Chem. B* **2008,** 112, (16), 5228-5237.

30. Jeyachandran, Y. L.; Mielczarski, E.; Rai, B.; Mielczarski, J. A., *Langmuir* **2009,** 25, (19), 11614-11620.

31. Kim, H. S.; Hartgerink, J. D.; Ghadiri, M. R., *J. Am. Chem. Soc.* **1998,** 120, (18), 4417-4424.

32. Sethuraman, A.; Vedantham, G.; Imoto, T.; Przybycien, T.; Belfort, G., *Proteins-Structure Function and Bioinformatics* **2004,** 56, (4), 669-678.

33. Furuya, M.; Haramura, M.; Tanaka, A., *Bioorg. Med. Chem.* **2006,** 14, (2), 537-543.

34. Caruso, F.; Furlong, D. N.; Kingshott, P., *J. Colloid Interface Sci.* **1997,** 186, (1), 129-140.

35. Prime, K. L.; Whitesides, G. M., *J. Am. Chem. Soc.* **1993,** 115, (23), 10714-10721.

36. Ta, T. C.; McDermott, M. T., *Anal. Chem.* **2000,** 72, (11), 2627-2634.

37. Laibinis, P. E.; Nuzzo, R. G.; Whitesides, G. M., *J. Phys. Chem.* **1992,** 96, (12), 5097-5105.

38. Nuzzo, R. G.; Dubois, L. H.; Allara, D. L., *J. Am. Chem. Soc.* **1990,** 112, (2), 558-569.

39. Harder, P.; Grunze, M.; Dahint, R.; Whitesides, G. M.; Laibinis, P. E., *J. Phys. Chem. B* **1998,** 102, (2), 426-436.

40. Herrwerth, S.; Eck, W.; Reinhardt, S.; Grunze, M., *J. Am. Chem. Soc.* **2003,** 125, (31), 9359-9366.

41. Surewicz, W. K.; Mantsch, H. H., *Biochim. Biophys. Acta* **1988,** 952, (2), 115-130.

42. Masuda, Y.; Sugiyama, T.; Seo, W. S.; Koumoto, K., *Chem. Mater.* **2003,** 15, (12), 2469-2476.

43. Singh, A.; Lee, I. S.; Myerson, A. S., *Cryst. Growth Des.* **2009,** 9, (2), 1182-1185.

44. Li, H. Y.; Estroff, L. A., *J. Am. Chem. Soc.* **2007,** 129, (17), 5480-5483.

45. Weiner, S.; Traub, W., *FEBS Lett.* **1980,** 111, (2), 311-316.

46. Addadi, L.; Joester, D.; Nudelman, F.; Weiner, S., *Chem. Eur. J.* **2006,** 12, (4), 981-987.

47. Levi-Kalisman, Y.; Falini, G.; Addadi, L.; Weiner, S., *J. Struct. Biol.* **2001,** 135, (1), 8-17.

48. *Proteins at Interfaces II: Fundamentals and Applications*. American Chemical Soceity: Washington, D.c., 1995.

49. Jeyachandran, Y. L.; Mielezarski, E.; Rai, B.; Mielczarski, J. A., *Langmuir* **2009,** 25, (19), 11614-11620.

50. Kim, U. J.; Park, J. Y.; Li, C. M.; Jin, H. J.; Valluzzi, R.; Kaplan, D. L., *Biomacromolecules* **2004,** 5, (3), 786-792.

51. Matsumoto, A.; Chen, J.; Collette, A. L.; Kim, U. J.; Altman, G. H.; Cebe, P.; Kaplan, D. L., *J. Phys. Chem. B* **2006,** 110, (43), 21630-21638.

52. Zhang, M. Q.; Desai, T.; Ferrari, M., *Biomaterials* **1998,** 19, (10), 953-960.

53. Schwinte, P.; Voegel, J. C.; Picart, C.; Haikel, Y.; Schaaf, P.; Szalontai, B., *J. Phys. Chem. B* **2001,** 105, (47), 11906-11916.

54. Karlsson, M.; Ekeroth, J.; Elwing, H.; Carlsson, U., *J. Biol. Chem.* **2005,** 280, (27), 25558-25564.

55. McGuire, J.; Wahlgren, M. C.; Arnebrant, T., *J. Colloid Interface Sci.* **1995,** 170, (1), 182-192.

56. Wu, Y. Q.; Murayama, K.; Czarnik-Matusewicz, B.; Ozaki, Y., *Appl. Spectrosc.* **2002,** 56, (9), 1186-1193.

57. Cerda-Costa, N.; De la Arada, I.; Aviles, F. X.; Arrondo, J. L. R.; Villegas, S., *Biochem. J.* **2009,** 48, (44), 10582-10590.

58. Cordeiro, Y.; Kraineva, J.; Suarez, M. C.; Tempesta, A. G.; Kelly, J. W.; Silva, J. L.; Winter, R.; Foguel, D., *Biophys. J.* **2006,** 91, (3), 957-967.

59. Falini, G.; Weiner, S.; Addadi, L., *Calcif. Tissue Int.* **2003,** 72, (5), 548-554.

60. Zeng, H. T.; Chittur, K. K.; Lacefield, W. R., *Biomaterials* **1999,** 20, (4), 377-384.

61. Mbamala, E. C.; Ben-Shaul, A.; May, S., *Biophys. J.* **2005,** 88, (3), 1702-1714.

62. Halter, M.; Antia, M.; Vogel, V., *J. Controlled Release* **2005,** 101, (1-3), 209-222.

63. You, C. C.; De, M.; Han, G.; Rotello, V. M., *J. Am. Chem. Soc.* **2005,** 127, (37), 12873-12881.

64. Lin, Y. S.; Hlady, V.; Janatova, J., *Biomaterials* **1992,** 13, (8), 497-504.

65. Kong, Y.; Jing, G.; Yan, Z.; Li, C.; Gond, N.; Zhu, F.; Li, D.; AZHang, Y.; Zheng, G.; Wang, H.; Xie, L.; Zhang, R., *J. Biol. Chem.* **2009,** 284, (16), 10841-10854.

66. Larsen, N. B.; Biebuyck, H.; Delamarche, E.; Michel, B., *J. Am. Chem. Soc.* **1997,** 119, (13), 3017-3026.

CHAPTER 5

SILK FIBROIN HYDROGELS COUPLED WITH THE N16N – β-CHITIN COMPLEX: AN *IN VITRO* ORGANIC MATRIX FOR CONTROLLING CALCIUM CARBONATE MINERALIZATION[*]

5.1 Abstract

As demonstrated in Chapter 2, the nacre specific peptide, n16N, has a binding affinity for β-chitin. The n16N-chitin assembly is able to selectivity nucleate aragonite. Here, I present a more complex *in vitro* assay in which silk fibroin hydrogels are added to the experimental assay. Crystallization, with silk and n16N on β-chitin, results in metastable vaterite and amorphous calcium carbonate which form as flat deposits with hemispherical centers. X-ray diffraction suggests that the vaterite crystals may be oriented with respect to the β-chitin fibrils. Fluorescence imaging of bound peptide show that n16N binds to β-chitin in the presence of silk. My results demonstrate that, with the addition of the silk fibroin hydrogel, both orientation and morphological control of calcium carbonate can be achieved.

5.2 Introduction

As discussed in Chapter 2, the peptide, n16N, is an intrinsically disordered peptide that can fold upon interaction with a target. Previous studies have shown that n16N interacts with calcium carbonate[1, 2] as well as β-chitin,[3] and may also be part of a larger protein complex.[4] Here I increase the complexity of my synthetic experimental assay with the addition of another organic matrix component, silk fibroin hydrogels, to the n16N – β-chitin system.

[*] E. C. Keene, J. S. Evans, and L. A. Estroff, in preparation.

Falini et al. demonstrated the importance of silk fibroin in an *in vitro* assay.[5] Calcium carbonate was grown on a substrate of β-chitin and silk fibroin with the addition of adsorbed soluble macromolecules from either the calcitic or aragonitic layers. The results suggest that polymorphic control (aragonite formation) was only possible with the complete substrate assembly (i.e., all three components).

Previous *in vitro* studies, including Falini's assay (see section 1.4.1), do not use silk hydrogels but rather silk films or solutions. Cryo-TEM and environmental SEM studies of nacre, however, have shown that the silk-like protein is a weakly ordered β-sheet, hydrated gel.[6, 7] In addition to the silk-like hydrogel in nacre, there are multiple other examples of gels in biomineralization including amelogenin gels associated with tooth enamel formation[8] and collagen-like protein gels in otolith formation.[9] While the exact role of silk fibroin in nacre growth is unknown, possible roles have been speculated.[7] The environment in a hydrogel for crystallization differs from solution growth in diffusion rates, ion activities, and water "structure" (in hydrophobic gels). Hydrogels can also act as a site directing agent by suppressing crystallization and therefore, preventing uncontrolled crystallization until nutrients are in contact with the nucleating site or with already formed mineral. With the addition of a protein hydrogel to the n16N - β-chitin assembly, I can more accurately model the hypothesized organic matrix of nacre, as well as increase the complexity of the *in vitro* model. Therefore, we can build on our understanding of the complete nacre organic matrix.

5.3 Results

5.3.1 Crystallization

The addition of a silk hydrogel to the mineralization assay changes the microenvironment (i.e., organic-inorganic interface) for mineralization (Figure 4.1). Experimental controls, in the presence of silk, on β-chitin, form poly-crystalline calcite (Figure 5.1A). As reported in Chapter 2, crystals grown on β-chitin in the presence of n16N form randomly oriented, poly-crystalline aragonite crystals (Figure 2.1C).[3] With the addition of silk fibroin to the n16N – β-chitin complex, flat deposits, with a rounded, three-dimensional center, form (Figure 5.1B). Visually, the flat regions appear to be elongated along the chitin fibers. The chitin aligned mineral are similar to the polycrystalline calcite aggregates grown on β-chitin with p-Glu seen in Chapter 2 (Figure 2.4)

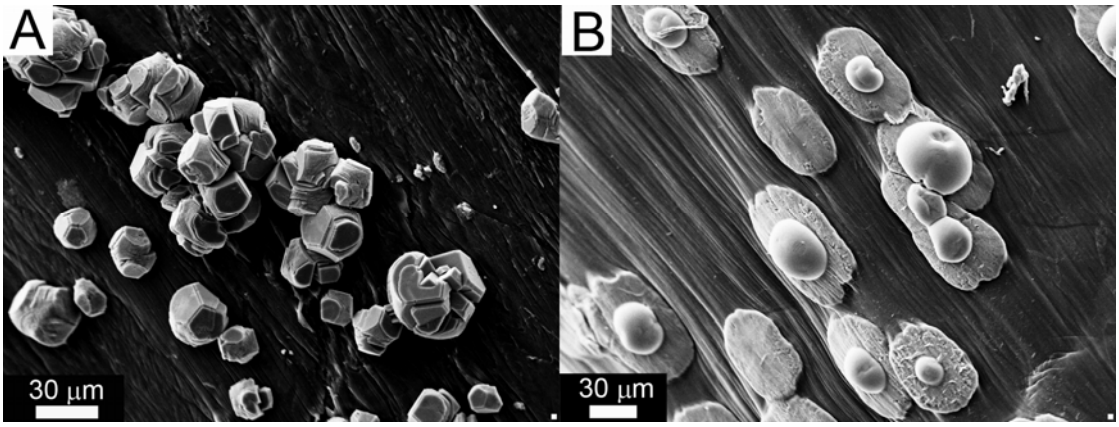

Figure 5.1 SEM micrographs of calcium carbonate crystallization on β-chitin with 2.5 wt% silk fibroin hydrogel (A) and 10 μM n16N (B).

Under cross-polarizers (optical microscopy) the outer, flat regions remain dark, while the center three-dimensional regions remain bright suggesting amorphous and

poly-crystalline material, respectively (Figure 5.2). Raman spectra indicate that these crystals may be a mixture of amorphous calcium carbonate (ACC) and vaterite due to the relatively weak intensity of the characteristic peaks (peaks labeled in Figure 5.3).[10] General area x-ray diffraction (GADDs) shows vaterite reflections, and also a minor calcite component (Figure 5.4). GADDs data also shows some alignment of the vaterite reflections with the chitin (102) reflection.

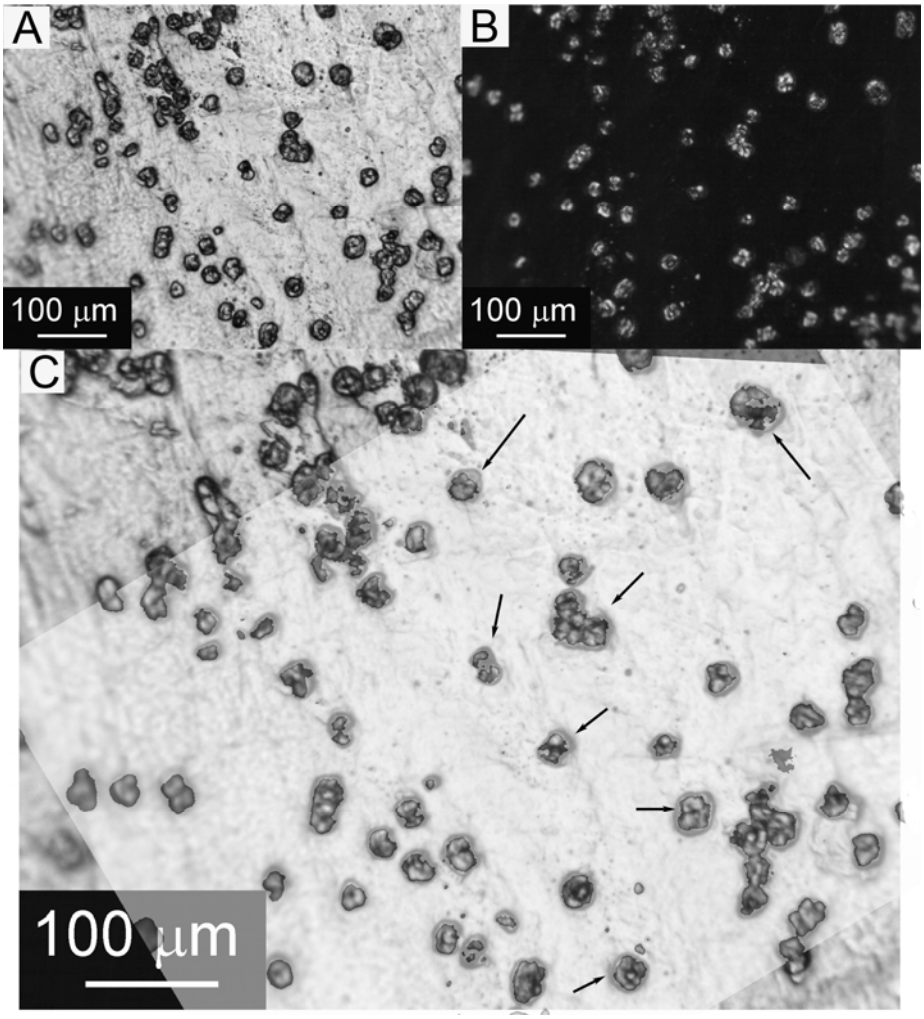

Fgure 5.2 Optical microscope images of crystals grown on β-chitin with 2.5 wt% silk gel and 10 μM n16N. (A) Bright field image, (B) sample rotated 30° under cross-polars, and (C) an overlay of the bright field and polarized image. Black arrows highlight the flat, outer regions that are dark under cross-polars.

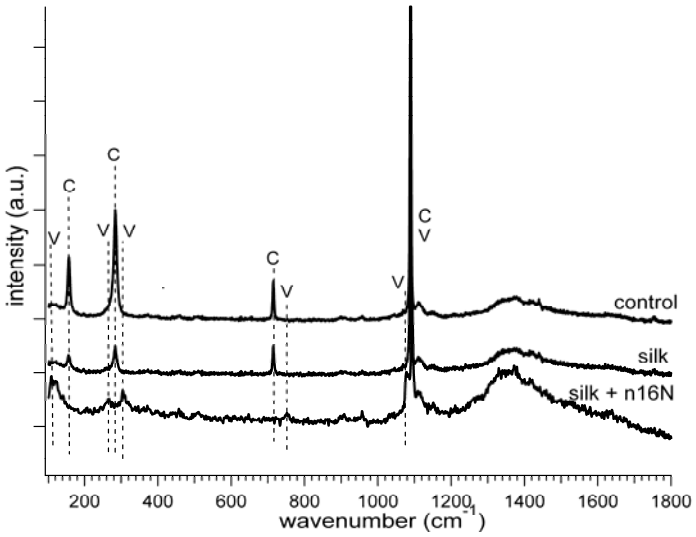

Figure 5.3 Raman spectra of calcium carbonate grown on β-chitin. Top spectrum (control) = no additives, middle (silk) = 2.5 wt% silk fibroin gel, bottom (silk + n16N) = 2.5 wt% silk fibroin gel and 10 μM n16N. Crystal polymorphs, indicated by *C* and *V*, denote characteristic calcite and vaterite peaks, respectively.

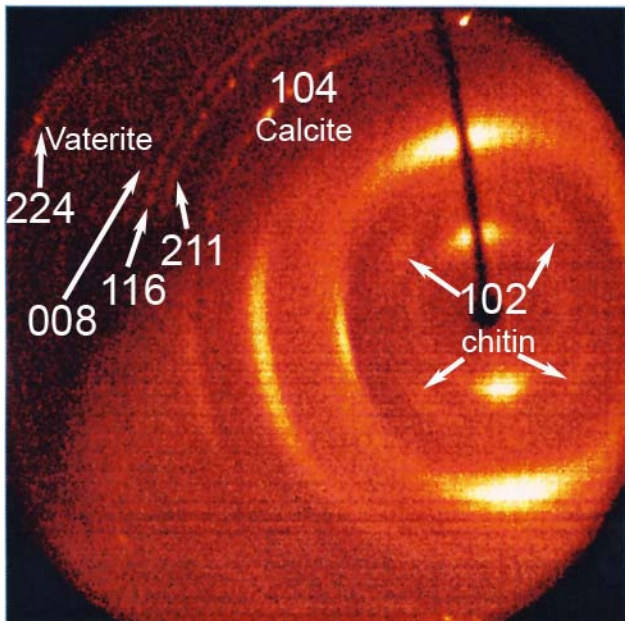

Figure 5.4 X-ray diffraction of crystals grown on β-chitin substrate with 2.5 wt % silk fibroin and 10 μM n16N. Relevant crystalline reflections are labeled with white arrows and indices on spectrum.

The complete organic matrix assembly has been shown to be crucial for the control of crystallization. By modifying the matrix, further information regarding the organic assembly can be gained.

Crystals grown in the bulk gel (silk + n16N, no chitin) were isolated and characterized. The majority of the crystals are calcite with minor morphological affects (Figure 5.5). Experiments were also performed with aqueous, random coil silk to study the affect of protein secondary structure and state (aqueous versus hydrogel). However, when n16N was mixed with aqueous silk, an insoluble precipitate forms. Therefore, experiments with random coil silk and n16N were discarded. When silk is added to a β-sheet hydrogel, this affect is not seen.

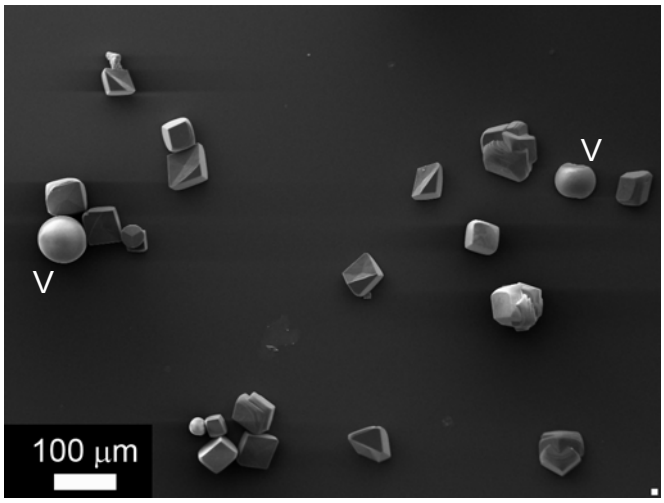

Figure 5.5 SEM micrograph of isolated bulk gel grown crystals (2.5 wt% silk fibrion gel + 10 μM n16N with underlaying β-chitin substrate). The majority phase is calcite (*V* index minority vaterite phase).

Both α-chitin and synthetic SAMs (carboxylate- and methyl-terminated alkanethiols on gold) were tested in place of β-chitin. Only polycrystalline calcite

forms (Figure 5.6) with similar morphologies to control crystals (no peptide) grown in the presence of silk gel (see Figure 4.4B for comparison).

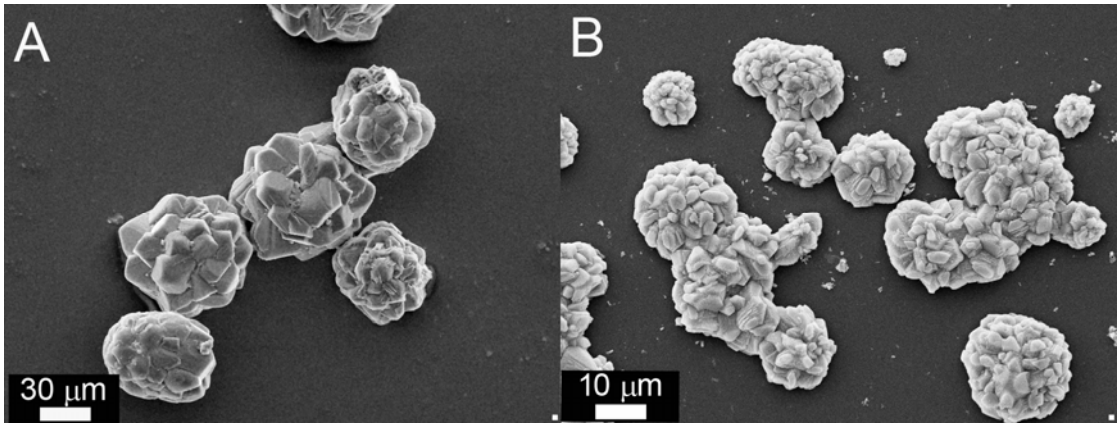

Figure 5.6 SEM micrographs, 2.5 wt% silk fibroin hydrogel with 10 μM n16N on a methyl-terminated SAM (A) and on α-chitin (B).

Different water-soluble additives, to substitute for n16N, were also tested as modifications of the main assay. The n16N variants (n16NN and n16Ns),[11] with the addition of silk fibroin and β-chitin, produce similar results as the native peptide (Figure 5.7). There is a flat, outer region with a rounded center, with similar characteristic vaterite/ACC Raman peaks seen in Figure 5.3. When n16N is substituted for a simple acidic polypeptide (p-Asp or p-Glu) with silk on β-chitin, crystals appear to grow into the chitin substrate (Figure 5.8A and B), while on synthetic SAMs poly-crystalline calcite forms (Figure 5.8C). The flat structures formed with p-Glu + silk crystals on β-chitin are reminiscent of the flat ACC/vaterite crystals of Figure 5.1B, however, they are calcite (Figure 5.8D).

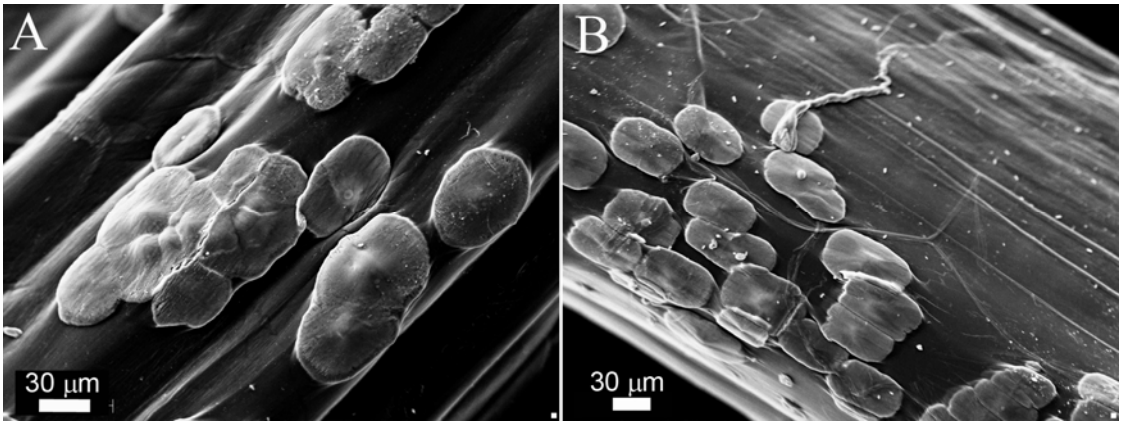

Figure 5.7 SEM micrographs of f crystals grown on β-chitin in the presence of 2.5 wt% β-sheet silk fibroin gel and (A) 10 μM n16NN or (B) 10 μM n16Ns.

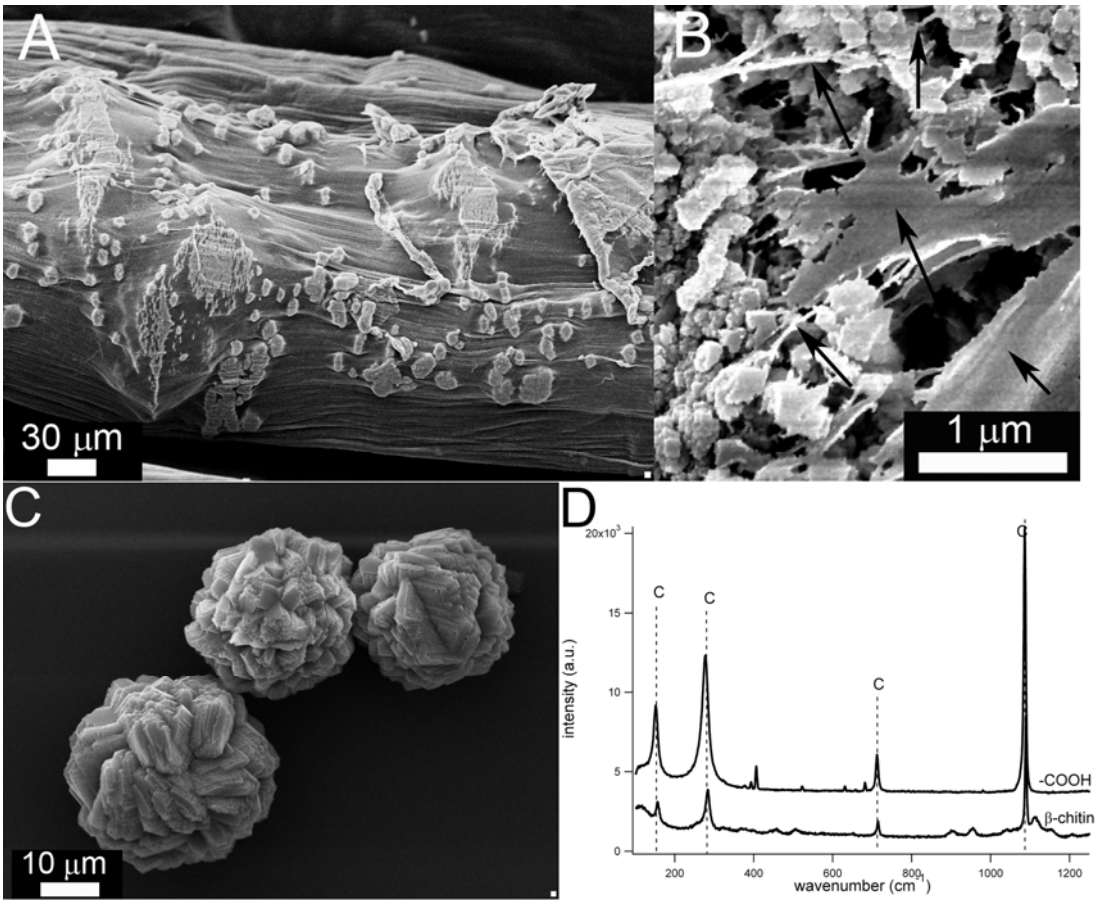

Figure 5.8 SEM micrographs of crystals grown in the presence of p-Glu and 2.5 wt % β-sheet silk fibroin gel on β-chitin (A and B) or on carboxylate-terminated SAM (C). Image magnification (B) shows crystals growing into the chitin substrate. Black arrows highlight β-chitin material. Raman spectra (D) of crystals grown on either a carboxylate-terminated SAM (top) or on β-chitin (bottom).

To learn more about the composition of the mineral deposits, etching and time dependent growth studies were carried out. Crystals were aged for 2 days (dry at room temperature). Visually, the samples appear more crystalline: the center regions have typical poly-crystalline, spherulitic morphologies (often seen with vaterite spherulites), while the flat regions appear to have a rougher texture (Figure 5.9).

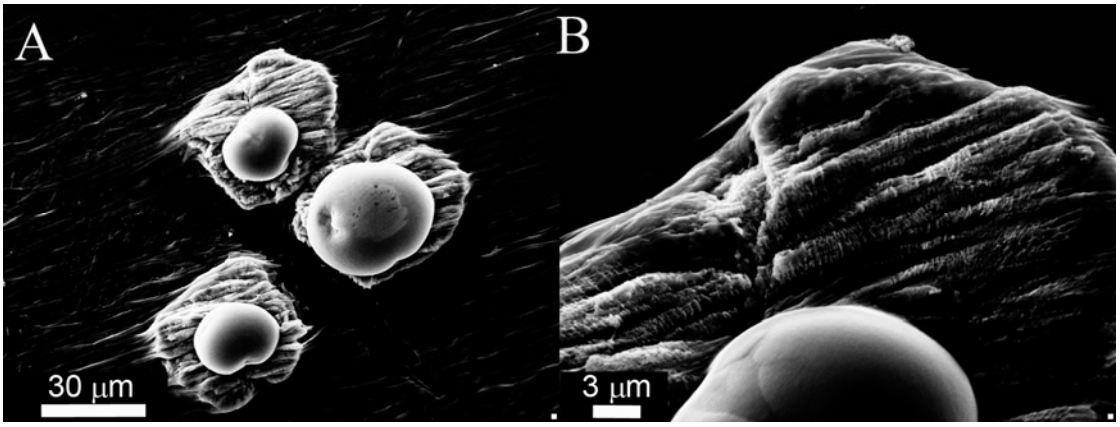

Figure 5.9 SEM micrographs of crystals aged, dry at room temperature, for 2 days.

Samples were etched to investigate the possible amorphous materials, as ACC has a higher solubility than crystalline $CaCO_3$.[12, 13 14] When samples were etched with DI water, and the outer, flat regions dissolved away first (Figure 5.10A). Sample magnification reveals that there is an indent in the chitin substrate where the flat material had been (Figure 5.10A, inset). Energy Dispersive X-ray (EDX) analysis of the etched crystals verifies the presence of calcium in the center region, while the outer flat deposits were completely etched away (Figure 5.11). Crystals were also etched with 1M KOH, believed to selectively etch ACC.[14] Both flat and spherulitic regions become etched. The centers are more affected by the KOH etching process: the centers are completely dissolved (Figure 5.10B).

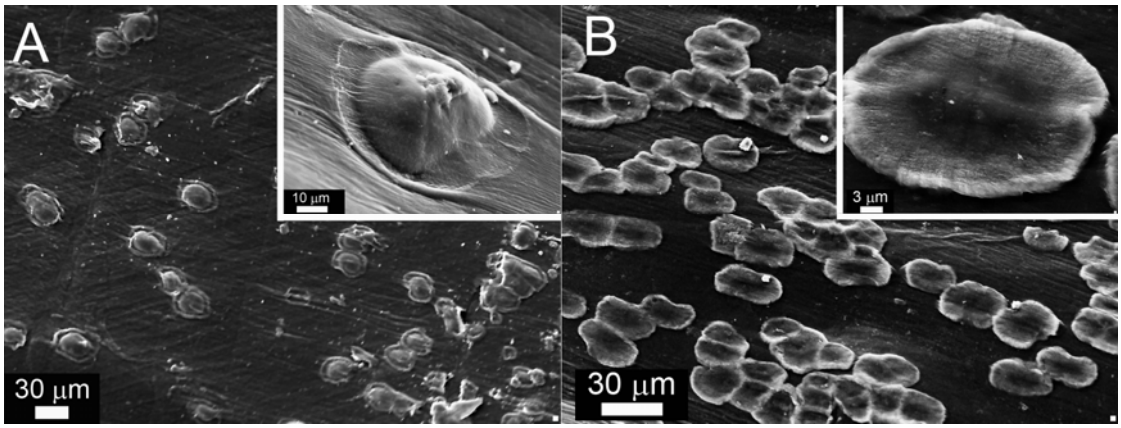

Figure 5.10 SEM micrographs of etched samples in (A) DI water for 20 hours or (B) 1M KOH (to selectively etch ACC) for 8 hours. Figure insets are magnified regions of one structure each.

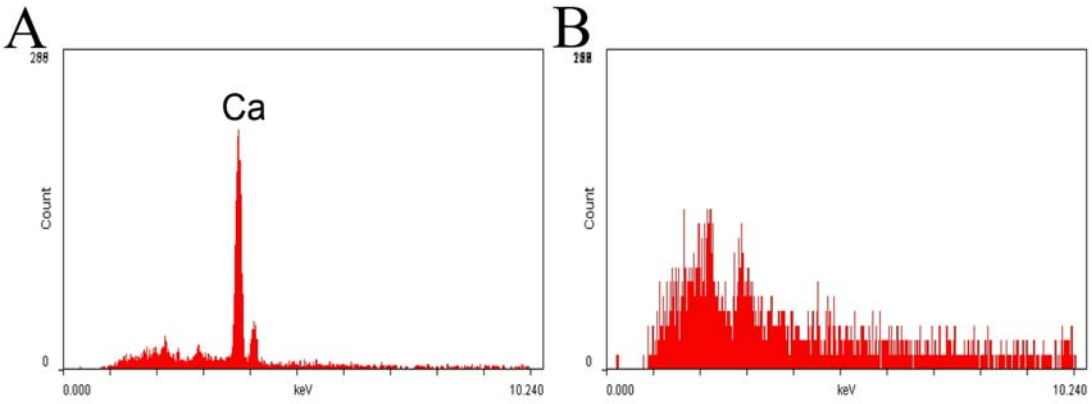

Figure 5.11 EDX of mineral deposits in Figure 5.11A, inset. (A) Center region and (B) outer indented region.

Timed growth experiments were utilized to monitor early mineral growth stages, when transient, metastable phases are often observed.[15-18] Crystals grown for shorter time periods (4 and 6 hours) form the spherulitic regions first, followed by the flat regions (Figure 5.12).

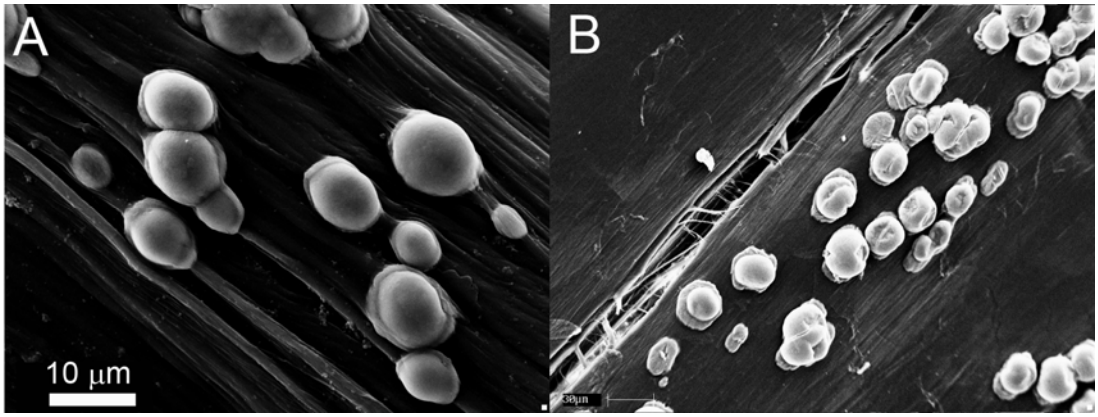

Figure 5.12 SEM micrographs of crystals grown for (A) 4 hours or (B) 6 hours.

Chapter 2 demonstrated n16N has a binding affinity for β-chitin. To investigate the effect of silk fibroin on the binding affinity of n16N, crystals were grown on chitin pieces that were incubated with silk fibroin and n16N. Unlike in Chapter 2, where aragonite selectivity remained after n16N incubation, with the addition of silk fibroin, both morphology and polymorph are lost. Only poly-crystalline calcite forms (Figure 5.13).

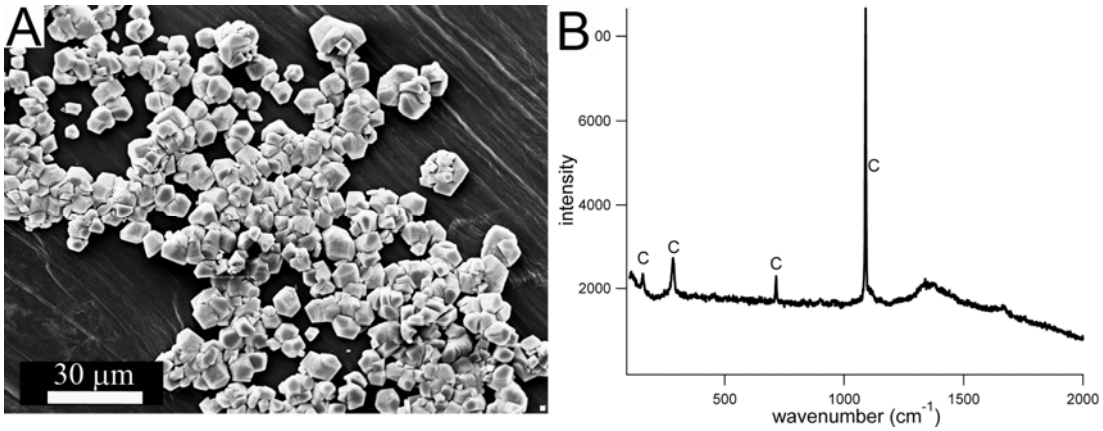

Figure 5.13 SEM micrograph (A) of β-chitin substrate with adsorbed n16N and silk fibroin. Raman spectrum characterizing crystal polymorph (B), where *C* denotes calcite.

5.3.2 Characterization of the organic assembly

To investigate the organic-organic interface (chitin – protein/peptide, Figure 4.1), further experiments were performed. Fluorescence labeling was used to investigate β-chitin - silk/n16N interface binding interactions. The fluorescence dye, BODIPY FL, binds to Cys groups of proteins or peptides.[3] Control fluorescence experiments of β-chitin incubated with silk alone do not fluoresce, suggesting that either the silk does not become labeled in this fluorescence assay (there is less than 1% Cys content in silk fibroin[19]) or there is no bound silk (Figure 5.14A). Another fluorescence control, silk and BSA incubated with β-chitin, show moderate fluorescence (<150 pixel brightness, Figure 5.14B). BSA is known to non-specifically bind to surfaces, and has Cys groups that can be labeled with BODIPY FL.[3] The majority of non-specifically bound protein should be removed with the appropriate washing procedures.[3, 20-22]

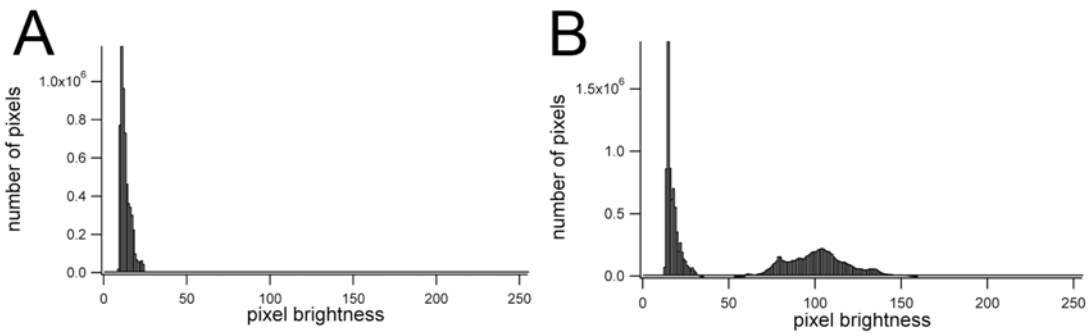

Figure 5.14 Summed histogram of BODIPY FL labeled chitin substrates incubated with 2.5 wt% silk fibroin hydrogel (A) and BSA (B).

Fluorescence labeling of adsorbed silk/n16N on chitin was obtained under two conditions: first, with a mixture of adsorbed silk and n16N, and second, with silk incubation first, followed by n16N. In both cases the chitin shows strong fluorescence

(> 200 pixel brightness), suggesting that the silk is not preventing n16N from binding to β-chitin (Figure 5.15). Chitin substrates incubated with a mixture of silk and peptide show a stronger fluorescence (more pixels at higher brightness levels) than the peptide adsorbed on chitin after silk.

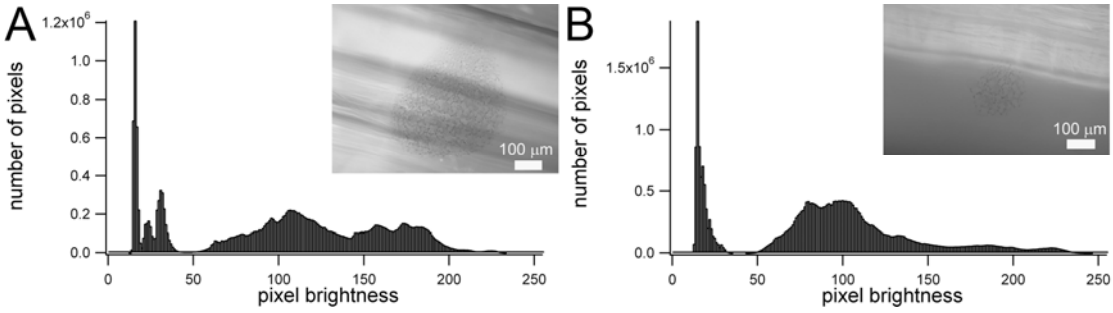

Figure 5.15 Representative fluorescence micrographs and summed histograms compiled from triplicate experiments of BODIPY FL labeled chitin substrates incubated with a mixture of n16N and silk fibroin (A) or incubation with n16N after silk fibroin incubation (B).

5.4 Discussion

This study demonstrates the importance of the complete organic matrix assembly from nacre for controlling crystal growth. XRD, Raman, and etching experiments all confirm the presence of metastable vaterite and ACC (Figures 5.3, 5.4, and 5.10). Ostwald's rule of stages (Figure 1.1) states that the pathway to the final crystalline state will pass through all less stable states in order of increasing thermodynamic stability.[23] ACC is a metastable phase and rapidly transforms into a crystalline phase without the addition of organic stabilizers.[13] The use of amorphous material is widespread in biology, and recently, it has been demonstrated that the

formation of calcium carbonate crystals in biological systems (such as mollusks) may occur through the formation of ACC which later converts to a more stable phase.[12, 24, 25] Under biological control (i.e., biomacromolecules), the amorphous material crystallizes in a controlled manner to form the desired crystalline polymorph and morphology.[26]

In this study, the conversion of ACC to a crystalline phase (vaterite), with silk fibroin and n16N, is not entirely unexpected. Aged samples (Figure 5.10) and timed growth experiments (Figure 5.12) suggest ACC forms at initial growth stages, and subsequently, slowly crystallize into vaterite. With these samples, a conversion to calcite is never seen. In the case of p-Asp/p-Glu with silk, ACC converts to calcite (Figure 5.8). From the literature, an *in vitro* experiment with CAP-1, a crayfish protein, was able to nucleate unidirectionally oriented calcite thin films on α-chitin through an amorphous precursor phase.[27] This protein, which has an α-chitin binding motif, is speculated to interact with both the chitin and the nucleating crystal.

On chitin, CAP-1 and p-Asp/p-Glu with silk result in a conversion of ACC to the thermodynamically stable calcite. The peptide, n16N, in combination with β-chitin and silk, is different. Together, n16N and silk are able to stabilize a metastable phase (vaterite). However, no further recrystallization to aragonite is observed. The experimental assay could be modified further, such that with the appropriate organic modifiers (in addition to n16N, silk fibroin, and β-chitin), ACC may convert to aragonite.

There are two possible organic matrix interactions affecting mineralization: silk and n16N may separately interact with the forming mineral (Figure 5.17A) or a silk – n16N complex may be forming (Figure 5.17B).

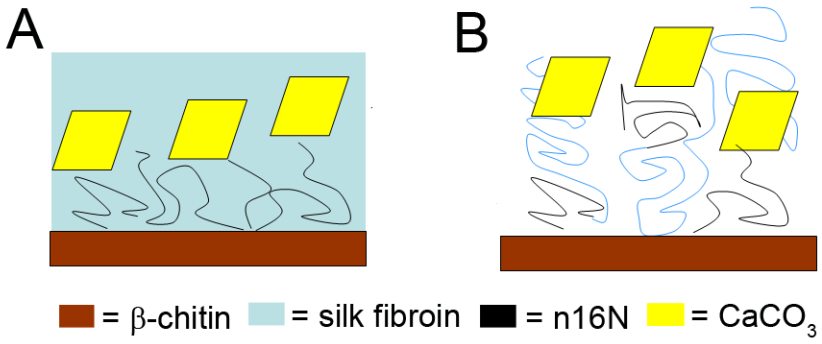

Figure 5.16 Two possible schematics of the complete organic assembly. Silk fibroin and n16N may interact with the growing crystals separately (A) or as a larger protein complex (B).

It is known that n16N is an intrinsically disordered peptide (IDP).[28] IDPs are unfolded in their monomeric state, but can undergo folding upon interaction with a "target".[29-33] The IDP nature of n16N may lead to different structures with and without the addition of the silk fibroin. In Chapter 2, I suggested that the unstable, partially unfolded structure of n16N facilitates interactions with β-chitin, such that internal stabilization (i.e., folding) of the n16N sequence occurs upon binding. This interaction with chitin may present certain functional groups at the organic-inorganic interface leading to aragonite selectivity.[3] Silk fibroin may disrupt this interaction. The fluorescence results demonstrate that n16N still binds to chitin in the presence of silk, but the crystallization results suggest that the peptide conformation/structure may have changed since the aragonite selectivity is lost (Figure 5.16A). Instead, two metastable phases, vaterite and/or ACC, form. It is possible that the silk fibroin, a known inhibitor of crystallization,[7] is suppressing crystal growth causing the metastable phase(s) to form, as well as a change in crystal morphology.

Alternatively, the complete organic matrix (chitin + n16N + silk gel) may promote the metastable phases. A recent report suggests that n16 is part of a larger protein complex.[4] If the n16N and silk fibroin hydrogel are forming a larger protein complex (Figure 5.16B), together they could play a similar role to prisilkin-39, a mollusk prismatic layer protein. Prisilkin-39 has a highly repetitive amino acid sequence reminiscent of silk fibroin and serves a dual role in prismatic layer formation.[22] This protein binds tightly to chitin, as well as inhibits crystallization (especially aragonite formation, even in the presence of magnesium). The presence of the β-sheet silk fibroin hydrogel in nacre may interact with both the acidic macromolecules and as well as the chitin matrix. The presence of silk appears to help charged molecules penetrate the chitin.[34, 35] The indent left in chitin, after the flat region is etched away by water (Figure 5.10A), suggests that mineral may have grown into the porous chitin substrate. Crystals grown with silk and p-Glu grow into the chitin substrate, on and around the chitin fibers (Figure 5.8). The intercalation of silk (and possibly other charged molecules) into the chitin matrix is consistent with previous results, which have suggested that silk penetrates the porous chitin framework.[34, 35]

Crystal growth, in the presence of all three organic components, can affect crystal polymorph, morphology, and orientation.[3-5] When the nucleating substrate is changed (α-chitin or SAMs) or removed (bulk gel crystal growth) only randomly oriented calcite crystals are observed, similar to control experiments. Previous fluorescence results demonstrated n16N does not have a binding affinity for α-chitin, and therefore does not selectivity nucleate aragonite (Chapter 2).[3] The addition of silk to n16N – α-chitin/SAM does not change this result. However, in this chapter, fluorescence studies demonstrate that silk does not prevent n16N from binding to β-chitin. GAFTIR results (from Chapter 4) demonstrate that silk adsorbs to various

surfaces. Therefore, when silk is adsorbed to chitin prior to n16N, there may be some non-specific binding of the silk to occupy sites that n16N could have become bound. When silk and n16N are incubated together, there is a stronger fluorescence, such that n16N may preferentially bind to chitin over silk. It is currently unknown whether n16N is structured or oriented on β-chitin, and whether the addition of silk changes this interface.

In summary, by systematically increasing the complexity of a crystallization assay, the roles of individual macromolecules can become known, as well as further control over *in vitro* crystallization can be gained. More specifically, I found that with addition of a silk fibroin hydrogel to the n16N – β-chitin system, crystal orientation and morphological control could be gained.

5.5 Materials and Methods

5.5.1 Peptide Synthesis and Purification

The 30-mer polypeptide, n16N, representing the 1-30 AA domain of native n16 (AYHKKCGRYSYCWIPYDIERDRYDNGDKKC), was synthesized using the protocol described in earlier work.[1, 2, 28] The 30 AA randomly scrambled version of n16N (n16Ns, EPRYCKWCDNKHGDRAGCKYSIDYYKIRDY), and the globally substituted Asp → Asn, Glu → Gln version, n16NN (AYHKKCGRYSYCWIPYNIQRNRYNNGNKKC) were also synthesized and purified as described.[11] All three peptides were synthesized in the C-amide "capped" form.

Poly-L-aspartic and poly-L-glutamic acid (Sigma Aldrich) were used without further purification.

5.5.2 Silk fibroin Purification and Gelation

Silk fibroin from *Bombyx mori* (silkworm) cocoons were purified as previously described (see Chapter 3 and 4). Silk hydrogels were formed as described in Chapter 3 and 4.

5.4.3 Chitin Purification/Preparation

Squid pen (β-chitin), from the *Loligo* species, was purified as described in Chapter 2. Before crystallization experiments, β-chitin pieces were rehydrated in 10 mM calcium chloride ($CaCl_2$) for a minimum of 2 hours.

5.5.4 Crystallization Experiments

Crystallization experiments were carried out via the vapor diffusion method (as described in previous chapters (Chapters 2 & 4) for 24 hours. Shorter crystallization times were also tested (4 and 6 hours). Bulk gel grown crystals were isolated by mixing bleach (sodium hypochlorite, Fisher) with the silk gel, after the chitin substrate had been removed. The bleach-silk mixture was then centrifuged (Eppendorf Centrifuge 5415C, 5 minutes, 8,000 g), supernatant removed, and rinsed with bleach followed by DI water. After last centrifugation, crystals were resuspended in ethanol and the ethanol-crystal mixture was placed on glass coverslips and air dried before characterization. All crystallization experiments were done in triplicate.

5.5.5 Crystal Etching

The crystals were etched in deionized (DI) water for 20 hours. During this time, the samples were gently agitated on a rocking table. After etching, the samples were air dried and characterized. To selectively etch ACC, crystals were etched with 1M KOH for 8 hours.[14]

5.5.6 Morphology and Polymorph Analysis

The morphology of grown crystals was examined via polarized light microscopy (Leica) and via scanning electron microscopy (SEM, Leica Stereoscan

440, 15 kV, 900 pA) after they were coated with a thin layer of Au/Pd. Elemental composition was identified by Energy Dispersive X-ray analysis (EDX, detector: Kevex; analyzer and software: Evex). The polymorph of the grown crystals was determined via Raman (Renishaw InVia micro-Raman system, 785 nm excitation frequency) and via x-ray diffraction (Bruker General Area Diffraction Detector System, transmission mode, 40 mA, 40kV). Chitin x-ray structural parameters were assigned based upon literature values.[35-37]

5.5.7 Adsorption experiments

Similar to Chapter 2, chitin substrates were incubated with solutions of 5 μM n16N plus 2.5% β-sheet silk fibroin on a rocking table at room temperature for 24 hours to allow the peptide/protein time to adsorb from solution onto the chitin substrate. Chitin samples that were incubated with silk and peptide separately were rinsed with DI water only between incubations. After 24 hours, substrates were washed with DI water, saline solution (0.2 M NaCl), buffer (10 mM Tris, pH 7.2), and finally DI water again to remove any unbound protein. Substrates were immediately used for crystal growth or fluorescence experiments.

5.5.8 Fluorescence experiments

Substrates with adsorbed peptide were reacted with BODIPY FL *N*-(2-aminoethyl) maleimide (Invitrogen) according to manufacturer's instructions with the modifications described in Chapter 2. Specimens were imaged via fluorescence microscopy (Olympus BX51 equipped with a Roper Cool Snap CCD Camera, 100 msec exposure time) using the Image Pro imaging software package. All images were processed in ImageJ as described in Chapter 2.

REFERENCES

1. Kim, I. W.; DiMasi, E.; Evans, J. S., *Cryst. Growth Des.* **2004,** 4, (6), 1113-1118.

2. Kim, I. W.; Darragh, M. R.; Orme, C.; Evans, J. S., *Cryst. Growth Des.* **2006,** 6, (1), 5-10.

3. Keene, E. C.; Evans, J. S.; Estroff, L. A., *Cryst. Growth Des.* **2010,** 10, (3), 1383-1389.

4. Suzuki, M.; Saruwatari, K.; Kogure, T.; Yamamoto, Y.; Nishimura, T.; Kato, T.; Nagasawa, H., *Science* **2009,** 325, (5946), 1388-1390.

5. Falini, G.; Albeck, S.; Weiner, S.; Addadi, L., *Science* **1996,** 271, (5245), 67-69.

6. Levi-Kalisman, Y.; Falini, G.; Addadi, L.; Weiner, S., *J. Struct. Biol.* **2001,** 135, (1), 8-17.

7. Addadi, L.; Joester, D.; Nudelman, F.; Weiner, S., *Chem. Eur. J.* **2006,** 12, (4), 981-987.

8. Moradian-Oldak, J., *Matrix Biol.* **2001,** 20, (5-6), 293-305.

9. Murayama, E.; Takagi, Y.; Ohira, T.; Davis, J. G.; Greene, M. I.; Nagasawa, H., *Eur. J. Biochem.* **2002,** 269, (2), 688-696.

10. Kontoyannis, C. G.; Vagenas, N. V., *Analyst* **2000,** 125, (2), 251-255.

11. Delak, K.; Collino, S.; Evans, J. S., *Langmuir* **2007,** 23, (24), 11951-11955.

12. Politi, Y.; Arad, T.; Klein, E.; Weiner, S.; Addadi, L., *Science* **2004,** 306, (5699), 1161-1164.

13. Addadi, L.; Raz, S.; Weiner, S., *Adv. Mater.* **2003,** 15, (12), 959-970.

14. Aizenberg, J.; Lambert, G.; Weiner, S.; Addadi, L., *J. Am. Chem. Soc.* **2002,** 124, (1), 32-39.

15. Wolf, S. E.; Leiterer, J.; Kappl, M.; Emmerling, F.; Tremel, W., *J. Am. Chem. Soc.* **2008,** 130, (37), 12342-12347.

16. Quigley, D.; Rodger, P. M., *J. Chem. Phys.* **2008,** 128, (22).

17. Pichon, B. P.; Bomans, P. H. H.; Frederik, P. M.; Sommerdijk, N., *J. Am. Chem. Soc.* **2008,** 130, (12), 4034-4040.

18. Lakshminarayanan, R.; Loh, X. J.; Gayathri, S.; Sindhu, S.; Banerjee, Y.; Kini, R. M.; Valiyaveettil, S., *Biomacromolecules* **2006,** 7, (11), 3202-3209.

19. Zhou, C. Z.; Confalonieri, F.; Jacquet, M.; Perasso, R.; Li, Z. G.; Janin, J., *Proteins-Structure Function and Genetics* **2001,** 44, (2), 119-122.

20. Weiss, I. M.; Schonitzer, V., *J. Struct. Biol.* **2006,** 153, (3), 264-277.

21. Suzuki, M.; Nagasawa, H., *FEBS J.* **2007,** 274, (19), 5158-5166.

22. Kong, Y.; Jing, G.; Yan, Z.; Li, C.; Gond, N.; Zhu, F.; Li, D.; AZHang, Y.; Zheng, G.; Wang, H.; Xie, L.; Zhang, R., *J. Biol. Chem.* **2009,** 284, (16), 10841-10854.

23. De Yoreo, J. J.; Vekilov, P. G., Principles of crystal nucleation and growth. In *Biomineralization*, Dove, P. M.; DeYoreo, J. J.; Weiner, S., Eds. Mineralogical Soc America: Washington, 2003; Vol. 54, pp 57-93.

24. Weiss, I. M.; Tuross, N.; Addadi, L.; Weiner, S., *J. Exp. Zool.* **2002,** 293, (5), 478-491.

25. Raz, S.; Hamilton, P. C.; Wilt, F. H.; Weiner, S.; Addadi, L., *Adv. Funct. Mater.* **2003,** 13, (6), 480-486.

26. Lowenstam, H. A.; Weiner, S., *On Biomineralization*. Oxford University Press: New York, 1989.

27. Sugawara, A.; Nishimura, T.; Yamamoto, Y.; Inoue, H.; Nagasawa, H.; Kato, T., *Angew. Chem.-Int. Edit.* **2006,** 45, (18), 2876-2879.

28. Collino, S.; Evans, J. S., *Biomacromolecules* **2008,** 9, (7), 1909-1918.

29. Oldfield, C. J.; Cheng, Y.; Cortese, M. S.; Brown, C. J.; Uversky, V. N.; Dunker, A. K., *Biochem. J.* **2005,** 44, (6), 1989-2000.

30. Xie, H. B.; Vucetic, S.; Iakoucheva, L. M.; Oldfield, C. J.; Dunker, A. K.; Uversky, V. N.; Obradovic, Z., *J. Proteome Res.* **2007,** 6, (5), 1882-1898.

31. Dunker, A. K.; Oldfield, C. J.; Meng, J.; Romero, P.; Yang, J. Y.; Chem, J. W.; Vacic, V.; Obradovic, Z.; Uversky, V. N., *BMC Genomics* **2008,** 9, 1-26.

32. Delak, K.; Collino, S.; Evans, J. S., *Biochem. J.* **2009,** 48, (16), 3669-3677.

33. Delak, K.; Harcup, C.; Lakshminarayanan, R.; Sun, Z.; Fan, Y. W.; Moradian-Oldak, J.; Evans, J. S., *Biochem. J.* **2009,** 48, (10), 2272-2281.

34. Levi, Y.; Albeck, S.; Brack, A.; Weiner, S.; Addadi, L., *Chem. Eur. J.* **1998,** 4, (3), 389-396.

35. Falini, G.; Weiner, S.; Addadi, L., *Calcif. Tissue Int.* **2003,** 72, (5), 548-554.

36. Cardenas, G.; Cabrera, G.; Taboada, E.; Miranda, S. P., *J. Appl. Polym. Sci.* **2004,** 93, (4), 1876-1885.

37. Falini, G.; Fermani, S.; Ripamonti, A., *J. Inorg. Biochem.* **2002,** 91, (3), 475-480.

CHAPTER 6

CONCLUSIONS

This thesis presented a bio-inspired synthetic organic matrix for controlling the growth of calcium carbonate crystals. My *in vitro* model systematically studied three organic matrix components of nacre (β-chitin, nacre-specific peptides, and a silk fibroin hydrogel) and their affect on mineralization. The results demonstrate that crystal form (polymorph and morphology) is controlled at the organic interface, and that there may be interfacial molecular recognition between the β-chitin and protein/peptide with the mineral.

In Chapter 2, studies with n16N (a nacre specific peptide) investigated its affects on calcium carbonate crystallization. Only in combination with a β-chitin substrate is the assay able to selectivity nucleate aragonite (separately, each component nucleates only calcite). The peptide, n16N, has a binding affinity for chitin, which results in the formation of a new organic matrix interface for interaction with crystal nuclei. This organic interface is capable of selectively growing aragonite, though this interface is not capable of controlling crystal orientation or morphology.

Chapter 3 introduced a silk fibroin-like hydrogel, a major component of the nacre organic matrix, to the *in vitro* nacre model. This chapter discussed the preparation of silk fibroin hydrogels from *Bombyx mori* silkworm cocoons for use in various applications. These results demonstrate that purification method and gelation conditions affect the resulting hydrogel such as gel quality, protein conformation, as well as gel viscoelasticity.

Chapter 4 utilizes the silk fibroin hydrogels for crystallization and interfacial studies on surfaces. With the addition of silk, crystallization results vary from solution controls on various self-assembled monolayers (SAMs) such that crystal orientation

and nucleation have changed. Further characterization of the protein-SAM interface found that protein adsorbed to the various surfaces, affecting the SAM-mineral interface. Upon adsorption, the silk fibroin changes to a more disordered secondary structure.

Chapter 5 further increases the complexity of the *in vitro* nacre model (established in Chapter 2). With the addition of the silk fibroin hydrogel to the chitin-n16N system, further control over crystallization is achieved. Metastable ACC and vaterite structures, which are oriented with respect to the underlying β-chitin fibers, grow in the presence of n16N and silk fibroin hydrogels.

Based upon these studies, general principles regarding nacre formation *in vivo* are elucidated. This thesis has demonstrated that minimalistic *in vitro* models are not accurate to biology, and therefore multi-component systems are necessary to understand *in vivo* biomineralization processes. As discussed in section 1.5, further research is needed to answer other key biological questions such as: what combinations make "good" organic matrices? Chapter 2 demonstrated that n16N binds to β-chitin, and together are able to selectively nucleate aragonite. However, it is still unknown if this interface structures the peptide, and which amino acids are presented to effectively determine polymorph selectivity. Chapter 5 demonstrated that with the complete matrix assembly (β-chitin + peptide + silk hydrogel), crystal morphology and orientation could be controlled, but not polymorph. Is β-chitin + peptide + silk hydrogel a "good" combination (since aragonite selectivity is lost)? To regain aragonite formation, other combinations (such as other nacre-specific peptides, either substituted or added into the system) could also be tested to see if the new combination would give a similar or improved result, and thus increase the matrix complexity further.

Biominerals have controlled structures, composition, shape, and organization. Studying their formation offers insight into control at inorganic-organic interfaces. Applying biomineralization concepts to other materials can inspire new synthetic techniques for creating materials with novel materials properties. To fully utilize Nature's control over mineral formation *in vitro*, continued efforts in fundamental biomineralization research is needed. This thesis has provided a starting platform for future biomimetic crystal growth approaches for understanding and controlling polymorph selectivity, morphology, and orientation.

APPENDIX 1

PROTEIN EXTRACTION FROM MOLLUSK SHELLS

A.1.1. Mollusk shell preparation

American bluepoint oysters (*Crassostrea virginica*), Littleneck clams (*Protothaca staminea*), and zebra mussels (*Dreissena polymorpha*) were used for protein extraction experiments. Oysters and clams were obtained from the raw oyster bar at Maxie's Supper Club (Ithaca, NY) and zebra mussels were scraped from rocks obtained from Onondaga Lake (Syracuse, NY). Zebra mussels were frozen to euthanize the mussels, then shells were split apart, and the internal tissue removed.

All split shells were washed with soap and water and any visible remaining organic material removed. Cleaned shells are soaked in 10% NH_4OH at room temperature overnight to remove any remaining surface organics (i.e., algae etc.) then rinsed with copious amounts of DI water. Shells were rinsed and stored frozen (-20º C) until use. Shell pieces were defrosted and fractured (and in some cases ground into a powder) before immediate characterization or protein extraction.

A.1.2. Shell characterization

Shells were characterized for polymorph, shell microstructure, and organic content. Mineral polymorph was characterized by FTIR with ground shell fragments made into a KBr pellets. Bluepoint oyster shells are composed entirely of calcite and zebra mussels and little neck clams are aragonite (Figure A1.1).

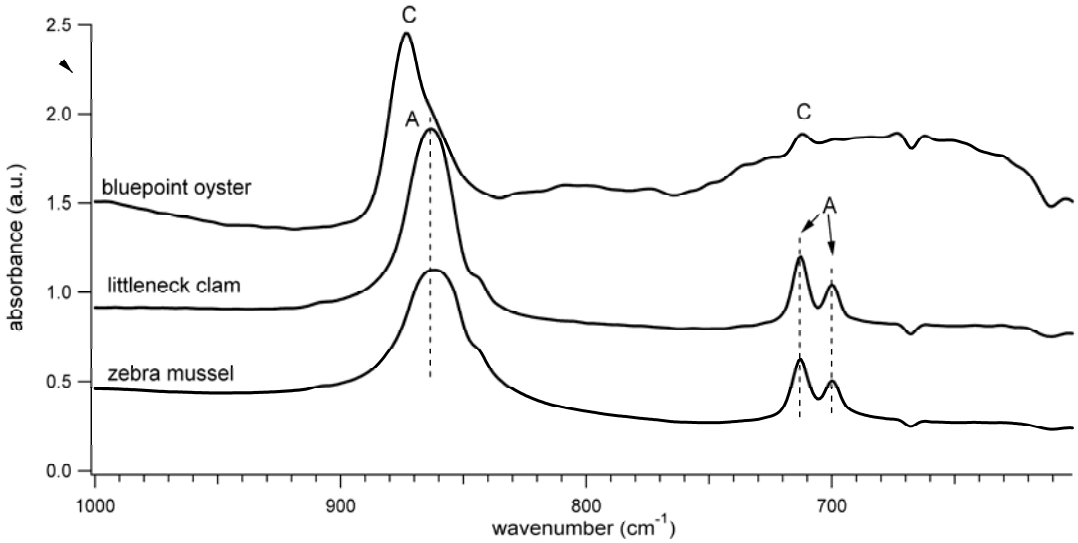

Figure A1.1 FTIR spectra of ground shell from the American bluepoint oyster (*Crassostrea virginica*), Littleneck clam (*Protothaca staminea*), and the zebra mussel (*Dreissena polylmorpha)*. Indices label characteristic calcite (C) and aragonite (A) peaks.

Shell fragments were imaged in the SEM to explore the microstructure of these two mollusk species (Figure A1.2). The oyster has a simple prismatic structure, while the zebra mussel has a more complex crossed lamellar structure, and clams have a monomodal growth pattern (large crystalline regions appear to grow out of one point).

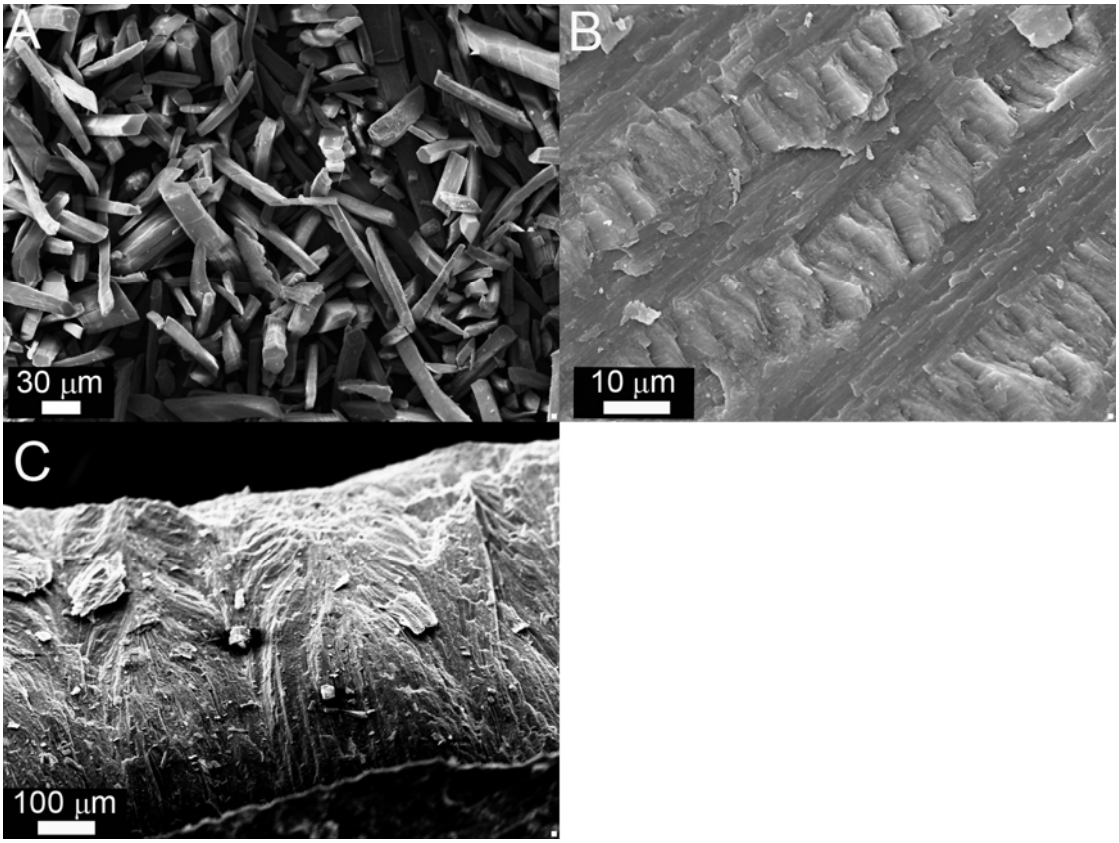

Figure A1.2 SEM micrographs of shell microstructure of (A) Bluepoint oyster prisms (separated by bleach) and shell cross sections from the (B) zebra mussel and (C) Littleneck clam shells.

Ground oyster shell samples were analyzed for organic content via thermogravimetric analysis (TGA, TA Instrumentas Q500, 5º C/min to 550º C from room temperature under a flowing air atmosphere). Even after the temperature ramp is complete, the sample did not plateau indicating that there may be more organic that has not been removed (Figure A1.3, >1.5% intercrystalline organic material).

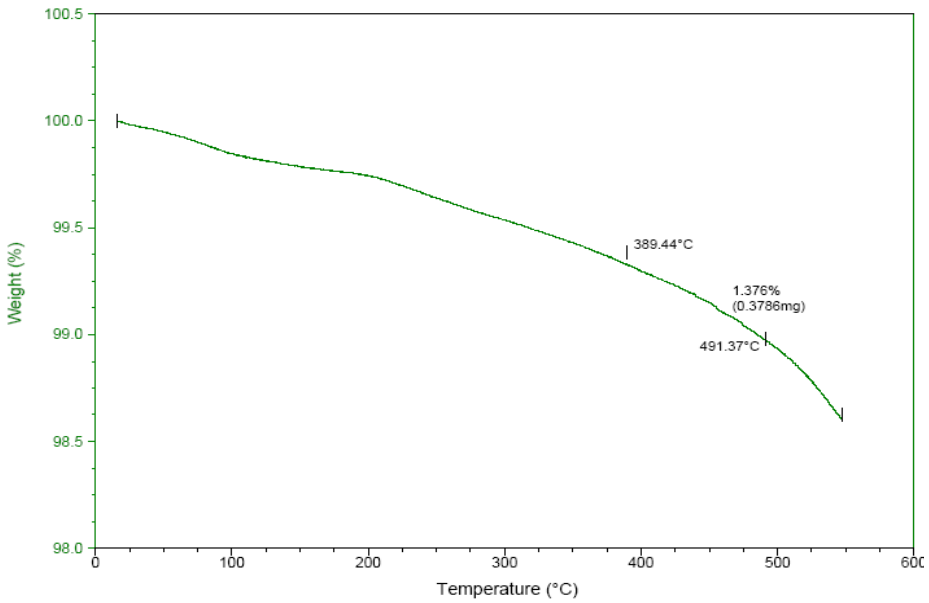

Figure A1.3 TGA curve of powdered oyster shell

A.1.3. Protein characterization

Proteins were extracted using three different approaches from powdered shell material. The first method, suspends the powder in DI water with continuous stirring for 24 hours to solubilize the water soluble organic material.[1] The solution was then filtered to separate out insoluble shell material (yields ~100 mg per 100 g starting shell material). This protein is denoted the water soluble matrix protein extraction. The second method dissolved the powdered shell in 10% EDTA (pH 8) for 24 hours at room temperature with continuous stirring followed by extensive dialysis (Spectrum Spectra/Por 3500 MWCO Cellulose tubing) against DI water to remove the EDTA.[2] This protein extraction is denoted EDTA soluble protein. The last method utilized cation exchange resin.[3] Approximately 40 g of powdered shell was suspended in a dialysis tube (Spectrum Spectra/Por 3500 MWCO cellulose tubing). The dialysis tube was placed in a 1 L plastic bottle filled one quarter full with prewashed and

regenerated cation exchange resin (Dowex) and topped off with DI water. The bottle was continuously rotated at room temperature to keep the resin and powdered shell suspended. The outer DI water was changed once daily until complete mineral dissolution (approximately 1-2 weeks). This extraction method isolates both soluble and insoluble shell proteins and is denoted the "gentle" method (yields ~100 mg per 40 g starting shell material).

The resulting protein solutions (from all extraction methods) were lyophilized to concentrate the organic material. Lyophilized powders were stored dry in the freezer (-20° C) until use. Prior to lyophilization, the soluble and insoluble shell proteins and polysaccharides could be further separated via centrifugation (3000 g, 45 minutes at 4° C). The supernatant is the soluble protein.

CD spectroscopy was used to analyze the protein secondary structure of the water soluble proteins. Both clam and oyster proteins have a random coil conformation (Figure A1.4). It is unknown whether the proteins are in a random coil conformation *in vivo*, or if the proteins denatured during the extraction process.

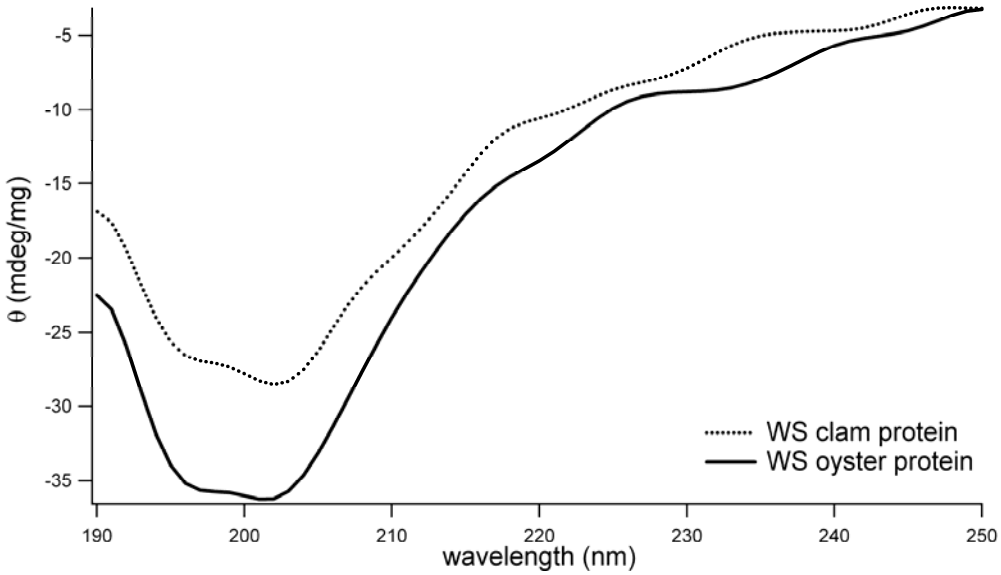

Figure A1.4 CD spectra of extracted shell proteins. WS = water soluble proteins.

Samples of the water soluble matrix proteins were sent to Bio-Synthesis, Inc. (Lewisville, TX) for amino acid (AA) analysis. Analysis included separation, detection, and quantification (via hydrolysis and chromatographic instrumentation, Figure A1.5 and Tables A1.1 and A1.2).

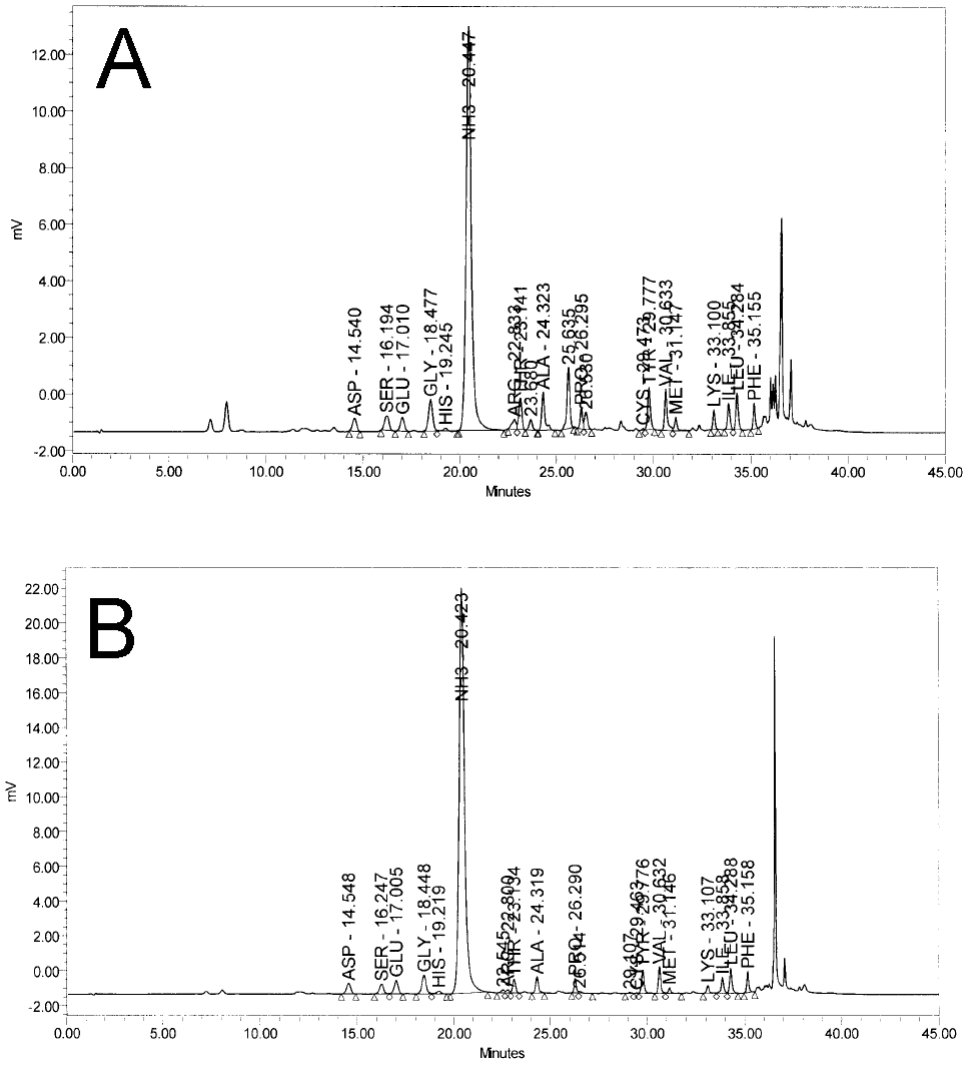

Figure A1.5 Liquid chromatography of extracted (A) oyster and (B) zebra mussel water soluble shell protein. Peptides labels correspond to column run times and assigned amino acids.

Table A1.1 Amino Acid Analysis Data for Water Soluble Oyster Shell Protein

AA	AA in sequence	AA found in pmoles	% recovered
D/N	1	28.833	14.15
S	1	17.977	6.73
E/Q	1	30.828	16.99
G	1	37.830	9.28
H	1	3.611	2.13
R	1	3.284	2.21
T	1	11.790	5.13
A	1	16.047	4.91
P	1	20.825	8.70
C	1	1.141	0.51
Y	1	15.502	10.88
V	1	10.081	4.30
M	1	2.643	1.49
K	1	7.412	4.09
I	1	5.294	2.58
L	1	7.494	3.65
F	1	3.596	2.28
W	0	0.000	0.00

Table A1.2 Amino Acid Analysis Data for Water Soluble Zebra Mussel Shell Protein

AA	AA in sequence	AA found in pmoles	% recovered
D/N	1	20.255	9.98
S	1	18.864	7.09
E/Q	1	19.636	10.86
G	1	37.520	9.24
H	1	2.332	1.38
R	1	7.849	5.29
T	1	16.949	7.40
A	1	26.044	7.99
P	1	19.300	8.09
C	1	2.493	1.11
Y	1	17.543	12.36
V	1	10.927	4.68
M	1	3.882	2.20
K	1	9.345	5.17
I	1	4.885	2.39
L	1	6.370	3.11
F	1	2.601	1.65
W	0	0.000	0.00

Crystals were grown with extracted proteins (water soluble and “gentle”) on glass coverslips to see the affect on crystal morphology and polymorph. All crystals are calcite with very little morphological affects.

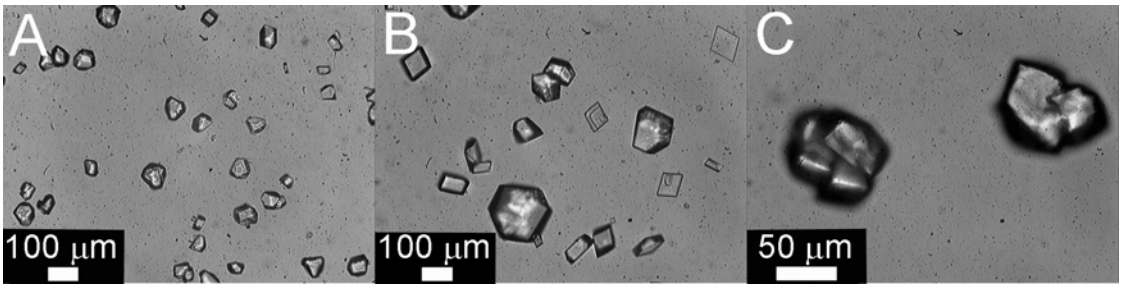

Figure A1.6 Optical microscopy images of calcium carbonate crystals on glass coverslips with (A) oyster water soluble shell protein, (B) clam water soluble shell protein, and (C) oyster protein from the “gentle” protein extraction method. All protein concentrations are 0.5 mg/mL.

REFERENCES

1. Almeida, M. J.; Milet, C.; Peduzzi, J.; Pereira, L.; Haigle, J.; Barthelemy, M.; Lopez, E., *J. Exp. Zool.* **2000,** 288, (4), 327-334.

2. Pereira-Mouries, L.; Almeida, M. J.; Ribeiro, C.; Peduzzi, J.; Barthelemy, M.; Milet, C.; Lopez, E., *Eur. J. Biochem.* **2002,** 269, (20), 4994-5003.

3. Gotliv, B. A.; Addadi, L.; Weiner, S., *ChemBioChem* **2003,** 4, (6), 522-529.

APPENDIX 2

SEM MICROGRAPHS OF VARIOUS BIOMINERALIZAION SPECIMENS

Calcium Carbonate

Rigid pen shell (Atrina rigida)

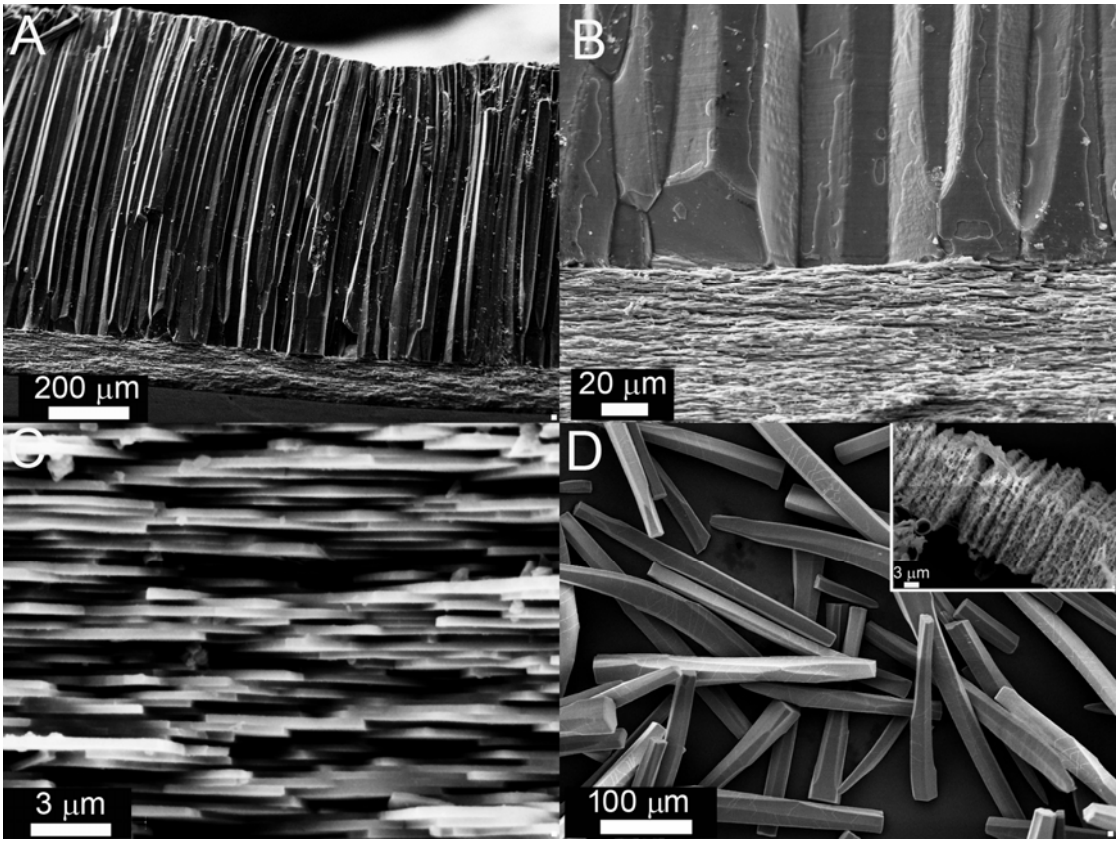

Figure A2.1 SEM micrographs of rigid pen shell (*Atrina rigida*). (A & B) Cross section of entire shell, top = prismatic = calcite, bottom = nacre = aragonite. (C) Magnified region of aragonite nacre tablets. (D) Separated calcite prisms (prismatic layer soaked in bleach to removed intracrystalline organic material). Figure inset of an etched prism (5 minutes,1% acetic acid) to expose intercrystalline organic material.

Zebra mussel (Dreissena polymorpha)

See Figure A1.2B

Littleneck clam (Protothaca staminea)

See Figure A1.2 C

American bluepoint oyster (Crassostrea virginica)

See Figure A1.2A

Calcium Phosphate

Juvenile Feline (Felis catus) Tooth

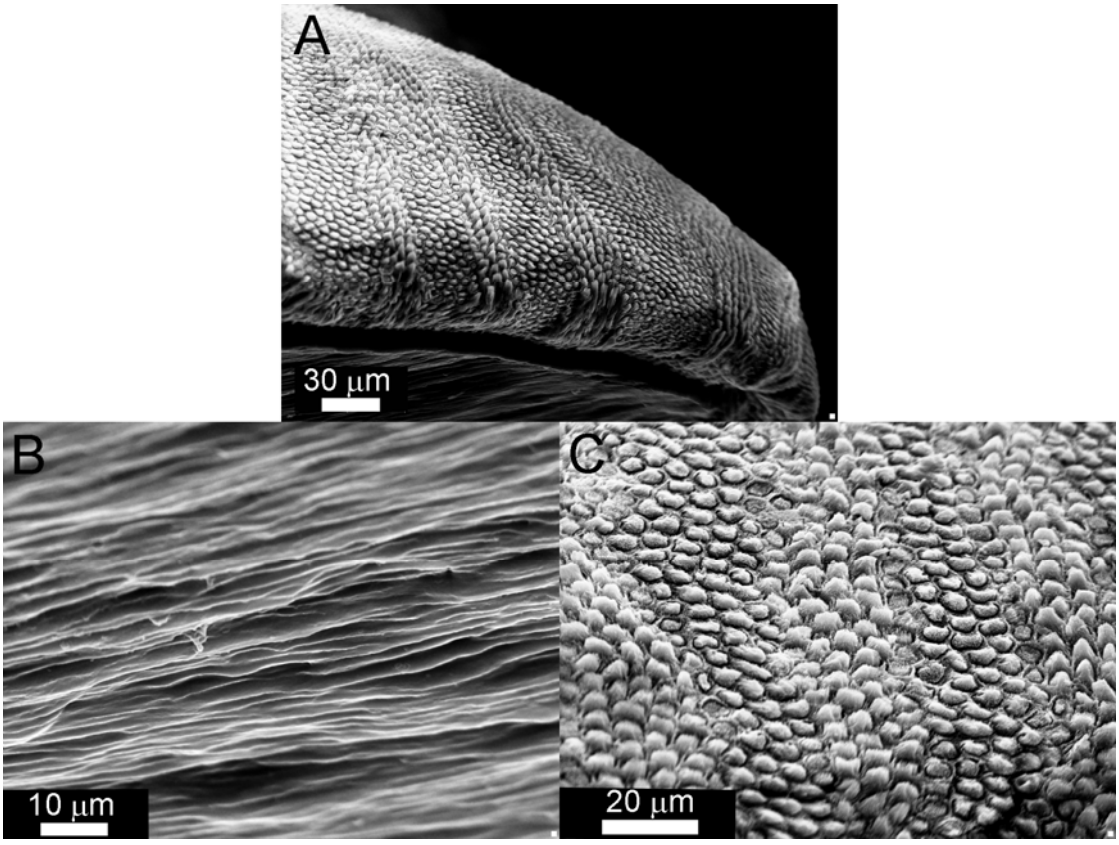

Figure A2.2 SEM micrographs of a fractured and etched (30 seconds, 0.1% nitric acid) juvenile feline (*Felis catus)* tooth. (A) Cross section of tooth fragment, magnified regions of the (B) inner dentin layer, and (C) outer enamel layer.

White-Tailed Deer (Odocoileus virginianus) Antler

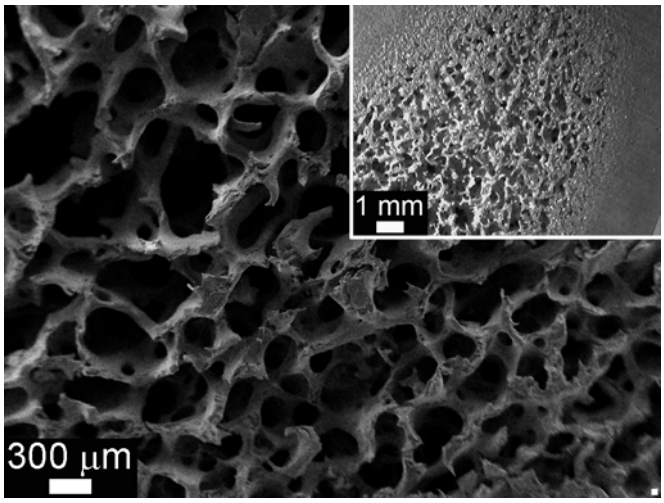

Figure A2.3 SEM micrograph of a cross section of the interior of a deer antler (spongy trabecular bone). Inset: optical micrograph of antler cross section with both the outer cortical bone and the inner trabecular bone visible.

Silica

Freshwater Diatoms

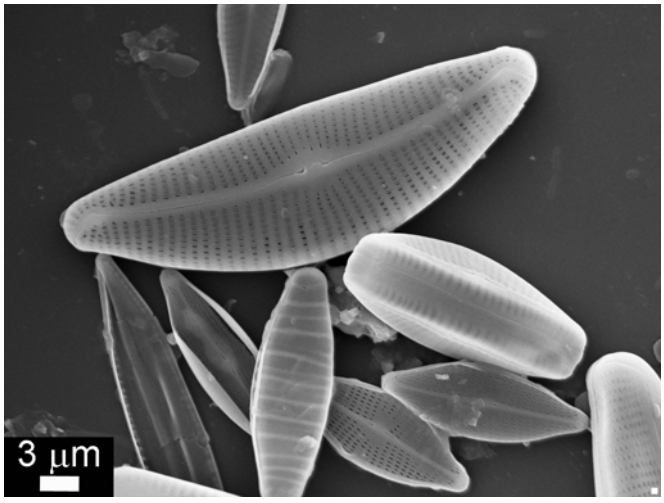

Figure A2.4 SEM micrograph of a freshwater diatom. Diatoms obtained from Beebe Lake/Fall Creek located adjacent to the Cornell Plantations Wildflower Garden.

APPENDIX 3

MISCELLANEOUS SILK FIBROIN RESULTS

A3.1 Etched crystals

To investigate possible silk fiber incorporation into calcium carbonate crystals, etching experiments in DI water were carried out.

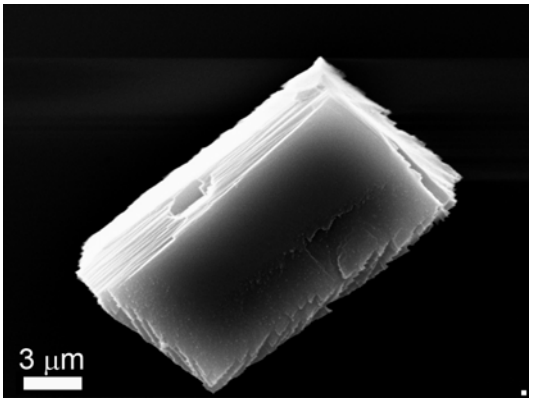

Figure A3.1 Solution (control) grown crystal on glass. Crystals were etched in DI water for 23 hours with minimal crystal dissolution.

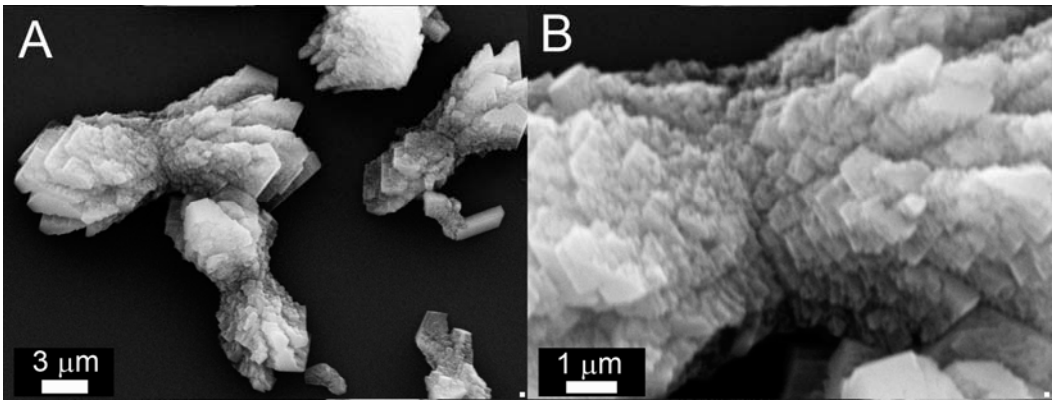

Figure A3.2 Crystals grown on a glass coverslip with aqueous, random coil silk (5 wt%). Crystals were etched in DI water for 13 hours with minimal crystal dissolution.

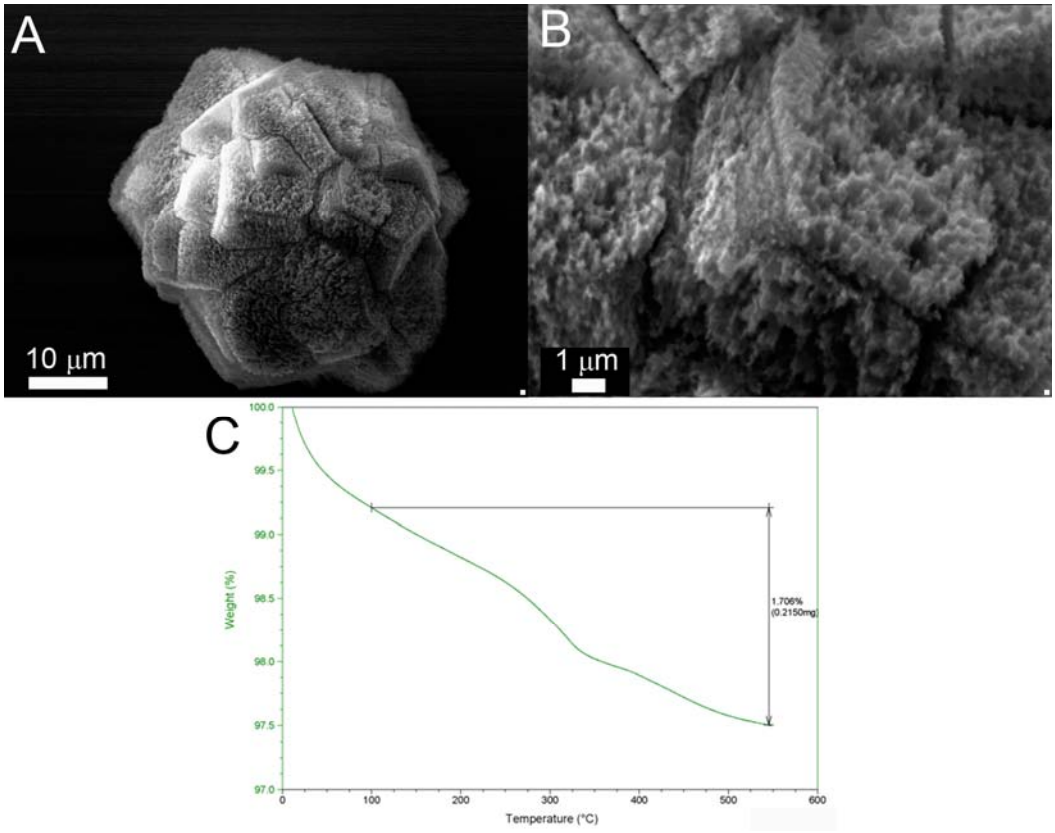

Figure A3.3 Crystals grown in the presence of silk fibroin β-sheet hydrogel (5 wt%). (A, B) Crystals were etched in DI water for 4 hours. (C) TGA of gel grown crystals show minimal (<2%) gel incorporation within the crystal.

A3.2 Crystal growth on silk films

Drops of aqueous silk fibroin was deposited on glass or β-chitin substrates and air dried. Dried silk films were treated with methanol for 2 hours to induce β-sheet formation and film insolubility.

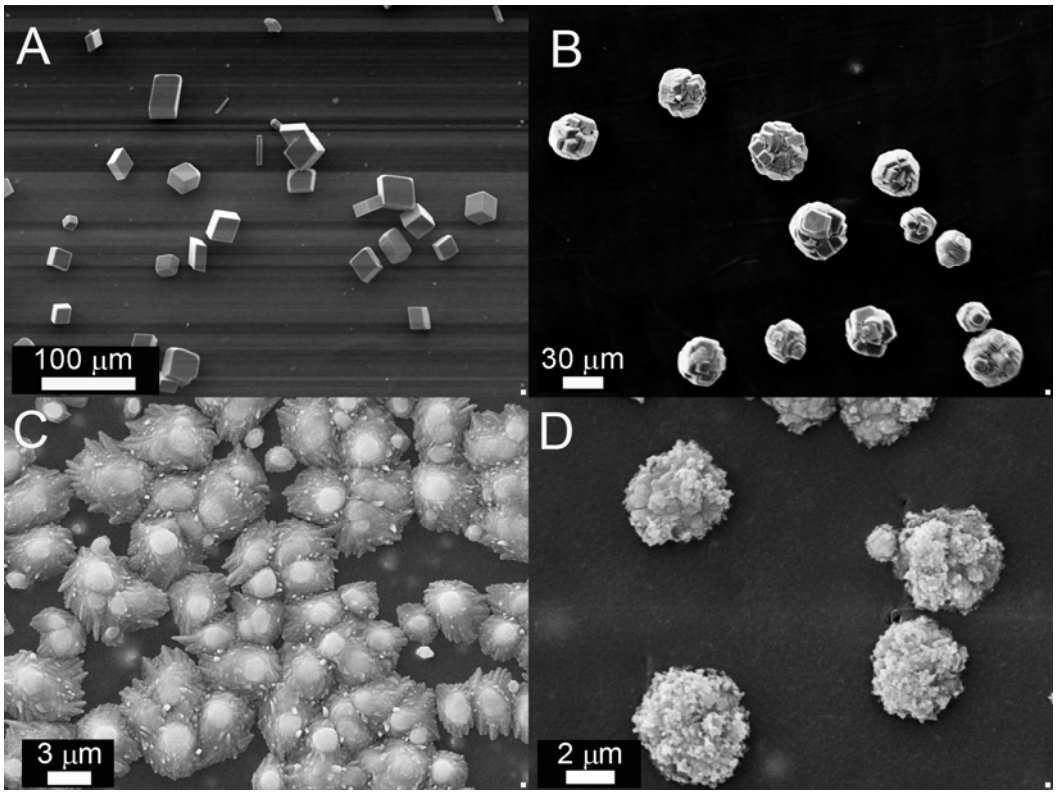

Figure A3.4 Crystals grown on silk films on glass with various additives. (A) Solution grown (no additives) (B) 2.5 wt % silk hydrogel (C) 10 μM p-Glu (D) 10 μM p-Glu + 2.5 wt% silk gel.

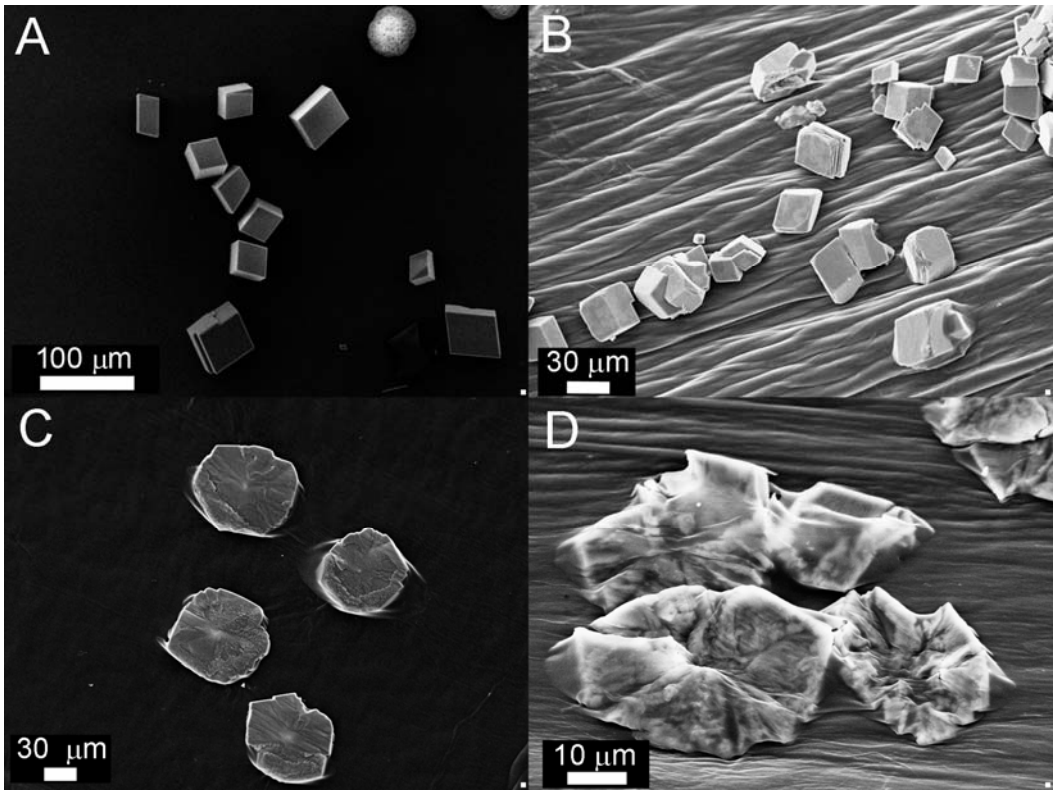

Figure A3.5 Crystal grown on silk films on β-chitin with various additives. (A) Solution grown (no additives) (B) 10 μM n16N (C) 2.5 wt% silk hydrogel (D) 2.5 wt% silk hydrogel grown crystals etched in DI water for 24 hours.